INVESTIGATION OF ELECTRONIC PROPERTIES OF IONIC LIQUID ELECTROCHEMICAL DEVICES BY X-RAY PHOTOELECTRON SPECTROSCOPY

A DISSERTATION SUBMITED TO
THE GRADUATE SCHOOL OF ENGINEERING AND SCIENCE
OF BILKENT UNIVERSITY
IN PARTIAL FULFILLMENT OF THE REQUIREMENTS FOR
THE DEGREE OF
DOCTOR OF PHILOSOPHY
IN
CHEMISTRY

By
Merve Camcı
December 2016

INVESTIGATION OF ELECTRONIC PROPERTIES OF IONIC LIQUID ELECTROCHEMICAL DEVICES BY X-RAY PHOTOELECTRON SPECTROSCOPY

December, 2016

We certify that we have read this thesis and that in our opinion it is fully adequate, in scope and in quality, as a dissertation of the degree of Doctor of Philosophy.

_____

Şefik Süzer (Advisor)

_____

Ömer Dağ

_____

Coşkun Kocabaş

_____

İrem Erel Göktepe

_____

Mehmet Fatih Danışman

Approved for the Graduate School of Engineering and Science:

_____

Ezhan Karasan

Director of the Graduate School

ABSTRACT

INVESTIGATION OF ELECTRONIC PROPERTIES OF IONIC LIQUID ELECTROCHEMICAL DEVICES BY X-RAY PHOTOELECTRON SPECTROSCOPY

Merve Camcı

Ph.D. in Chemistry

Advisor: Şefik Süzer

December 2016

Attention towards electrochemical energy storage devices assembled with innovative solvent-free electrolytes 'ionic liquids' (ILs) has been progressively rising over the last two decades. In order to design a particular electrochemical device it becomes crucial to understand the structure of interfacial region and the electrical response of ILs. Accordingly, this thesis focuses on X-ray Photoelectron Spectroscopic (XPS) investigations of electrochemical devices containing ILs, that is compatible with ultra high vacuum condition needed for XPS. Towards better understanding the fundamental aspects of certain electrochemical issues, electrochemical devices consisting of two metal-electrodes, which contains *N*,*N* – Diethyl -*N*- methyl -*N*- (2-methoxyethyl) ammonium bis (trifluoromethanesulfonyl) imide, (DEME-TFSI) IL-electrolyte between them, have been investigated by XPS under external electrical stimuli control, as a novel analytical tool for elucidating; (i) charging/ discharging phenomena, (ii) electrical double layer (EDL) formation and (iii) electrochemical reaction products.

In the first part, a co-planar electrochemical device, with two gold electrodes on porous polyethylene membrane (PEM) plus DEME-TFSI impregnated between the electrodes, has been studied using external DC bias, for recording the position dependent electrical potential variations. In addition, AC bias is used to harvest temporal behavior. For the AC bias a square wave excitation is used, for which two frequencies are adopted corresponding to slow (10 mHz) and fast (1 kHz) time scales, for probing the response of the system at infinite- and zero-time onset, respectively. In all cases XP spectra have been recorded at different lateral positions. As a result of these DC and AC applications a new understanding has surfaced. Accordingly, although at the metal-electrolyte interface the EDL formation is limited to lateral dimensions at the nanometer scale, its visualization through the analysis of the XPS-probed voltage transients can be extended to very large distances from the interface, in the millimeters scale. These responses have also been modeled using a simple equivalent circuit with two oppositely polarized electrodes and an ionic conducting medium in between.

In the second part, re-arrangement of the DEME-TFSI's ionic constituents at the Au electrode/IL-electrolyte interface has been monitored by the dynamic-XPS approach under application of electrical pulses in the form of a slow (1 mHz) triangular wave with an amplitude of 5V, while recording the intensity fluctuations of the two N1s peaks corresponding to the anionic and the cationic fragments.

In the last part, the externally bias XPS analysis has been used for *in-situ* and *in-vacuo* monitoring of anodically triggered electrochemical preparation and characterization of Au NPs in both a co-planar and also in a wire-plane

electrode electrochemical geometries. The small sized Au NPs' formation within the DEME-TFSI medium has been confirmed by the characteristic peak around 470 nm in the Visible spectrum and with the spherical and well-dispersed (~4 nm) particles in TEM images.

Keywords: X-ray Photoelectron Spectroscopy, ionic liquids, electrical double layer, gold nanoparticles, electrochemical reduction, in-situ monitoring of electrochemical reactions

ÖZET

İYONİK SIVILI ELEKTROKİMYASAL AYGITLARIN ELEKTRONİK ÖZELLİKLERİNİN X-IŞINI FOTOELEKTRON SPEKTROSKOPİSİYLE İNCELENMESİ

Merve Camcı

Kimya, Doktora Tezi

Danışman: Şefik Süzer

Aralık 2016

Yeni bir çığır açan solventsiz elektrolitler ‘iyonik sıvılar’ (ILs) ile bir araya getirilmiş/hazırlanmış elektrokimyasal enerji depolama aygıtlarına yönelik olan dikkat son yirmi yılda giderek artmaktadır. Belli bir elektrokimyasal cihaz tasarlamak için, IL'lerin ara yüzlerinin yapısını ve elektriksel tepkisini anlamak çok önemlidir. Buna göre, bu tez X-ışını Fotoelektron Spektroskopisi (XPS) için gerekli olan ultra yüksek vakum koşullarıyla uyumlu bir IL içeren elektrokimyasal cihazların, XPS ile incelenmelerine odaklanmaktadır.

Belirli elektrokimyasal konuların temel özelliklerini daha iyi anlamak için, iki metal elektrotun arasında N, N-Dietil -N-metil -N- (2-metoksietil) amonyum bis (triflorometansülfonil) imid (DEME-TFSI) iyonik sıvı-elektroliti içeren elektrokimyasal aygıtlar, (i) şarj / deşarj fenomenleri, (ii) elektrikli çift katman (EDL) oluşumu ve (iii) elektrokimyasal reaksiyon ürünlerinin analizlerini aydınlatmak için, yaratıcı bir analitik aracı olarak XPS’in harici elektriksel uyarı kontrolü altında incelenmiştir.

İlk bölümde, gözenekli polietilen membran (PEM) üzerinde iki altın metal elektrot bulunan sistemin arasında DEME-TFSI emdirilerek elde edilen bir eş-düzlemsel elektrokimyasal cihaz, pozisyon bağımlı elektriksel potansiyel değişimlerini kaydetmek için, harici D.C. gerilimi uygulanarak çalışılmıştır. Buna ek olarak, A.C. gerilimi zamansal davranışı aydınlatmak için kullanılmıştır. A.C. gerilimi için, sistemin sonsuz- ve sıfır-zaman başlangıcında tepkilerini saptamak için sıra ile yavaş (10 mHz) ve hızlı (1 kHz) zaman ölçeğine karşılık gelen iki frekansın kullanıldığı bir kare dalga uyarımı ile gerçekleştirilir. Her koşulda, XP spektrumları farklı yerel konumlarda kaydedilmiştir. Bu D.C. ve A.C. uygulamalarının bir sonucu olarak yeni bir anlayış ortaya çıkmıştır. Buna göre, metal-elektrolit ara yüzündeki EDL oluşumu yerel boyutlarda nanometre ölçeğinde sınırlı olmasına rağmen, bunun XPS ile algılanan gerilim geçişlerinin analizi yoluyla görselleştirmesi ara yüzeyden milimetre ölçeğindeki çok geniş mesafelere kadar etkili olduğu saptanmıştır. Bu tepkiler aynı zamanda, iki zıt polarize olmuş elektrot ve bunların arasında bir iyonik iletken madde bulunan basit bir eşdeğer devre kullanılarak modellenmiştir.

İkinci bölümde, DEME-TFSI'nin iyonik bileşenlerinin Au elektrot / IL-elektrolit ara yüzünde yeniden düzenlenmesi, dinamik-XPS yaklaşımı ile yavaş (1 mHz) üçgen dalga şeklinde 5V'luk bir genlik elektriksel darbeler uygulaması altında, anyonik ve katyonik fragmanları temsil eden iki N1s tepesinin şiddetlerindeki değişimler kaydederek izlenmiştir.

Son bölümde, harici potansiyel uygulanan XPS analizleri, Au-NP'lerin hem bir eş-düzlemli hem de bir tel ve düzlem-elektrot elektrokimyasal geometrilerinde anodik tetiklemeli elektrokimyasal hazırlanışının gerçek zamanlı ve vakum ortamında izlenimi ve karakterizasyonun için kullanılmıştır. DEME-

TFSI ortamı içindeki küçük boyutlu Au NP'lerin oluşumu Görünür bölgedeki optik spektrumda 470 nm civarındaki karakteristik bir tepe ve TEM görüntülerdeki küresel ve iyi dağılmış (~ 4 nm) parçacıklarla teyit edilmiştir.

Anahtar Kelimeler: X-ışını Fotoelektron Spektroskopisi, iyonik sıvı, elektrikli çift katman, altın nanopartiküller, elektrokimyasal redükleme, electrokimyasal reaksiyonların gerçek zamanlı görüntülenmesi

Acknowledgement

As one-step to the end of my education in Bilkent University, but as the first step in science, I want to express my deepest gratitude and respect to my advisor Prof. Şefik Süzer; he has been always the 'leading lights' for me since 2009 through his scientific perception, guidance and tremendous mentoring . I learnt and have been still learning a lot from his enthusiasm and dynamism.

I would like to express my appreciations to Dr. Burak Ülgüt and Dr. Coşkun Kocabaş for their valuable support, provision, collaboration and fruitful discussions during my experiments.

The first person, who I met at the beginning of my chemistry story in Bilkent, was our graceful department secretary Emine Yiğit and many thanks for her support, alliance and assistances in administrative issues.

Special thanks to our present and former group members Pınar Aydoğan Göktürk, who is not only my lab mate but also coffee-mate, holiday-mate, shopping-mate and yoga-mate; and Ahmet Uçar; We laughed a lot, talked a lot, worked a lot, planned and did many unforgettable "a lot" things together and thank you a lot. One more special thanks to my dear friend Seylan Ayan, for her encouragements to continue but not give up and morning coffee chats in the garden.

I am always to be proud of Taners' daughter and I could not succeed without my dad's morning reinforcements, my mom's patience, perception and their endless love. Thank you my *Pinokyo* for being my blind side…

I was 18 years-old when I came from Konya to Bilkent, as I am leaving at the beginning of my 30s with great memories. Whatever or whenever I lived was ephemeral, at the end I was in Bilkent and now I would like to thank you Bilkent, see you soon!

More than a thank you or more than a dedication, I am so glad to have an adorable husband who sweeps every single obstacle from my life-path and comes with a cup of tea or glass of wine while I am studying. We are now turning over a new leaf to Strasbourg and he is again with me…

This PhD work and my daughter were born in August 2012. When I have taken her to the lab, she has asked me for "two or three atoms to do some experiments." After four years, I am graduating with my daughter from same university so I dedicate this thesis to *Asya Masal*…

Contents

List of Figures

List of Tables

List of Schemes

List of Abbrevations

A.C. : Alternating Current

AFM: Atomic Force Microscopy

AR-XPS: Angle Resolved- Xray Photoelectron Spectroscopy

D.C. : Direct Current

DEME-TFSI:N,N-Diethyl-N-methyl-N-(2-methoxyethyl)ammonium-bis(trifluoromethanesulfonyl) imide

EDL: Electrical Double Layer

EW: Electrochemical Potential Window

IL: Ionic Liquid

NMR: Nuclear Magnetic Resonance

NP: Nanoparticle

PE: Polyethylene

PEM: Polyethylene Membrane

RTIL: Room Temperature Ionic Liquids

SEM: Scanning Electron Microscopy

SFG: Sum Frequency Generation

STM: Scanning Tunneling Microscopy

SPR: Surface Plasmon Resonance

SQW: Square Waves

TEM: Transmission Electron Microscopy

TRW: Triangular Waves

UHV: Ultra High Vacuum

UV-vis: UV- visible

XP: X-ray Photoelectron

XPS: X-ray Photoelectron Spectroscopy

Chapter 1

Introduction

1.1. Ionic Liquids and Their Properties

1.1.1. Ionic Liquids

The “ionic liquid” term has been used for the salts in liquid state with melting points below 100 ˚C, which are also referred as Room Temperature Ionic Liquids (RTILs). An ionic liquid can be described as an inorganic salt, when it *melts* or liquefies without any molecular solvent (molten salt). In contrast to similar ionic character of the simple salts, the molten-salts are corrosive and are at high temperatures, whereas real ionic liquids have different properties. In Figure 1, an ionic liquid N,N-Diethyl-N-methyl-N-(2-methoxyethyl)ammonium bis (trifluoromethanesulfonyl) imide (DEME-TFSI) and a common inorganic KBr salt consisting of K^+ and Br^- ions are represented at room temperature with their molecular structures. DEME-TFSI is an ionic liquid at room temperature but has no detectable melting point, but only a very low glass transition temperature at -

91°C. In contrast, the melting point of KBr is 734 °C, so KBr is solid at room temperature and highly corrosive in its molten state.

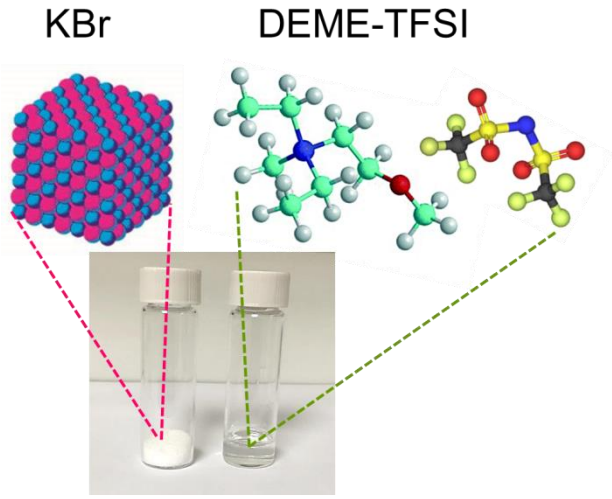

Figure 1. Representative images of potassium bromide salt (KBr) and N,N-Diethyl-N-methyl-N-(2-methoxyethyl)ammonium bis (trifluoromethanesulfonyl) imide (DEME-TFSI) ionic liquid at room temperature with molecular structure.

Through the history of the ionic liquids, various terms such as "molten salts," "room temperature molten salts," "ionic fluids" "ionic melts," and "liquid organic salt" have been used for their description. Ionic liquids were introduced to the literature with an article published in 1914, which described the ethyl ammonium nitrate salt liquid at room temperature with melting point of 13-14 ˚C.[1] In 1951, Hurley and Wier [2] introduced details of the chloroaluminate – based liquid salts, as melts, under ambient conditions after three years from their patent in literature.[3] The term "fused salts" entailing only of ions but in the liquid state was described in 1965 by Sundermeyer and co-workers.[4] Afterwards in 1975, use of "molten-salt system" for practical electrochemical applications was reported for the first time. The room temperature ionic liquids (ILs) were primarily introduced as "fused and liquid salts" with enhanced physio- and

electro-chemical properties, in late 1900s by Wilkes showing that IL can be prepared from various combinations of cations and anions.[5] By definition, ILs are non-aqueous liquid salts comprised merely of anions and cations at room temperature. Beyond the rich history, as a general description of ILs in literature they are the ionic compounds with organic cations and inorganic anions in liquid state at room temperature.[6]

1.1.2. General Properties of Ionic Liquids

Since ILs are composed merely of ions, the properties of ILs are governed not by the individual properties of cation and anion in the structure but appear as complete average properties of both of them. The appropriate selection and so the combination of the anion and cation enables designing and fine-tuning of the ILs' properties for particular purposes. *For instance ILs can be designed in different structural variations by matching of a cation with an anion; hence there exists more than 10^6 possible ILs arrangements.*[7] Figure 2 represents the chemical structures of most common cations and anions that are used in ILs' arrangements. In the ILs' structure the ionic constituents are held together with hydrogen bonds, coulombic and weak van der Waals interactions. This purely ionic composition imparts high intrinsic charge density. ILs have numerous unique physicochemical properties such as low toxicity, non-flammability, high thermal and chemical stability, wide-ranging electrochemical window etc. As a very critical characteristic property, the melting points of ILs are low, so they are liquids below 100 ˚C. Due to the relatively large size, asymmetric and complicated structure of the cation and its combination with a flexible and charge delocalized anion these organic salts deviate severely from their ordered crystal

structures and turn into disordered liquids under ambient conditions.[5, 6, 8-13] The density of ILs are in the range of 1.2 - 1.5 g/ml and their viscosity values are typically around 30-50 cP (η_{H2O} = 0.89 cP).[14] The type of cationic and anionic fragments has a large effect of the ILs' viscosity and these viscosity values are found to be one or two orders of magnitude higher than the conventional molecular solvents.[15-18] The higher viscosity values are interconnected to the low mobility of ions within the ILs' medium, thus the ions are slowed down in highly viscous media as a rudimentary consequence of their hindered diffusions. Accordingly, because ILs are high charge carriers large conductivity values are expected at the outset. However, due to the hindered mobility their conductivities are at a level of 10 mS/cm that is not considerably different from those of the molecular solvents.[12, 16, 18-20]

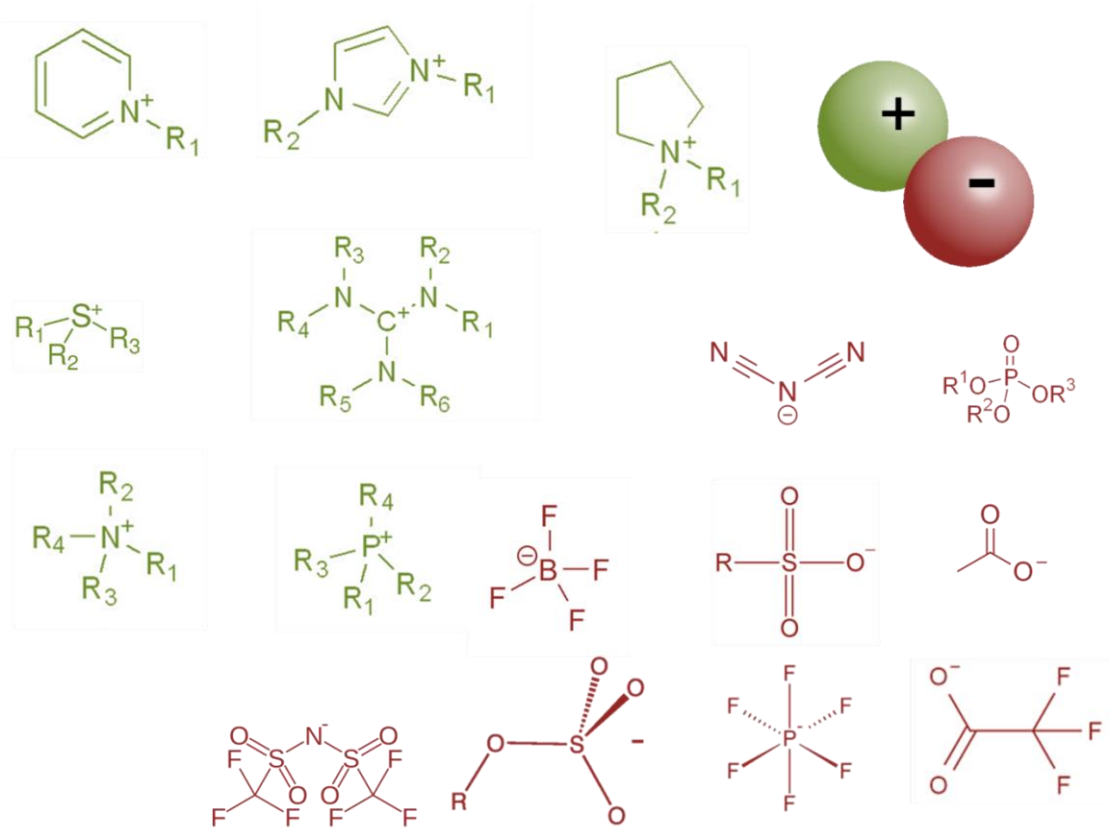

Figure 2. Chemical structures of common cations and anions of ILs.

Although ILs are ‘liquids’ they have exceedingly low vapor pressures at room temperature, that are practically not measurable, so can be accepted as zero. For example vapor pressure of 1-*n*-butyl-3-methylimidazolium salts was reported to be ~10^{-10} Pa[21] at 298 K that is 10^{13} orders of magnitude lower than H_2O (~10^3 Pa at 298 K).[22] Consistent with their physical form but contrary to the volatility characteristics of the liquids, ILs are non-volatile. [7, 23, 24] The non-volatility of ILs is interrelated with the thermal stability, where ILs do not undergo thermal decomposition in wide temperature ranges (up to 600K) for 1-Alkyl-3-methyl imidazolium bis(trifluoromethylsulfonyl)imide.[25]

1.2. Applications of Ionic Liquids

Ionic liquids (ILs) provide a bundle of unusual properties as liquids that are different from those of the molecular solvents, so ILs have attracted a fascinating growing interest in a wide range of scientific and technological applications. Through their primary properties, ILs appear to be alternative to the common molecular liquids and their fine-tunable characteristics open novel application areas (examples are given in Table 1) in designing innovative systems with advanced performance, in addition to the conventional applications covering energy storage,[26-29] energy conversion,[30] catalysis[8, 23, 31-34] or chemical synthesis.[5, 35-40]

Table 1. Common Applications of Ionic Liquids

Electrolyes	Solvents
▪ *Batteries* ▪ *Fuel-cells* ▪ *Supercapacitors* ▪ *Thermal liquids* ▪ *Solar cells* ▪ *Actuators* ▪ *Sensors*	▪ *Nano-structure synthesis* ▪ *Organic reactions* ▪ *Catalytic reactions* ▪ *Polymerizaiton reactions* ▪ *Enzymatic reactions*
Bio-functional materials	**Analytical materials**
▪ *Protein crystallization* ▪ *Drug delivery* ▪ *Artifical tissues* ▪ *Bio-reactors* ▪ *Colony culture* ▪ *Biomass processing*	▪ *Membranes* ▪ *MALDI-TOF matrices* ▪ *Extraction / separation matrices* ▪ *Lubricants* ▪ *Additives*

1.2.1. Ionic Liquids in Electrochemical Systems

Ion conductive and electron conductive materials are two essential materials which have vital significance for electrochemical systems. Electrolytes are aqueous or organic solvent based components and they are essentially used as ion conducting materials in electrochemical systems. However, solvent based conventional electrochemical systems suffer from the volatility and decomposition problems in high operating temperatures and voltages, inflicting poor performance plus short life time to the electrochemical devices. Therefore, ILs appear as innovative solutions, since they are electrolytes, which are merely composed of dense ionic components free of solvent; maintain liquid characteristics and stabilities in wide temperature and voltage intervals.[13, 14]

Replacement of aqueous or organic electrolytes with ILs opens new routes in electrochemical applications. For instance, the electrochemical reactions in aqueous or organic media can also be performed in ILs. In addition, use of ILs

overcomes the impossibility of certain processes that cannot be performed in aqueous media. [41, 42]

The foremost issues for energy storage devices such as solar cells, fuel cells or double layer capacitors, are primarily safety and performance. Electrolytes, being nonvolatile and free of any molecular solvent, enable safer applications in outdoor use in addition to prolonged operational life times and impart higher performance to the electrochemical energy storage devices. As a result, for applications in electrochemistry, thermodynamically and kinetically stable ionic liquids are suitable electroactive candidates on account of their high ionic conductivity plus durability against flammability and volatility instead of aqueous and / or organic electrolyte solutions that are usually volatile and unstable.

Any kind of electrolyte is usable in electrochemical systems, if and only if the electrolyte of interest can conduct the electrochemical processes of the species devoid of any side redox reactions and / or solvent breakdown, before the electrolyte itself. Besides, not only the electrolyte but also the electrode in the electrochemical system must be stable against either oxidation or reduction within the operating potential range. The operating potential range for an electrochemical system corresponds to electrochemical potential window (EW) that is connected to its electrochemical stability. The limit of the EW appears as the boundary for potential at which the electrochemical decomposition of either ions of the electrolyte and electrode materials deviate from their stability and start to decompose. The conventional aqueous electrolytes have narrow EWs, as small as 0.9 V, and use of organic electrolytes increases this value to around 2.5-2.7V.[43, 44] In contrast, ILs have higher EW values in the range of 4.2 to 5.4 V,

typically 4 V but up to 6 V in some cases, compared to the conventional electrode-electrolyte systems.[45-49] This electrochemical stability potential window is directly related with the performance and the energy stored in a given electrode-electrolyte system. For the performance of the electrochemical cell, the electrolyte decomposition at high potentials limits the cell voltage, since the wider the electrolyte stability potential window is the higher the cell voltage and the energy density.[43, 44] Thus ILs enable operation of electrochemical systems in wide potential ranges with improved energy and charge densities.

1.2.1.1. Ionic Liquid Interfaces

In general, average molecular and geometrical properties control thermodynamic and kinetic properties of ILs. So for ILs' applications in many systems covering electrical energy devices such as fuel cells or double layer capacitors and catalytic processes, the molecular orientation of the charged fragments within the IL structure must be well understood. Although the novel bulk properties of room temperature ILs have been researched extensively over the past decades, their structural and interfacial investigations are limited to few studies. The IL interface region corresponds to the region where the anions and cations of the corresponding IL are in contact with the other phase i.e. gas, liquid or solid phases. The composition and the fragmental arrangement of the ILs at interfaces are very different as compared to those in the bulk. Hence, investigations on the preferential arrangements of the anions and cations at the ILs interface become essential for fundamental understanding in further developments and applications. In general, the structural arrangements of the ionic fragments

closer to the IL interfacial region are complicated topics and are still under investigation without deep understanding.

In order to obtain detailed information about the chemical structure of ILs at the surface, the interface between IL and the gas phase molecules has been investigated to understand whether anionic or cationic fragments of ILs dominate the gas interface or both of the ions exist in equal amounts, and whether they are being positioned parallel or perpendicular to the surface plane. For instance, the structure of the IL/gas interface plays a crucial role in catalytic systems' development, since it has impact on understanding of the chemical reactions at the interfacial region plus their mechanisms, such as adsorption of gaseous molecules on the IL-surface and catalytic reactions taking place therein.

Accordingly the IL/gas interfacial region was studied by direct recoil spectrometry where signal was coming from the outermost 2-4 Å depth of the IL surface, which was combined with time-of-flight analysis, to identify the surface atoms and/or molecular composition.[50] In this work, the ionic fragments were studied with glancing incidence of ion beam as a function of analysis depth. The cationic fragment of imidazolium ring containing ILs was found to be positioned at the surface together with the anionic fragment though perpendicular to the surface plane.[50, 51] IL/gas interface of the similar systems containing imidazolium ring in the ILs' structures were also studied by sum frequency generation (SFG) vibrational spectroscopy, which is an extremely surface sensitive technique and probes the interfacial structures within 30 nm through their vibrational spectra. [52, 53] It was found that the spectra were dominated by the alkyl chains, which were the lowest energy component of the cationic fragments. Thus, the authors also stated that the composition of the surface is

dominated by lowest surface energy component of the system. In another work on imidazolium derivative ionic liquids with two different anions, the X-ray reflectivity analysis were performed to clarify the surface layering and the anion enrichment within the bulk IL-structure as a function of the surface-normal electron density with an angstrom-scale resolution.[54] They found that surface layer within thickness of 6-7 Å consisted of the standing up alkyl chains of the IL.

1.2.1.2. Electrode/Ionic Liquid Interface and Electrical Double Layer

The solid/IL interface is a fascinating region and need to be better understood, since when a liquid is brought into contact with an electrified solid surface, the liquid molecules undergo rearrangements adjacent to this well-defined solid surface. The interface between ILs/solid surfaces is established by merely of ions through their interaction with the electrified solid-surface. So the ionic arrangement and the orientation of individual cationic or anionic constituents at charged or uncharged solid interfaces appear to be important point of discussion/investigation.

The relative positions of the negative and positive ions in the structure of IL that is adsorbed on uncharged and charged graphite surface have been modelled to obtain information about the internal orientation at IL/solid interface through computational analysis.[55-57] In these computational works, the cationic fragment was found to be re-oriented to the uncharged electrode surface Moreover, the concentrations of the adsorbed anionic and cationic fragments were found to be controlled by the surface charge of the electrode. As a result of the molecular simulation work, Kislenko and co-workers reported also that the ILs'

structure differs from that of the bulk at uncharged graphite surface and yet has an ordered structure, at the negatively charged surface/IL interface.[55] The molecular structure at the interface turns into a multilayered structure of ions as alternating anionic and cationic fragments.

The interaction between IL and a solid surface is strongly dependent on interfacial properties since the solid surface imparts physical and chemical constraints. If the surface is positively polarized the negatively charged fragments of the IL structure are expected to be closer to the interface or positively charged fragments are repelled by the developed charges at IL/solid interface. At the interface between IL and the negatively or positively charged solid surface, there exists a reorientation of the charged fragments of ionic liquid with respect to the surface charge. Thus the polarity difference between the IL and the solid surface is the cause of Electrical Double Layer (EDL) formation depending on the charged fragments' reorganization at the interfacial region.[58-63]

In the classical Electrical Double Layer (EDL) concept, there exists a strong interaction between the electrode surface and electrolyte, when an electrolyte is brought into contact with an electrode. Because the solvated ions are mobile in the electrolyte together with the neutral molecules, the ions undergo a redistribution with respect to charge on the electrode surface through electrostatic interactions, and as they approach the electrode surface a charge balancing layer is also formed at electrode/electrolyte interface.[64] In 1850s Helmholtz suggested his model for the EDL, which described the formation of compact only one-ion thick layer as a result of the electrostatic interaction. Later, in early 1900s Gouy-Chapman model was proposed to modify the thickness of EDL as not being limited to one-ion layer but also to the formation and the existence of ionic diffuse

layer. Accordingly, Stern combined these two models in 1920s and defined the EDL concept as a combination of a one-type of solvated layer at the electrode/electrolyte interface together with charge reversed diffuse layer comprised of alternating counter-ion layers.[65]

Gouy-Chapman-Stern EDL theory assumes dilute solvents that contain dissolved ions and neutral molecules as electrolytes. Upon the application of the electrical potential, the charge on the electrode is screened by the local association of the anions and the cations plus the neutral solvent molecules at a simple boundary between electrode surface and electrolyte solution, adopting an opposite net charge with induced structural changes. Since ionic liquids are composed merely of charged fragments and these fragments are mobile under ambient conditions, which enable structural rearrangement of them, they render different properties than those of the electrolytes in an electrochemical system. Therefore classical EDL models are not applicable to the electrode/IL interfaces. This is schematically shown in Figure 3 for representation of the EDL model for the classical electrolyte system and the IL system. Basically, the electrode is assumed to be a planar sheet of charges and the ILs consist of only anions and matching cations in equal amounts. In order to screen the charge on polarized electrode, the exact one-to-one ratio between anion and cations is disturbed at the electrode/IL interface. On this concept, experimental and theoretical works meet in the same question: *"How is the interfacial structure and what are the ionic arrangements near the electrode surface?"*

The redistribution of the multiple ion layers at electrode/IL is not modest, because of the high electrostatic interactions between anionic-cationic species, predetermined ion size, their large and complicated shape plus the steric

hindrance of these ions and are all essential inputs to model EDL structure in ILs. [61, 66-73] In addition, ILs systems with high density of ions prevent the formation of solvation layers at electrode/IL interfaces. This results in the movement of anionic or cationic fragments near electrode region in interfacial ordering and the formation of multiple ionic layers in alternating manner in order to compensate the charge on the electrode surface at the interface between electrode/IL.[56, 60, 73-76]

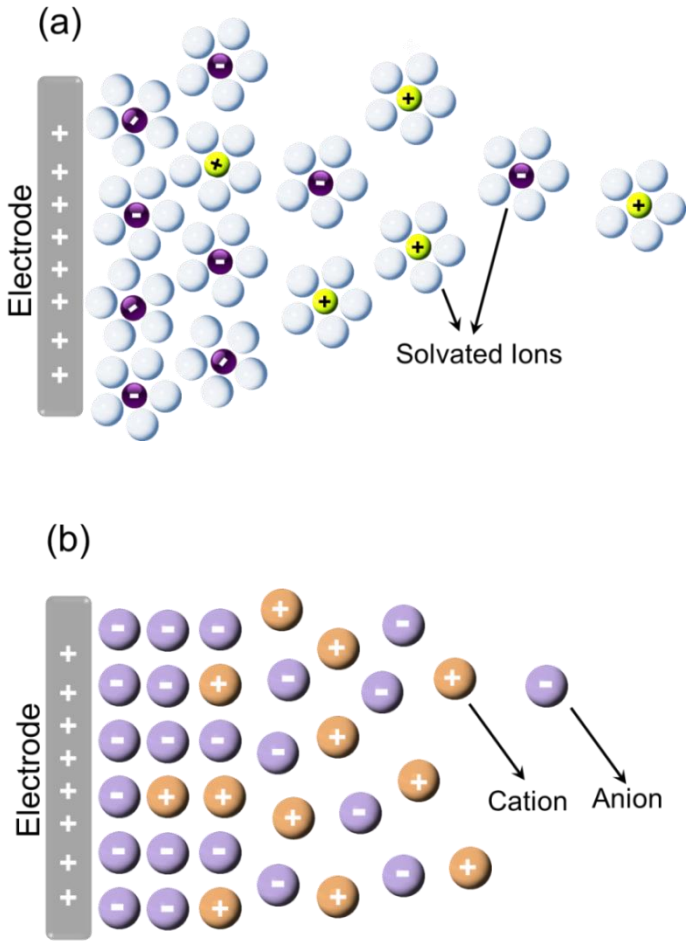

Figure 3. Schematic representation of (a) Classical EDL model and (b) EDL model for ILs.

The work of Baldelli et al., through SFG analysis shows that there exists an oriented layer of cationic and anionic fragments at the Pt electrode/ionic liquid interface where the arrangement of the ionic fragments are controlled with respect to the electrically developed positive or negative surface charge on the Pt-electrode.[66] Hayes et al. studied the interfacial layer that has excessive degree of organization, between IL and Au (111) electrode in order to understand the EDL structure at the electrified electrode/IL interface using AFM as a function of applied potential to the electrode.[61] They concluded that the double layer formation and the relative orientation of the ionic fragments closest to the electrode surface were strongly dependent on the applied electrode potential and electrostatic forces between electrode surface and cations of IL. ILs are found to be inserted into carbon micro-pores of the graphite-electrode without any potential application, but adsorption/desorption of the counter ions from the carbon pores are detected under potential, by Merlet et al. [56] They also showed by molecular simulations of applied constant potential differences to the two graphite electrodes and IL-medium in between then resulted in EDL formation, existence of differential capacitance and charge density fluctuations in the sub-nanometer scale. Moreover they found out that only the half of the applied constant potential was prevailed on the bulk-IL. In their more recent works, molecular details based on the computer simulations showed as a function of voltage, that the number of cations in tilted position is increased at the positive electrode but decreased at the negative one.[57, 77] Also they indicated the number of anions at both electrodes is also increased in order to balance the cations. In turn the anions enter the first ionic layer as a result of compact structural reorganization.

Atomic Force Microscopy (AFM) is used to obtain information about IL/electrode interfaces' structure since the force between AFM probe is surface sensitive to the charges plus dimensions of anions and cations. Similarly, using both AFM and STM techniques, rearrangement of anions and cations was studied at the Au (111) electrode interface with respect to the applied potential.[70] Another AFM and STM study showed that the structure of interfacial region within 5nm between IL/Au-electrode can be tuned and is strongly dependent on the ion structure of the IL, where the ionic arrangements also vary with the sign plus the extent of the applied potential.[78] A recently performed impedance analysis on the ion-electrode interactions examined the differential capacitance developed as a function of the applied potential to the electrode.[79] This differential capacitance is found to be sensitive to the conformational changes, in addition to the interaction between electrode material and the cations and anions.

To sum up, at the ILs/electrode interface, the EDL structure of ILs is defined as combination of a ionic layer that alternates the charges on the electrode surface and the densely packed counter ions alternate the net charges in neighboring layers.[80, 81] Within an electrochemical system consisting of two electrodes and IL-electrolyte, when the potential is applied across the electrodes, anions migrate towards positive electrodes while the cations migrate towards the negative one forming EDL structure with a maximum charge at the electrode surface. The applied potential drops within the range of EDL structure, which is around few nanometers and decays towards equilibrium forming layered-ionic distribution that approaches to the bulk IL structure establishing the overall charge to be neutral.[80, 82, 83]

1.2.2. Ionic Liquids and Metal Nanoparticle Syntheses

The properties of bulk materials are independent of their size, though the properties start to be deviating when the size of materials falls in the nano-scales. The “nano” sized materials, as a transition between atomic and bulk forms, exhibit different properties than either those of the bulk material or atomic forms The “nano” term usually refers to the particle size in the 1-100 nm range and the particles in nano-scale dimensions are often called as “nanoparticles”, “nanocrystals” or “nanocolloids.” Nanoparticles (NPs) have been known since ancient time; for example in ancient eras Au NPs had been used to give red color and glittering effect on the bowls or paintings. The very famous “*Lycurgus Cup*” which belongs to Romans in the 4th century, contains Au NPs inside and shines in red or green with respect to the angle of incoming light. In 1857, Micheal Faraday reported on the optical properties of nano-sized metal particles, and for the first time scientific clarification was given. In his well-known work on the Au NPs with characteristic bright red color were obtained by the chemical reduction of chloroaurate ion in an aqueous solution.[84] The “nano” technology appears to be one of the recent research areas in science with an ever increasing attention over the past two decades leading to numerous innovative approaches for preparation of nano-sized materials, especially the metal NPs, and understanding their new properties. Therefore, the topics in nanotechnology cover a wide range of NPs’ applications including biological systems, catalysis, electrical devices, energy storage systems, environmental issues etc.

Among the research fields on nano-materials, nano-sized particles of gold (Au NPs) exhibit interesting features and gets growing attention. As being one of the most stable NPs, Au NPs have been the topic of interest in electronic,

magnetic, optical, biologic and catalytic applications.[85-89] Within the scope of this doctoral thesis examples of Au NPs are discussed since in the upcoming chapters including thesis's results and discussions, Au NPs will be within the central theme.

1.2.2.1. Metal Nanoparticles

The metal NPs are prepared by various methods; reduction of metal salts through simple chemical reduction, electrochemical reduction, photochemical reduction and sonochemical reduction or photolytic, thermal and sonolytic decomposition of metal organic precursors, where the size and shape of nanomaterials are strongly related with the preparation conditions. Since the NPs have high surface energy and large surface area, the nano-sized particles tend to agglomerate into larger particles through attaching from their surfaces to lower their overall energy and reach the more thermodynamically favored state. In order to stabilize metal NPs against agglomeration, a variety of surfactants or capping agents, which form a steric and/or electrostatic protection layer around the particles, are added into aqueous and/or organic reaction media.[90]

When the size of metal particles are reduced from the well-ordered bulk crystalline to structures in the nanometer scale, they exhibit unique properties over the bulk; their physicochemical properties as well as electronic properties, and the interrelated optical properties are different.[91, 92] The NPs' intrinsic properties are dominated by their high surface energy (unsaturated nano-sized metal particles are in higher energy state than the entirely coordinated atoms in the crystal structure of the bulk) and their high surface to volume ratio.[93] In addition, NPs' novel physicochemical properties are strongly related with the size of particles. As

a basic background, the metals in bulk form in millimeter scales or larger, do not have discrete energy levels and have no band gap in their electronic structure. In contrast, metals in molecular form have a large band gap between valance and conduction bands. Unlike the metals in bulk or molecular form, metal NPs have discrete energy levels and a small band gap.[90, 94]

1.2.2.2. UV-visible Spectra of Metal Nanoparticles

Illumination of a sample with electromagnetic radiation, results in absorption, reflection or scattering of incoming radiation. The absorbed amount of incoming electromagnetic radiation as a function the wavelength of incident beam is measured in absorbance spectroscopy through relating the intensity of the transmitted light to the incoming light. Beer's Law, also known as Beer-Lambert Law, defines the absorption quantitatively as a function of path length *b* and concentration of absorbing species *c* (see Figure 4). The term Ɛ in Beer's Law represents the extinction coefficient, which is a material specific property, interconnected with the strength of absorbing species to absorb light at a given wavelength interval.

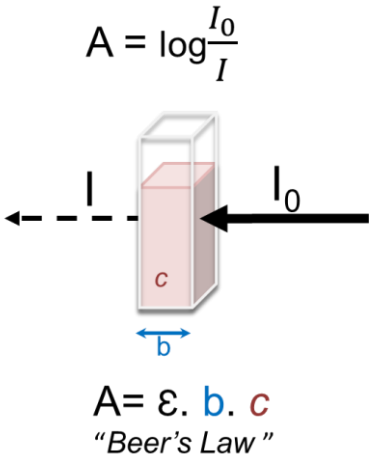

Figure 4. Schematic representation corresponding to adsorption of incoming radiation I_0 through a solution and transmitted light I.

The absorption spectroscopy using the ultra violet (UV) – visible (vis) region of the electromagnetic spectrum for incident beam is called as "*UV-visible (UV-vis) absorption spectroscopy*" and has widespread applications in all branches of science; biology, engineering, physics, chemistry, etc. UV-vis spectroscopy arises as the most common tool for the characterization of metal NPs, because the absorption of light by these NPs is specific to the material. As the electronic structure of the metals is changed with respect to the size of the particles, their interaction with light is also altered. The free electrons in metals start to oscillate when they interact with the incoming light in resonance. The so-called Surface Plasmon Resonance (SPR) is known as the collective free-electron oscillations in the conduction band. The SPR absorbance of the noble metal NPs is in visible region that give rise to their fascinating colors. The "gold color" of the Au-metal as in the bulk, turns into bright-red for its nanoparticles. Since SPR is a surface related property the color is not only varied with the type of the metal NPs but also with the size and shape of NPs. For instance, Ag NPs around 40-60 nm size show an intense-yellow color and their SPR appears as a band around 420 nm in absorbance spectrum, yet the spectrum shifts to 400 nm when the size of Ag NPs is around 5 nm and the color of NPs solution becomes lighter yellow.[94] In absorption spectrum of the nearly mono-dispersed 1-4 nm Au NPs, SPR arises below 525 nm whereas the larger particles give sharper and more intense peak at higher wavelengths.[95] Spherical Au NPs of their size higher than 5 nm, have characteristic absorption band between 520 nm to 580 nm but Au particles in nano-rod form span an absorption range from 700 nm to 1100 nm as the size of the Au nano-rods increased.[89] However as it will be discussed in this

thesis, Au NPs prepared in ILs have usually their SPR bands in much lower (450-500 nm) wavelengths range.[96]

1.2.2.3. Transmission Electron Microscopy of Metal Nanoparticles

Interaction of electrons with matter as electrons are passing through the very thin sample is the subject of interest for different characterization technique. The change in the amplitude and intensity of the electron beam is converted into light intensity by Transmission Electron Microscopy (TEM) to acquire morphological information. The resolution of the imaging is strongly linked to the wavelength of the electrons through the De Broglie's well-known equation,

$$\lambda = \frac{h}{mv}$$

where h is Planck constant, m is the mass and v is velocity of the electron. De Broglie' equation states that as the accelerating voltage corresponding to the energy of electrons in the electron microscope is increased the velocity of electrons also increases, thus the de Broglie wavelength of an electron turns to be shorter (for example for 100 keV electron λ is 4 pm) where the diameter of an atom is typically 30-300 pm for isolated neutral atoms.[97] Accordingly, TEM appears to be a very high resolution tool for morphological characterization of nano-sized metal particles since their sizes and shapes are imperative for further applications. As a result, TEM offers structural identification of a single NP with less than 1 nm resolution. In addition, it offers characterizations of atomic lattices within the particles at atomic resolution.[98]

1.2.2.4. Use of Ionic Liquids for Metal Nanoparticle Synthesis

For practical and innovative applications, metal NPs must be initially synthesized successfully, then be dispersed in the medium of interest and must also be protected against agglomeration. The metal NPs preparation requires reproducibility, reliability, simple reaction conditions yielding NPs in narrow size distribution and desired shapes. ILs as being an innovative matrix whose functions and properties can be fine tuned for particular purposes, also appear to be suitable medium for NPs' synthesis. The natural pre-organized structure within the ILs is formed through extended H-bonding, electrostatic and van der Waals interactions among the constituent ions.[99-101] The extremely structured IL organization consisting of ionic channel networks with high directionality and polarizability makes ILs supramolecular networks an entropic driver for nano-scale structure's preparation and their dispersion.[102-107] Since both polar and non-polar nano-domains exist in the same supramolecular network, ionic metal precursors have tendencies to be dissolved in IL medium. Thus basic reduction methods; where chemicals or photon beam irradiation are generally used as reductants, are also applicable to obtain metal NPs from metal ions dissolved in ILs. Tsuda and co-workers reported on the reduction of Au^{3+} ions dissolved in three different types of ILs by electron beam and γ-ray irradiation and presented the characteristics broad SPR absorbance of Au NPs consistent with TEM analysis.[96] Similarly, reduction of Au^{3+} ions by a chemical reductant $SnCl_2$ in ILs, and Au NP growth, as well as their dispersion to 2.6 to 200 nm, were studied by following the Au NPs' absorbance band in UV/vis spectrometry and complementary TEM analysis.[40]

The non-polar domains of the highly directional nano-network in ILs support decomposition of neutral organometallic precursors into nano-sized metal NPs. Scariot et al. used this high directionality of the pre-organized IL structure to obtain Co NPs in cubic and irregular shapes by the thermal decomposition of $Co_2(CO)_8$ organometallic complex with Co at zero oxidation state.[108] Preparation of different metal NPs from their metal-carbonyl complexes through photolytic decomposition along with the thermal decomposition, was reported by Krämer et al. (for Fe, Ru and Os NPs) [39] and Redel et al. (Cr, Mo and W).[109] Alternatively, ILs are used as not only supporting but also stabilizing media for finely dispersed NPs that are obtained from the bulk metal precursor bombardment with energetic ion and/or photon beams. In the work published by Torimoto et al., finely dispersed Au NPs (around 1.9 nm and 5.5 nm) were prepared by sputter deposition technique, where the ejected nano-sized Au particles are found to be dispersed as clusters on the surface of the particular IL.[110] In addition, monometallic Au and Ag NPs as well as bimetallic Au/Ag nano-alloys, in altered fractions, were prepared by bombardment of Au and Ag targets.[111] As an alternative approach, Endres and co-workers, for the first time, reported on the electrodeposition of metal and alloys in ILs, for NPs such as Mg, Ti, Si or Ge where their electrodeposition is only possible under high temperatures and in molten salts.[41, 42]

Since ILs have large electrochemical stability windows, they also provide electrochemical reaction media to work under low temperatures. Thus they open a wide window in providing metal particles synthesis that cannot be electrodeposited from aqueous and/or organic electrolyte solutions or at room temperature. Imidazolium-derivative ionic liquids were used as templates for the

electrochemical reduction of $Ag(CN)^-$ and $Au(CN)^-$ anions to form both Ag and Au NPs in a size controlled manner, through controlling of the potential and the current density during electrodeposition.[112] Similarly, electrochemical depositions of Se, In, Cu and Al were also studied in ILs without any additives at room temperature where their favorable dispersion was also confirmed by SEM analysis.[113, 114]

Therefore, ILs emerge to as a green synthesis and stabilization medium for NPs preparation through their characteristics, since ILs combine the electrostatic stabilization as they are composed of merely ions, and steric stabilization through restriction of NPs' free motion by the ionic fragments.[115] Thus, if ILs are used for reaction medium there is no need for additional stabilizing agents during preparation processes. Hence, ILs eliminate the possibility of byproduct formation, residual constituents or side reactions with the additives. Moreover, as reported by Gao and co-workers on preparation of Au nano- and micro-structures through the reduction of $AuCl_4^-$ ions, ILs facilitate spontaneous formation of metal NPs without the need for reducing agents.[116] Additional research showed that, Cu flakes with the size of 1-5 μm spontaneously dissociated into Cu NPs (~10 nm) on account of strong interaction between the partially positive Cu-surface and anionic fragment of the IL, and they are dispersed and stabilized within the IL-medium. [117]

1.3. X-ray Photoelectron Spectroscopy and Ionic Liquids

1.3.1. Basic Principles of X-ray Photoelectron Spectroscopy

In X-ray Photoelectron Spectroscopy (XPS), the sample is irradiated by X-ray with a known energy, and as a result photoelectrons are generated. Al Kα and Mg Kα with energies of 1486.6 eV and 1253.6 eV respectively, are the conventional X-ray sources for excitation of photoelectrons. XPS studies are performed under ultra high vacuum conditions around 10^{-7} to 10^{-10} mbar, since gaseous atoms/molecules at higher pressure conditions hinder the precision of measurements through interaction of the residual gases with the emitted photoelectrons. The ejected photoelectrons from the sample, which are detected by a particle detector, are measured to determine their kinetic energies (E_K). The binding energies (E_B) of those photoelectrons are computed using the *Einstein's equation*; $E_B = h\nu - E_K - \Phi$, where $h\nu$ is energy of the X-ray photons and Φ is the spectrometer work function, since the Fermi levels of sample and spectrometer are equalized. (See Scheme 1 for E_B correlations with the work function).

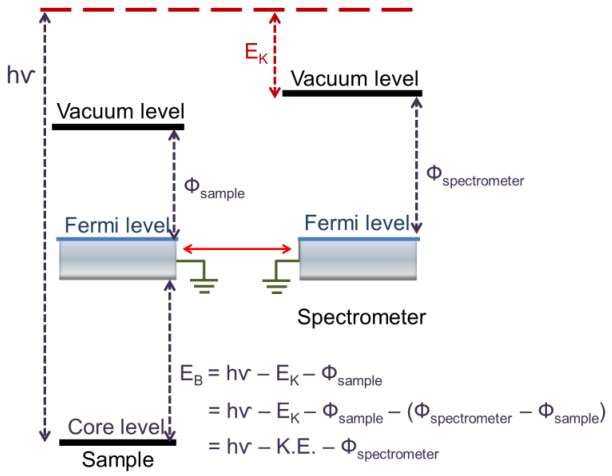

Scheme 1. Schematic illustration of relation between the energy levels and the work function in XPS for the sample (left), the spectrometer (right).

Binding energy of a specific energy level is different for each atom and is also a function of chemical environment. Therefore, information about each element, except for H, can be obtained using XPS. The incoming photons permeate through the sample in the microns range. The interaction between the outgoing beam and the material of interest is strong so that only a fraction of the ejected photoelectrons originating from the top few nanometers depth of the sample's surface can survive without energy loss through inelastic scattering. The characteristic photoelectron peaks arise from those of electrons leaving the surface without energy loss. The other ejected but inelastically scattered electrons contribute to the background of the spectrum as depicted in Figure 5. Hence, chemical and physical information of the sample are collected from about few outermost atomic layers. In others words XPS has 0-10 nm probe length, of the sample's surface. In addition using the elemental specific property of XPS, relative amounts of corresponding elements can also be determined.

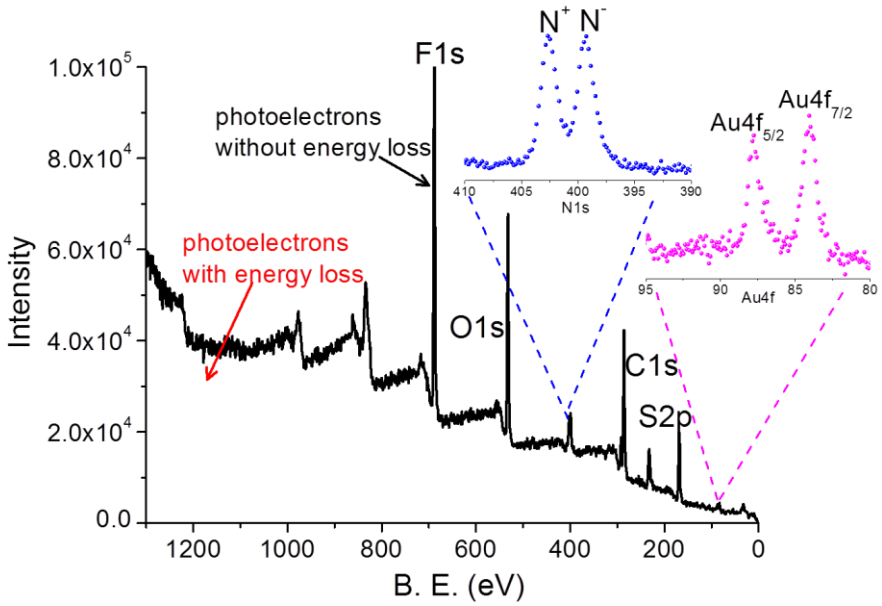

Figure 5. XP survey of DEME-TFSI on Au-electrode representing the photoelectrons' contribution to the spectrum and the detected elements. High resolution Au4f and N1s regions are given inlet.

In the high resolution mode (see Figure 5 inset), the photoelectron spectrum of a specific element contains information about its chemical or electronic environment. The oxidation state of an atom shifts the binding energy toward higher values, since positively charged atoms have strongly bound electrons and toward lower binding energy in case of negatively charged atoms that have less strongly bound electrons, as presented for N1s region in Figure5. Therefore, not only information on identification and quantification of the same element but also information about the chemical environment can be harvested by XPS analysis. Along with the elemental and chemical sensivity of XPS, additional information is extracted by elemental mapping from a defined area on sample surface.

At the surface of the sample the detected XPS signal, (I) is related to the intensity of the XPS signal (I_0) originating from the underlying substrate, after attenuation through the overlayer with a thickness of d using the following equation:[118-120]

$$I = I_0\, e^{-\left(\frac{d}{\lambda \cos\theta}\right)}$$

The attenuation length, λ are tabulated in the literature for many materials and the angle θ is the electron take-off angle normal to the surface which is adjustable for Angle Resolved XPS (AR-XPS) analysis. When the XPS measurements are performed at electron take-off angle θ = 0˚, where collection angle perpendicular to the surface) analysis depth of ~3λ is achieved. By varying the angle θ analysis depth is shortened and gives more information about the outer surface region. As represented in the Figure 5, θ dependent XPS measurements become extremely surface sensitive and are performed with changing the angle where the limiting

value for analyses depth is d≅3λcosθ.[119] For instance, if the typical probing depth of XPS at electron collection angle is ~10 nm, the probed depth is decreased to ~3 nm at 70˚ electron take-off angle. Being a non-destructive technique, AR-XPS reveals information from different depths of the sample by changing only the emission angle at which electrons are collected. Therefore, in addition to information about the element and chemical state distribution at different depths, AR-XPS extracts information about the thickness and relative composition in the sample as a depth profile.

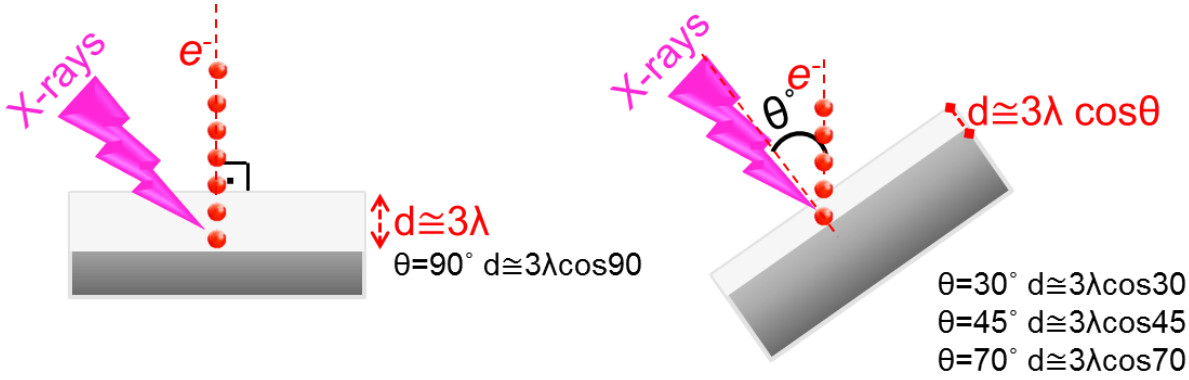

Scheme 2. Schematic representation of Angle Resolved XPS and the sampling depth.

As an example, AR-XPS analysis for N1s regions of the DEME-TFSI ionic liquid, recorded at two electron take off angles θ = 0˚ and θ = 45˚ are given in Figure 6. The N1s region of DEME-TFSI contains two distinct nitrogen species corresponding to the anion and the cation within the IL structure. The intensity of negatively charged $-N^-$ fragment corresponding to TFSI anion, was found to be higher at θ = 45˚ as compared to the intensity of $-N^+$ fragment. As it is revealed from the Figure 6, the anionic fragments dominate the surface when the underlying substrate was negatively charged. Cremer et al. studied adsorption of

imidazolium derived IL's thin films on Au (111) surface.[121] They calculated the thicknesses of the adsorbed IL-films from the intensity relation of the underlying substrate's Au4f peaks as a function of electron take-off angle, as described above. They showed by observing the decrease in the photoelectron peak intensities of the imidazolium cation at θ = 80˚ in AR-XPS analysis, TFSI anion of the IL was positioned towards the surface, similar to our work.

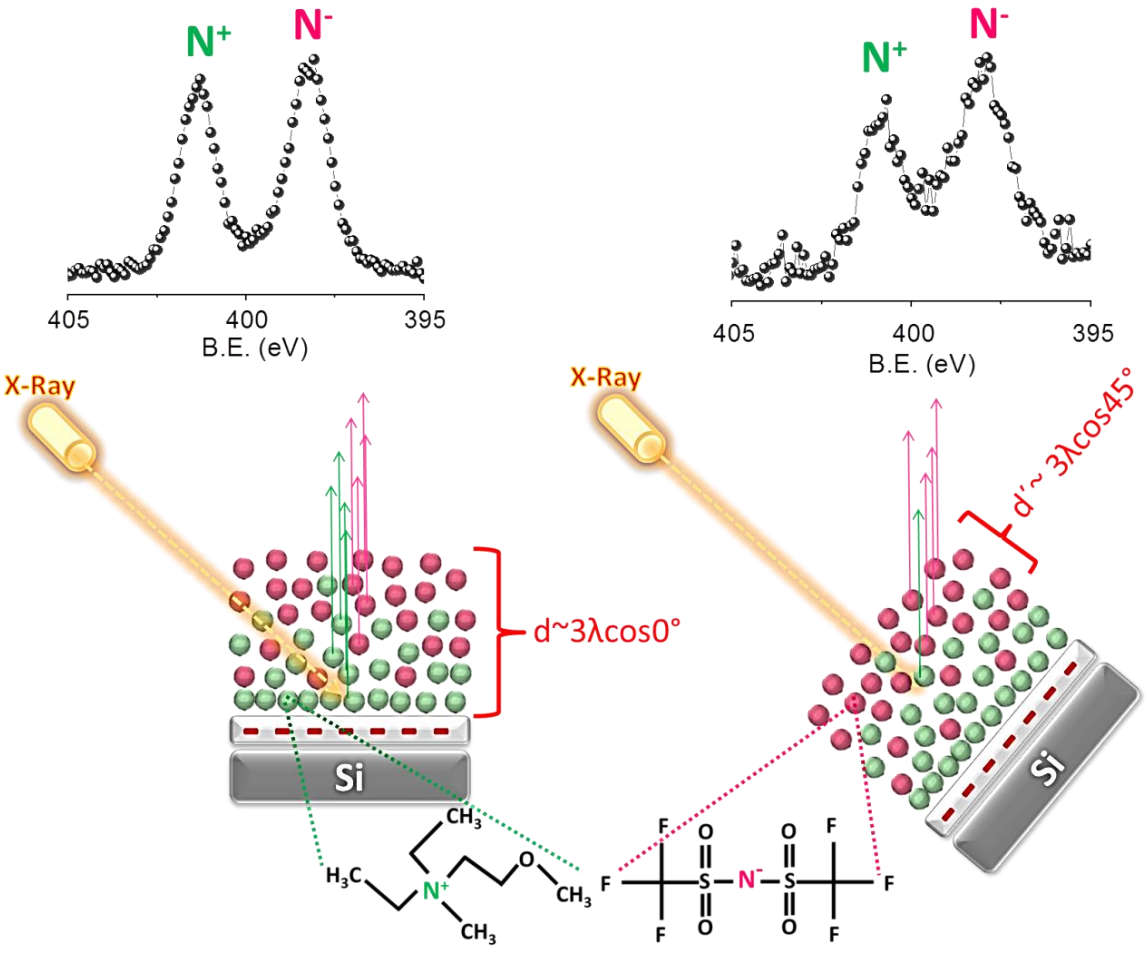

Figure 6. AR-XPS spectra for ionic liquid DEME-TFSI at electron take-off angle normal to the surface θ =0 (left side) and θ=45 (right side). N1s region at two different electron take-off angles represented together with the schematic illustration of the AR-XPS method.

1.3.2. Alternative Use of XPS

When a photoelectron is ejected from the grounded sample it leaves a positively charged surface behind. Subsequently, a potential difference is developed between the sample and earth that causes surface charging, and this positive charge is neutralized in conducting samples rapidly with the electron flow from the earth to the sample. For the non-conducting samples, the positive charge left on the surface as a result of electron ejection is compensated by an additional low energy electron source in the spectrometer in conventional use. On the other hand, careful control of the surface charging facilitates obtaining additional information from the surface. As an alternative approach, application of external bias to the sample utilizes the sign and the extent of developed charges on the surface. Response of electrolytes to an external electrical stimulus depends not only on the structural properties of electrolytes but also their electrical properties. Therefore additional information about electrical and structural properties of ILs can be acquired by control of applied external voltage as described in our previous works.[122-124] In addition to obtaining conventional properties by XPS measurements, we are able to extract further electrical information about the sample by recording the XPS spectra under application of external electrical stimuli. Surface charging as a result of external D.C. voltage stress application can be used as a tool to obtain information about the surface structures at various voltages. Positions of photoelectron peaks shift under external potential application. For the conductive materials the displacement in peak position is as much as the bias applied in a linear fashion whereas non-linear trends are usually observed for poorly-conductive or non-conductive materials.

The XPS studies regarding charging as a tool under use of a time varying external bias are named as “Dynamic XPS Measurements”.[122, 125, 126] Time dependent Dynamic XPS analysis is performed under voltage stimuli in the form of square wave (SQW) pulses.[124, 127-130] As it will be demonstrated below, Dynamic XPS measurements allow investigation of interfacial structure between IL and electrified electrode, while giving adequate amount of time for the structural rearrangement to take place within the IL upon application voltage stimuli. In short, during the XPS study the charge built up is additionally controlled by applying external voltage and the sign of the developed charge on the material of interest is turned from positively charged state to negatively charged state by switching the sign of applied potential.

Applying 1 V to the sample leads to 1 eV alteration in binding energy positions. For instance, when external voltage of +5.0 V is applied to a conductive sample (Au metal in the present case) peak positions are shifted to the higher binding energy positions by exactly 5.0 eV. If the sign of the applied 5 V potential is switched to negative, negative charge accumulates on the sample surface then the peak position are shifted to lower binding energy positions and the overall shift is exactly 5.0 eV for conductive materials but smaller for non-conductive materials. Figure 7 (a) shows the grounded Au 4f spin orbit doublet with the $4f_{7/2}$ component at 84.0 eV. When +5 V D.C. potential is applied to the Au metal, the corresponding binding energy shifts to 89.0 eV. The peak position shifts to 81.0 eV when the sign of potential is reversed [Figure 7 (b)]. Application of external square wave (SQW) pulses, that is alternating potentials at a given frequency and amplitude, enables the time dependent analyses of surface charging by switching the applied potential with variable time intervals. In this case, positive /negative

voltage application together causes splitting of photoelectron peaks into two components at higher and lower binding energies [Figure 7 (c)], respectively.

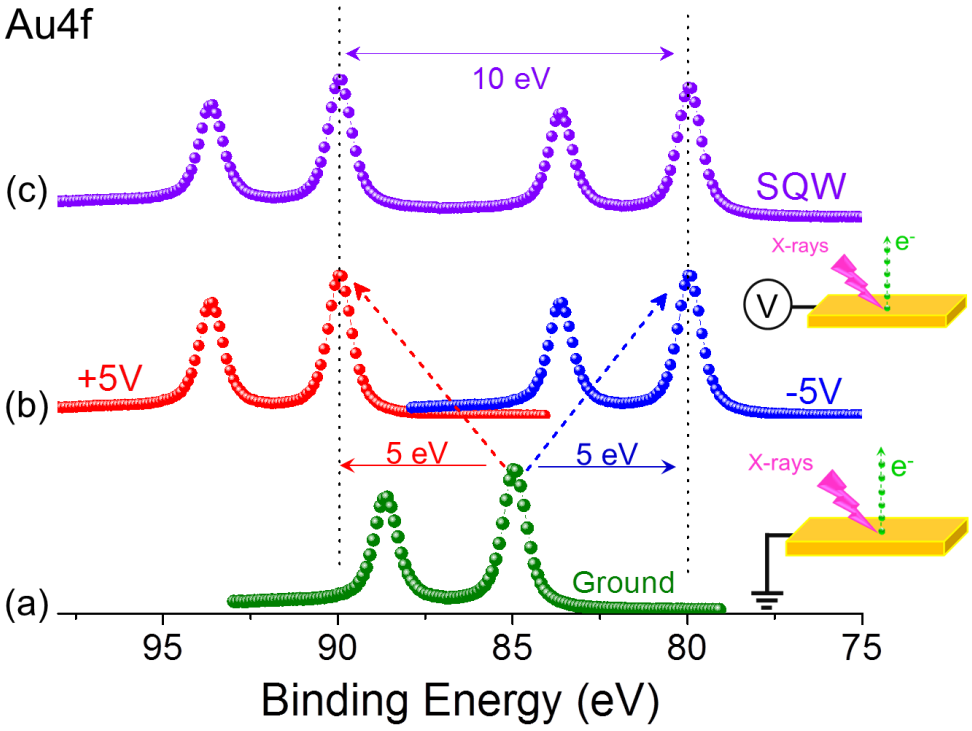

Figure 7. XPS spectra of a conducting gold metal's Au4f region when sample is (a) grounded, (b) subjected to +5V and -5V D.C. voltage bias and (c) SQW excitation of 5V amplitude with 1 kHz frequency.

The frequency of usable pulses ranges in 10^{5} to 10^{-3} Hz for the sample under investigation and for the spectrometer used. For example, when a measurement at 10 mHz SQW with an amplitude of 5 V is performed, sample is exposed to +5V as soon as the positive cycle starts and feels this bias for 50 seconds. During the next 50 seconds the sample is exposed to -5V. In the resulting photoelectron spectrum all peaks are twinned, and the difference between the

splitted peaks is exactly 10.0 eV for conductive samples and but can be smaller than 10.0 eV for non-conductive, charging samples.[124]

1.3.3. Ionic Liquids and XPS

The surface properties of a particular IL dominate the overall properties of the system. Hence, further understanding of the ILs' surfaces has a great significance for their applications. In general surface sensitive techniques rely on the analysis of ions or electrons, hence they require ultra high vacuum (UHV) conditions to work properly for not hindering the propagation of ions or electrons. Therefore, investigation of liquids, e.g. liquid electrolytes in electrochemical systems is not compatible with UHV conditions due to their high vapor pressures. The high ionic conductivity, non-volatility, high chemical stability and negligible vapor pressure properties of ILs make them suitable candidates for UHV analysis. XPS is a surface analysis technique of ILs at the molecular level since;[131, 132]

i. ILs are conducting, no charge neutralization is required during XPS analysis.
ii. ILs are stable under X-ray illumination, where any X-ray beam destruction and/or visible physical change have not been reported so far.
iii. ILs emit adequate photoelectron flux, so that valuable data can be acquired in a short experimental time interval without any change in peak shapes and stoichiometry.

Any surface contamination or impurities are also certainly detectable (above 1% atomic level) through following the XPS peaks of the characteristic elements other than those of the ILs. In addition, the chemical state and the surface composition of the atomic constituents of ILs give insight to understanding of their impurity levels. For example, carbon is a common impurity atom, hence deviation from the stoichiometry of the IL's C1s signal points out the presence of impurities. The chemical specificity of the XPS technique, together with a variable depth information in the nm range, achieved by recording the data at grazing angles (Angle-Resolved XPS or AR-XPS), give detailed information about structure, preferential location of the ionic constituents and reactivity of the ILs.[131-138] Maier and co-workers, investigated the dissolved Pt metal precursor in an imidazolium derived IL, together with the purity of the IL-system, using two different emission angles.[139] They reported that the Pt ions were found to be enriched at the top-surface of IL. In the recent work of Caporali et al.[140] metal-bistrifilimide salts dissolved in bistrifilimide derived IL were analyzed by XPS at normal emission and grazing emission (angles of 90˚ and 10˚ respectively). They found that there exists a surface enrichment of anion upon the addition of the metal salt, with respect to the cation of the IL. Also regarding to the chemical shifts in the binding energy positions, authors discussed the strength of the chemical bonds formed between the anionic fragment of the IL and the inserted metal ion.

1.3.3.1. *In-situ* XPS Analysis for Ionic Liquids

The conventional electrochemical systems cannot be investigated in ultra high vacuum chambers because of the common shortcomings of aqueous and/or organic electrolytes such as volatility or chemical instability. Hence, the investigation of the electrochemical systems turns into ex-situ analysis and is not in real time. When these solvents are replaced by ILs, the electrochemical systems turn into accessible arrangements for *in-vacuo* and *in-situ* spectro-electrochemical analysis, to shed light on the effect of electrochemical reactions in the electronic structure of the atoms using the shifts in the core-levels. For example, the *in-situ* liquid phase reactions can be monitored by XPS through the binding energy shifts as a result of chemical state changes due to the electrochemical reactions. *In-situ* reduction of the Pd^{2+} ions to Pd^{0} species, under X-ray exposure was monitored for the first time in a liquid state-electrochemical XPS analysis work thru following change in the Pd3d photoelectron signal intensities corresponding to a decrease in the intensity of Pd^{2+} and the increase in Pd^{0}, where the binding energy position of two oxidations states were well resolved.[132] Licence et al.[141] monitored the electrochemical reduction of Fe^{3+} species to Fe^{2+} in two electrode electrochemical cell using an externally connected potentiostat in real time, by following the XPS peak changes in the oxidation states of the photoelectron peaks together with cyclic voltammograms recorded inside the chamber. In their following work, the dissolution of copper-metal and the electrochemical formation of cationic Cu^{+} species were identified by XPS in a time dependent fashion thru following the intensification of the photoelectron peak in the both survey and high resolution Cu2p region under anodic polarization.[137]

Compton and his co-workers studied for the first time, the electrodeposition of potassium metal in the electrochemical cell containing potassium salt dissolved in a IL connected to the potentiostat while recording the K2s high resolution spectra by *in-situ* XPS with respect to time and showed the increase in the intensity of K2s photoelectron peak at K-metal electrodeposition potential.[142] Subsequently, they studied the electrodeposition of another Group 1A metal, rubidium, that cannot be electrodeposited from aqueous or organic solvents because of their narrow electrochemical potential windows and the highly active nature of Rb.[143] They monitored not only the increase in the intensity of Rb3d within time but also the decomposition of IL, as a result of decrease in intensity of the photoelectron peaks corresponding to anion under cathodic polarization, as a function of the applied current.

1.3.3.2. XPS for Ionic Liquid Interfaces

The chemical composition and the molecular orientation of the ionic constituents within the ILs structure at the IL-interface differ from those of bulk. In addition to the physicochemical properties of ILs, their interfacial region is of utmost interest. XPS is an outstanding technique to analyze interfacial structure of IL systems beyond the macroscopic properties of the ILs to understand the molecular orientation and surface structures because of the high atomic photoelectron emissions of ILs, and the quantitative nature of the technique.[131-134, 136, 138] Also, because of the fact that the ILs' interfacial structure analysis needs to be performed in a very small time scale which should be smaller than the Brownian motion of the molecules at the interface, [144] XPS is a prevailing

technique that is based on the fast photoelectron ejection process. Caporali and co-workers studied, as an important contribution to the literature, the structure and composition of outermost IL layers at the IL/vacuum interface by XPS together with low energy ion scattering (LEIS).[145]

However, most XPS measurements have been carried out without deliberate electrification of the surfaces, except for the work of Foelske-Schmitz et al., where it was demonstrated for the first time that the IL/vacuum interfaces could be electrified by imposing a potentiostatically controlled D.C. bias using an electrochemical set-up while recording XPS as the IL rapidly complied to the electrochemical potential imposed.[146, 147]

Upon the electrification of the electrode, cations and anions inside the IL in contact with the electrode undergoes a structural rearrangement at the electrode/electrolyte interface in order to screen the induced charge at the electrode surface, forming the EDL as described in the previous section. The extent of the EDL from the electrode at the steady-state, is short (1-10 nm) which is also influenced by the degree and the sign of electrode-electrification. It was also reported that the electrostatic charge screening through the ion density fluctuations can range up to 40 nm in IL-electrolytes.[148] Moreover, Liu and co-workers reported on the extent of ion l layers screening the charge on electrode surface, is in microns range under electrostatic-actuation in ionic polymer actuators containing ILs.[149] Although the spectral resolution of XPS is not capable of monitoring the EDL directly, as it will be demonstrated below, the screening of the charge at the interface can be monitored in surprisingly large distances up to mm range away from the interface.

1.4. Aim of the Study

As discussed above and beyond, ILs open new routes for further developments of electrochemical energy storage devices which require deeper understanding of their properties. The imidazolium derived ILs have been comprehensively inspected towards fundamental considerations through various spectroscopic, microscopic, electrochemical and theoretical tools such as sum frequency generation technique [53, 62, 150, 151], atomic force microscopy [61, 70, 152], cyclic voltammetry [141] and molecular dynamic simulations [56, 57, 153, 154] along with X-ray photoelectron spectroscopy [137, 155-157]. But there is still plenty of room toward further understanding especially the ILs based electrochemical devices. Since XPS reveals detailed chemical composition, IL-interface and electrochemical reactions taking place within IL containing electrochemical devices, main aim of this thesis work is to use XPS as a tool for innovative analysis.

The scope of thesis can be summarized as follows. XPS will be used as an analytical tool for;

- **i.** Detailed analysis of IL-devices.
- **ii.** Characterization of IL-devices at the molecular level.
- **iii.** Better understanding of the properties of electrode/IL interface.
- **iv.** Providing a different look at the electrical double layer formation and charge screening.
- **v.** Furthering of the information related to the ionic rearrangements at polarized electrode/IL interfaces.

vi. Monitoring of certain i*n-situ* and *in-vacuo* electrochemical reactions.

Therefore, before the analysis of the fundamental aspects, an electrochemical device consisting of metal electrode/IL electrolyte/metal electrode geometry was optimized and constructed to enable the transfer of the device in to the XPS analysis chamber and record the XP spectra under application of electrical stimuli as D.C. potentials and A.C. in square or triangular wave forms. The first part of the present work focuses on the XPS visualization of the electrode potential screening throughout the IL-medium within a device. Thus, the formation and the effect of EDL on the entire electrochemical device with lateral and temporal resolution have been investigated. In the second part, the individual responses of the charged fragments in the IL-structure at the electrified electrode/IL interface have been studied by following the inter-ionic structural rearrangements of anionic and cationic fragments of IL under external electrical stimuli. The last part is subdivided into two sections. Firstly to a detailed study on *in-situ* reaction monitoring within the XPS chamber, and electrochemical production of Au NPs and electro-corrosion phenomena under anodic polarization has been represented. In the last part of this PhD thesis, characterization of reaction products (Au NPs) by an innovative XPS approach will be presented through the response of the F1s and Au4f peaks to the applied electrical potentials corresponding to the IL and Au NPs respectively.

Chapter 2

Experimental

2.1. Materials

20 μm thick porous polyethylene membrane (PEM) (Celgard 2730, Gelon LIB Group) with porosity of 43% was used for the device fabrications. Electrochemistry grade ionic liquid (≥98.5%) DEME-TFSI [*N*,*N*-Diethyl-*N*-methyl-*N*-(2-methoxyethyl) ammonium bis (trifluoromethanesulfonyl) imide] was purchased from Sigma-Aldrich (CAS Number: 464927-84-2). The water used in all experiments is prepared in a three-stage Millipore Milli-Q Synergy 185 purification system.

2.2. Instrumentation

An Agilent Technologies, Cary 300 UV - vis Spectrometer is used for optical spectral measurements through scanning wavelengths 350 - 800 nm region by a data interval 0.167 nm and a scan rate 100 nm / min. A Tecnai F300 tranmission electron microscope at 300 kV beam energy is used to obtain high-angle annular dark field scanning TEM and bright field images. A Thermo Fisher K-Alpha X-ray Photoelectron Spectrometer with monochromatized photon energy of 1486.6 eV is used for all XPS measurements, which samples ~10 nm depth. The spectrometer system is calibrated by taking reference Au4f region of sputter-cleaned reference metal inside the chamber. The lateral resolution of the spectrometer is limited to the X-ray spot size which can be focused down only to 30 μm. For the measurements reported in this thesis, either a 100 μm or a 50 μm spot size is adopted depending on the analysis circumstances. Analysis of samples is performed under X-rays with 45° and analyzer with 90° angle to the sample. No significant X-ray damage has been detected even under focused beam and also in prolonged measurement times of up to 60 hours.

The device is connected either to ground or to a D.C. source for static XPS analysis or to DS340 Function Generator (Stanford Research) for imposing A.C. electrical stimuli, and obtaining dynamical information. Spectra have been recorded using various amplitudes and frequencies, but only 3 and 5 V results will be shown here, which are chosen for spectral clarity. In addition to conventional scanning mode, the instrument can also be used in the snap-shot mode with moderate time resolution down to 0.2 to 1 s, depending on the signal strength. XPS data has been analyzed using Avantage software version 5.31 which is provided by Thermo Fisher Scientific. For the quantitative analysis, atomic

sensitivity factors implemented in to the Avantage database based on Scofied values are used and spectra are fitted with a 30% Gaussian and 70% Lorentzian product function.

2.3. Preparation of Ionic Liquid Devices

The gold electrodes are sputtered on the 20 μm thick porous polyethylene membrane (PEM) using conventional plasma sputter coating under low vacuum environment around 0.15 mbar and 25 mA discharge current for 80 seconds. 5μl of DEME-TFSI is injected to the surface of the PEM between the Au-electrodes, which spreads rapidly and wets even the electrodes. The impregnation of the membrane is performed either from top or bottom of the PEM membrane depending on the particular purpose of the experiment, as represented schematically in Figure 8 (a) and (b).

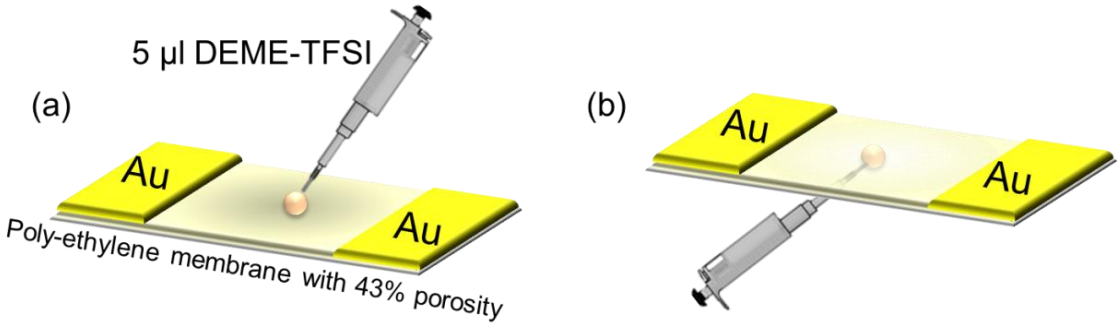

Figure 8. Schematic representation of the electrochemical device with IL impregnation from (a) top and (b) bottom of the device.

For the second device design, a flat Pt electrode is prepared by plasma enhanced-chemical vapor deposition on to a Si-substrate and a bare Au metal in the rod form was cleaned with emery-paper and used as the other electrode. After preparation of metal electrodes, 10µl of the DEME-TFSI liquid is injected in between. The device design is schematically represented in Figure 9.

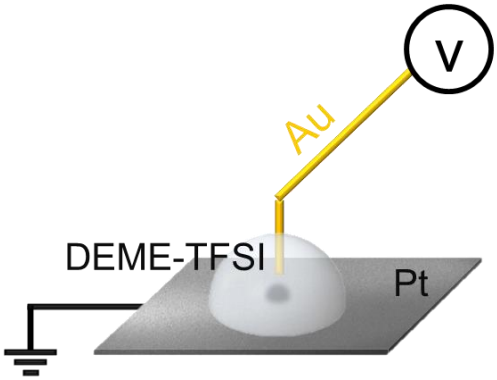

Figure 9. Schematic illustration of experimental set-up to control role of electrode's nature.

2.4. XPS Analysis of IL Devices

For both type of devices, in order to minimize moisture absorption, injection of IL into the device is performed just before the insertion of sample into load-lock chamber of the instrument. Then the pumping is started immediately and entry chamber is pumped down until the pressure around 10^{-7} mbar and subsequently transferred to the main chamber pumping to pressure around 1-3 $x10^{-8}$ mbar. XPS measurements are carried out using the electron spectrometer either grounded or connected to the external electrical sources. IL devices in two electrode geometry were connected from one electrode to the electrical source (source) and grounded from other electrode (drain), as shown in Figure 10.

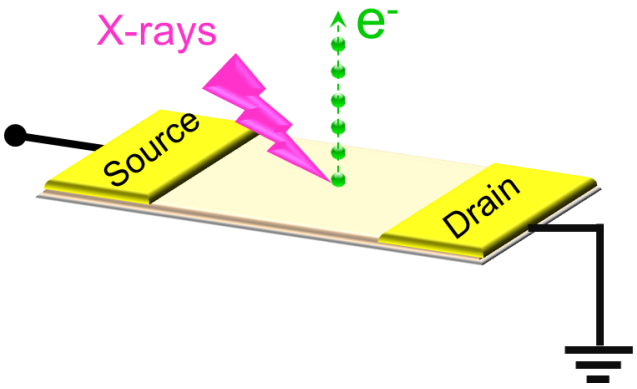

Figure 10. Schematic representation of XPS analysis under external bias application in source-drain design.

2.4.1. Electrode/IL Interfacial Region

Under the D.C. voltage stresses, spectra are recorded in both normal and line scan modes. For A.C. measurements a time-varying electrical signal is applied in the form of square-waves (SQW) with either at a frequency of 1 kHz or 10 mHz, and data are recorded in the snap-shot mode with 1 second intervals. For the external biasing using a triangular wave, the external potential was scanned linearly in time from -5V to +5V with a period of 1000 seconds. In the first round, the spectrum is recorded in order of increasing binding energy of 0.2 eV steps with a dwell time of 100 ms, and in the second round the same region is recorded in the direction of decreasing binding energy, resulting in a time difference of 10 seconds between the two spectra for ensuring correct averaging.

2.4.2. *In-situ* Electrochemical Reaction Monitoring with XPS

Time dependent XPS measurements are performed using the two electrode geometry IL device in the source and the drain (as in same device shown in Figure 8) under application of +3V or -3V D.C. stresses while recording consecutive high resolution XP spectra in the line scan mode starting from the source side and moving to the drain. Line scans are repetitive as samples are subjected to external biasing for up to 36 hours. Afterwards, the potential is switched from positive to negative or vice versa after the desired number of line scans are recorded.

The electrochemical device to control the role of electrode nature in preparation of NPs with Au and Pt electrodes is transferred into XPS chamber and external +3V and afterwards -3V D.C. potentials are applied continuously to the Au-electrode, while Pt-electrode was grounded up to 60 hours under UHV conditions.

For the experiments regarding the XPS characterization after the *in-vacuo* preparation of Au NPs under +3V potential [Figure 11 (a)], 5μl of Au NPs/DEME-TFSI is injected between the two Au electrodes [Figure 11 (b) and (c)], as described in the previous section. The drop containing Au NPs diffuses immediately over the entire device, then it is transferred to the analysis chamber again in the source-drain geometry, to record the temporal and lateral response under D.C. and A.C. potential applications [Figure 11 (d)].

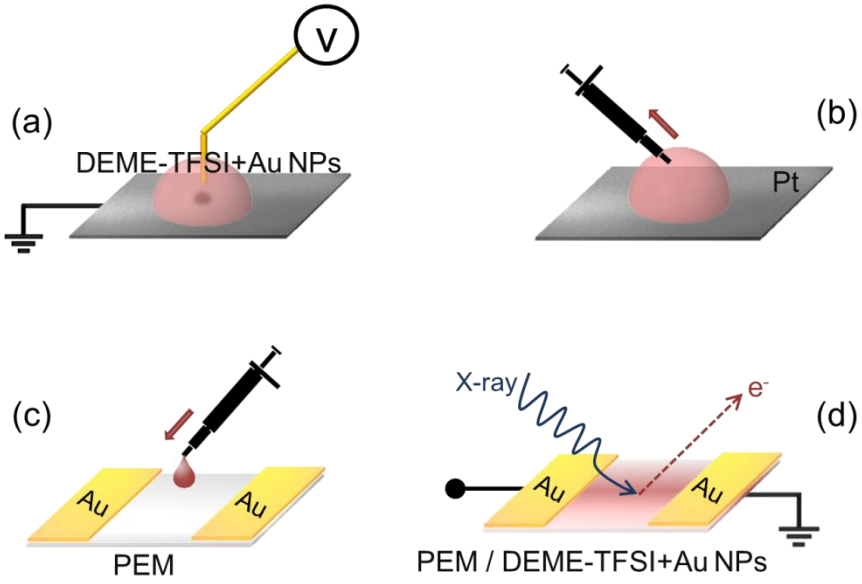

Figure 11. Illustration of experimental steps for analysis of electrochemically prepared Au NPs within the DEME-TFSI.

Chapter 3

Results and Discussions

3.1. XPS Characterization of Ionic Liquid in Electrochemical Device

N,*N* – Diethyl -*N*- methyl -*N*- (2-methoxyethyl) ammonium bis (trifluoromethanesulfonyl) imide, denoted as DEME-TFSI is an aliphatic quaternary ammonium based ionic liquid. DEME group is a flexible asymmetric cation that contains a methoxy-ethly group on nitrogen atom and TFSI group is a bulky imide derivative anion. Although not much interest has been focused on the aliphatic quaternary ammonium containing ILs, they impart greater cathodic stability in electrochemical devices when compared to the aromatic quaternary ammonium derivatives as well as commonly used imidazolium or pyridinium-based ILs, since relatively small size of the aliphatic cation compared with the aromatic ones imparts higher melting point to their high wide EW and high ionic conductivity.[158-162]

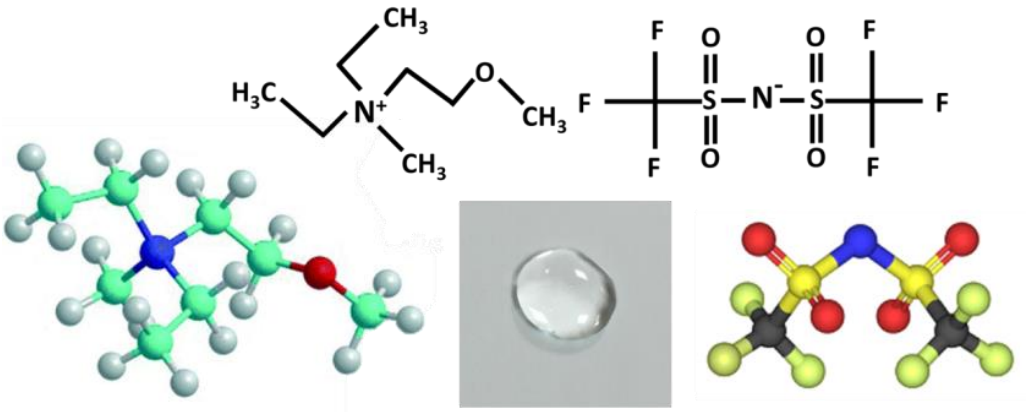

Figure 12. *N*,*N* – Diethyl -*N*- methyl -*N*- (2-methoxyethyl) ammonium bis (trifluoromethanesulfonyl) (DEME-TFSI) and its molecular structure.

A typical XPS survey spectrum, as given in Figure 13, confirms the presence and the stoichiometry of the DEME-TFSI through the elemental identification by the photoelectron peaks of S2p, S2s, C1s, N1s, O1s and F1s, corresponding to S, C, N, O and F atoms present in the chemical structure of DEME-TFSI. All data are acquired without the need of charge compensation since DEME-TFSI as other ILs act as electrical conductors under XPS-analysis conditions. The expected ratios S : C : N : O : F = 1 : 5 : 1 : 2.5 : 3 is found to be in agreement with the stoichiometry S : C : N : O : F = 1.03 : 5.19 : 1 : 2.48 : 3.18, that is derived from the experimental XPS results without any constriction in binding energy and area of the photoelectron peaks. In addition, the survey XP spectrum of the PEM+IL indicates that no major surface impurities exist.

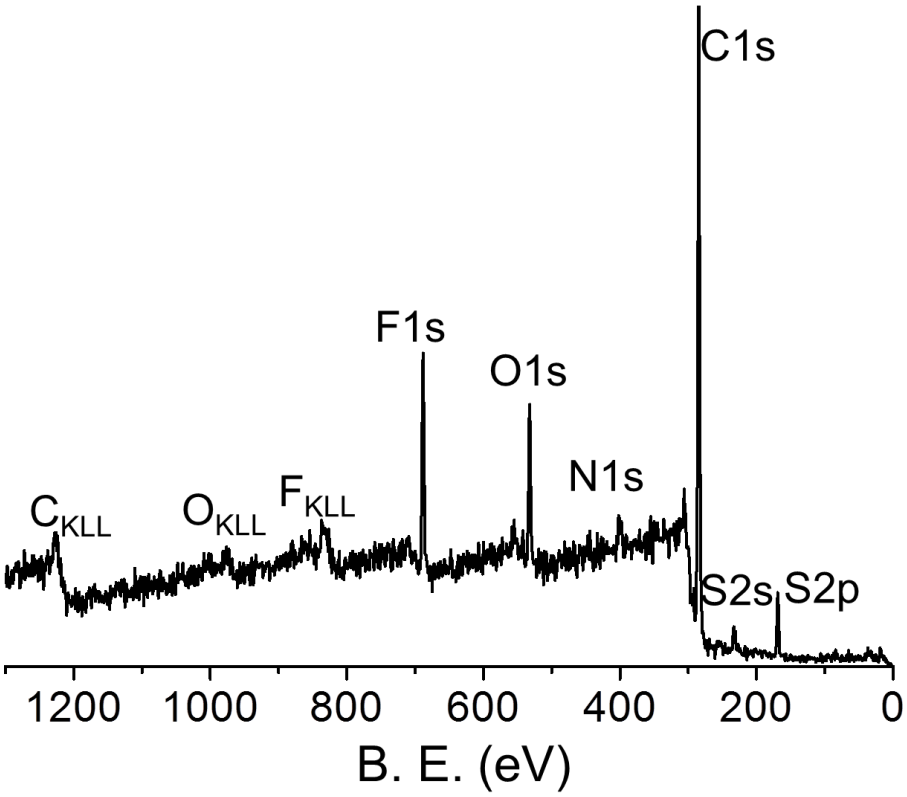

Figure 13. Typical XP survey of ionic liquid DEME-TFSI

In Figure 14 sulphur, fluorine and oxygen core-level XP spectra are presented. The S2p doublet spectrum [Figure 14(a)], where sulphur content only arises from the S-atom in TFSI anion, is fitted with two components corresponding to the spin orbit doublet. In the spectrum of F1s region [Figure 14(b)], only a single - sharp peak is fitted and it is attributed to six equivalent fluorine atoms in the TFSI-fragment of the IL. The O1s region [Figure 14(c)] consists of five-oxygen atoms; one from methoxy-ethyl group and four from the two $–SO_2$ groups.

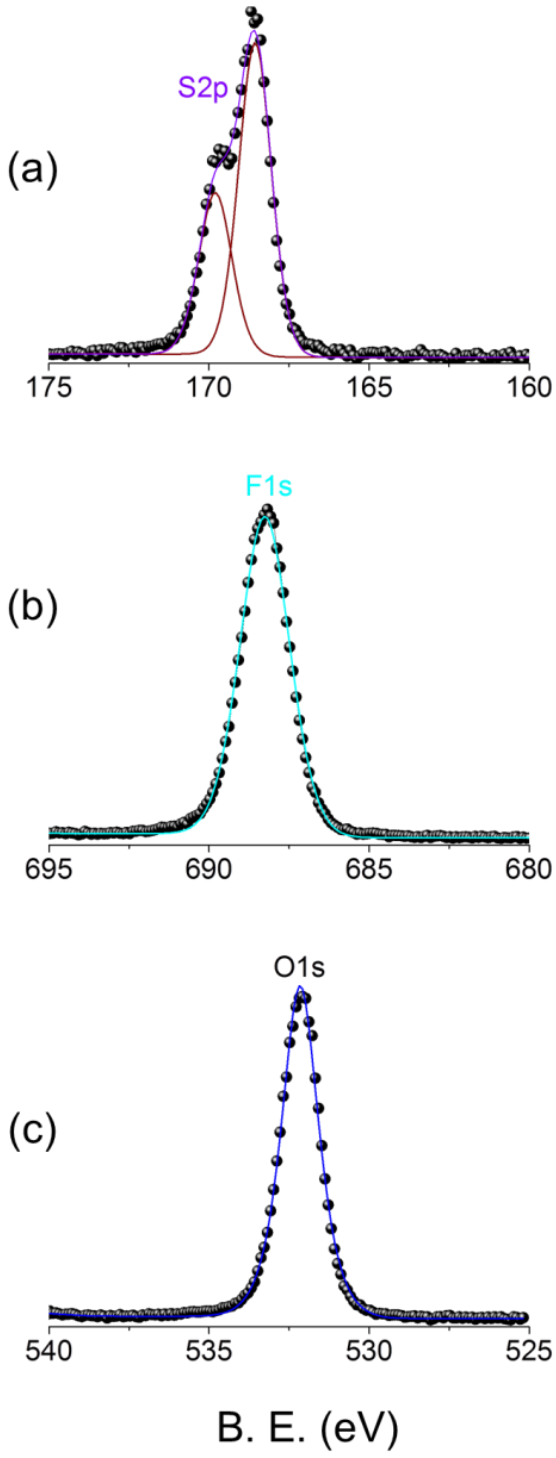

Figure 14. XP spectra of (a) S2p (b) F1s and (c) O1s regions.

DEME-TFSI consist of cationic $–N^{+}$ and anionic $–N^{–}$ fragments correspondingly; thus the well-resolved N1s region was fitted into two different peaks representing the quaternary ammonium $–N^{+}$ and the imidic $–N^{–}$ contributions from the IL-molecular structure. Since the nitrogen of the cationic fragment is more positively charged than the nitrogen of the anionic fragment of DEME-TFSI the photoelectron peak at lower binding energy arises from the negatively charged $–N^{-}$ group and the peak at higher binding energy arises from positively charged $–N^{+}$ group, with the binding energies at 402.0 and 399.0 eV [157], respectively (Figure 15). In the grounded samples the intensity of these two N1s main peaks were measured to be very close to each other with ratio of the groups $–N^{-} / –N^{+} = 1.04$, that is in good agreement of 1:1 stoichiometry in the molecular structure

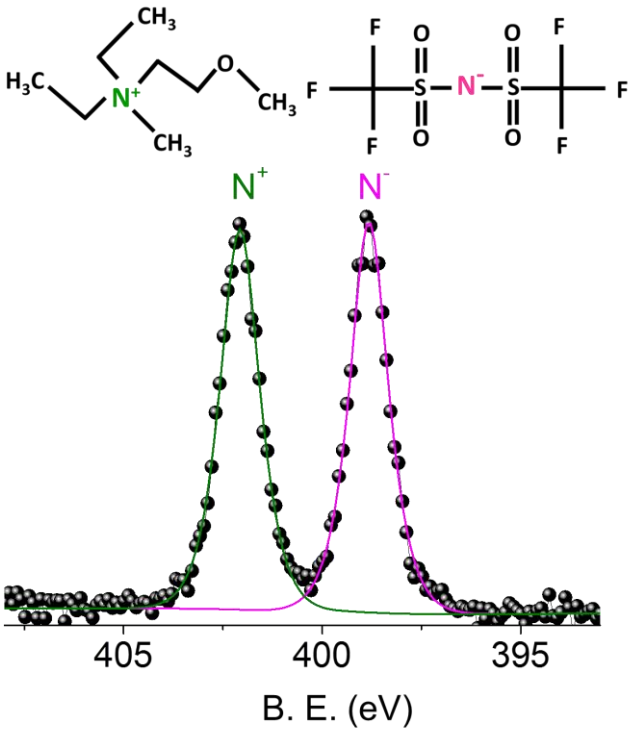

Figure 15. N1s core level XP spectra of DEME- TFSI representing molecular structure and well-resolved two different nitrogen species.

The C1s core level spectrum is fitted into four components (see Figure 16). No constraints are applied for binding energy values, but FWHM values for each peak is constrained to be between 1.0 – 1.5. The relative peak areas of each component is also constrained to be consistent with stoichiometry of DEME-TFSI IL, $C_1 : C_2 : C_3 – CF_3 = 1 : 1 : 2 : 1$. The only contribution from the TFSI anion is from the fluorinated carbon ($–CF_3$) and the C1s peak appears at the highest binding energy of 293.3 eV, upshifted since three bonds are formed with three electronegative fluorine atoms. C_1 peak at 284.8 eV is attributed to the aliphatic carbon in DEME cation. C_2 peak at 285.9 eV corresponds to carbon atom bounded to the oxygen in the methoxy-ethyl group and C_3 peak at 286.4 respectively at a higher binding energy as a result of four carbon atoms bounded to nitrogen atoms in the DEME cation.

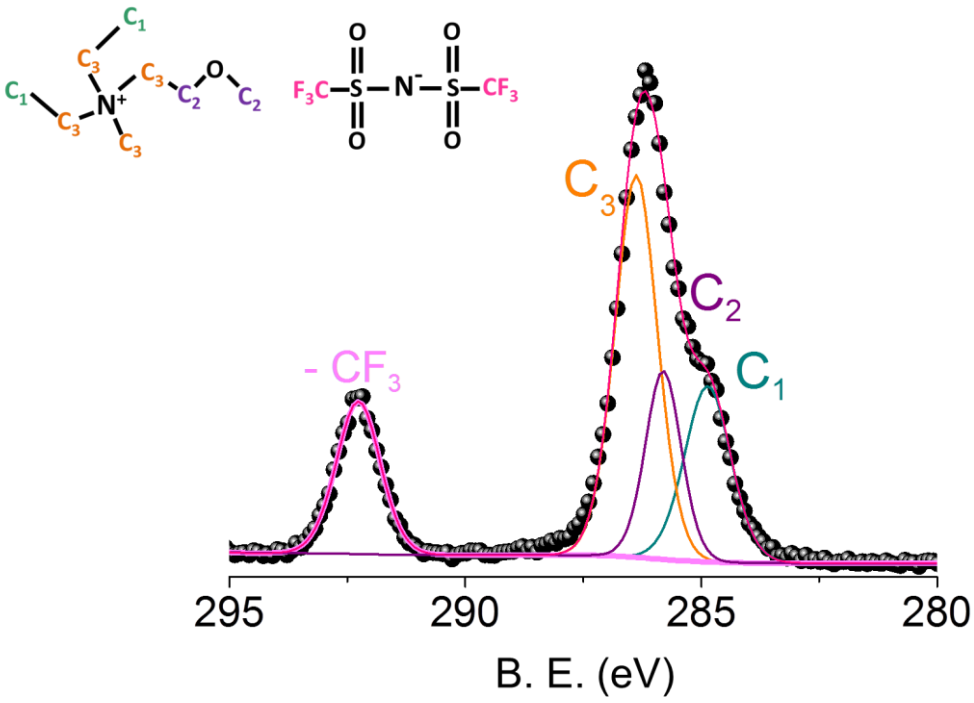

Figure 16. C1s region of DEME-TFSI.

3.2. XPS Study of the Electrified Au Electrode / IL Interface

(This part is also described in M. Camci; P. Aydogan; B. Ulgut; C. Kocabas; S. Suzer, "XPS enables visualization of electrode potential screening in an ionic liquid medium with temporal-and lateral-resolution". Physical Chemistry Chemical Physics, 2016, 18, 28434.

"Reproduced by permission of the PCCP Owner Societies. http://pubs.rsc.org/en/content/articlelanding/2016/cp/c6cp04933h#!divAbstract")

Understanding of charge accumulation and dissipation on electrode-electrolyte interfaces are of utmost importance. It is well-known that when an electrified solid interface is brought in contact with ionic conductors, the surface accumulates opposite charges and forms an electrical double layer (EDL) at the interface. As a result of the advanced research efforts, structure of the EDL down to nanometer scales, and especially intricate changes at interfaces accompanying their electrification has now been brought up to a new level of understanding.[163] Accordingly, at the steady-state the double layer in ILs consists of pronounced charge density oscillations within a short range (1-10 nm) from the electrode surface, which can also be controlled by the sign and/or magnitude of the electrification. By recording electrostatic surface forces, it was recently reported that electrostatic screening can even have a longer range component up to 10-40 nm.[148] In the work of Liu et al., asymmetric ion distribution was found to extend to microns range under electrostatic-actuation in ionic polymer actuators containing ILs.[149]

Monitoring charge accumulation/depletion is an outstanding challenge, and XPS, although an ultra-high vacuum analysis technique provides chemically specific information also for ILs, due to their low vapor pressure together with moderate ionic conductivity at room temperature. In this thesis, we will show that

transient effect(s) of screening of the electrode potentials by ILs can also be measured in similar time domains up to minutes, but at the same time, we will also show that the voltage transients can be measured in a completely surprising and different realm, i.e. up to millimeters range away from the interface, using X-ray photoelectron spectroscopy (XPS).

Also, we present an XPS investigation for probing dynamics of charge screening both in a position- as well as time-dependent fashion across two metal electrodes of a device which has an ionic liquid medium in between. One of the metal electrodes is subjected to various D.C. and/or A.C. electrical pulses to induce static and dynamic electrification, respectively, while the other electrode is grounded. In parallel with these electrical interventions, XPS data is recorded either in the snap-shot mode with 1s time intervals to probe transients, and lower energy resolution, or in conventional longer scanning mode with higher resolution for probing the steady-state behavior, depending on the information sought-after. Data is also recorded in the line-scan mode to obtain position dependent information across the electrodes.

3.2.1. Static XPS Analysis Under D.C. Bias

The DEME-TFSI device is connected either to ground or to a D.C. source for static XPS analysis. Spectra have been recorded using various amplitudes, but only 3 and 5 V results will be shown here, which were chosen for spectral clarity. In addition to conventional scanning mode, the instrument can also be used in the snap-shot mode with moderate time resolution down to 0.2 to 1 s, depending on the signal strength. The imposed potential is screened in time

through formation of the double layer by the mobile ions of the IL medium, which can be followed by XPS measurements. Note that, even though our lateral resolution (30 μm) is not capable of probing the EDL directly, its influence is easily probed by measuring the binding energy position of the F1s, or any other peak of the IL, as shown in Figure 17.

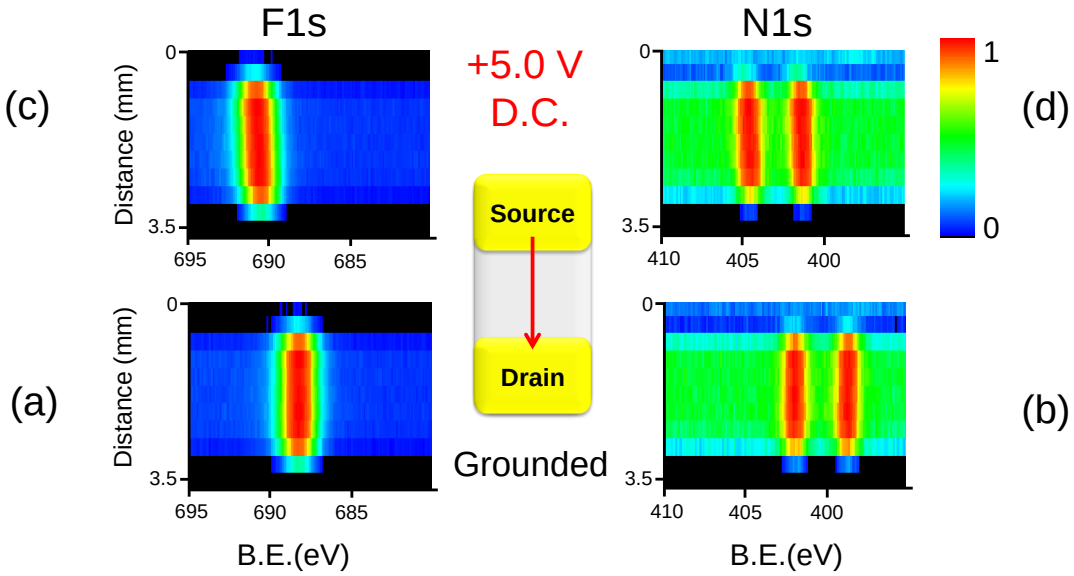

Figure 17. XP Line Scan spectra of F1s and N1s regions between the electrodes when grounded (a) - (b) and when +5 V is applied to one of the electrodes (c) - (d). N1s region has two peaks corresponding to N- and N+ moieties.

Applying +5V positive potential while recording XP spectra as a line scan of F1s and N1s regions corresponding to the elements of DEME-TFSI device, allows to display the steady state surface potential achievement across two Au-electrodes in millimeter range. But for the discussions of this thesis, F1s spectra is chosen to represent the DEME-TFSI IL in electrochemical device since there is only one kind of fluorine specie (-CF_3 in TFSI anion) composed of six-F atoms with high X-ray cross-section and subsequent intense peak in XP spectra

as compared to the other specific elements e.g. sulphur or nitrogen of DEME-TFSI. We have analyzed more than 10 similar IL- devices, with slightly different F1s intensity distribution, but always exhibiting uniformly shifted constant binding energy position. In Figure 18 and other figures below for this section, data of a particular device are presented to emphasize the constancy of the peak position where as intensity hesitates. Au 4f region represents the Au-metal electrode in the discussions of this section. In this work we only have a two electrode cell, and our values refer to the actual potential applied to one of the electrodes, and the local potential is measured in a non-contact fashion via the position of the F1s peak.

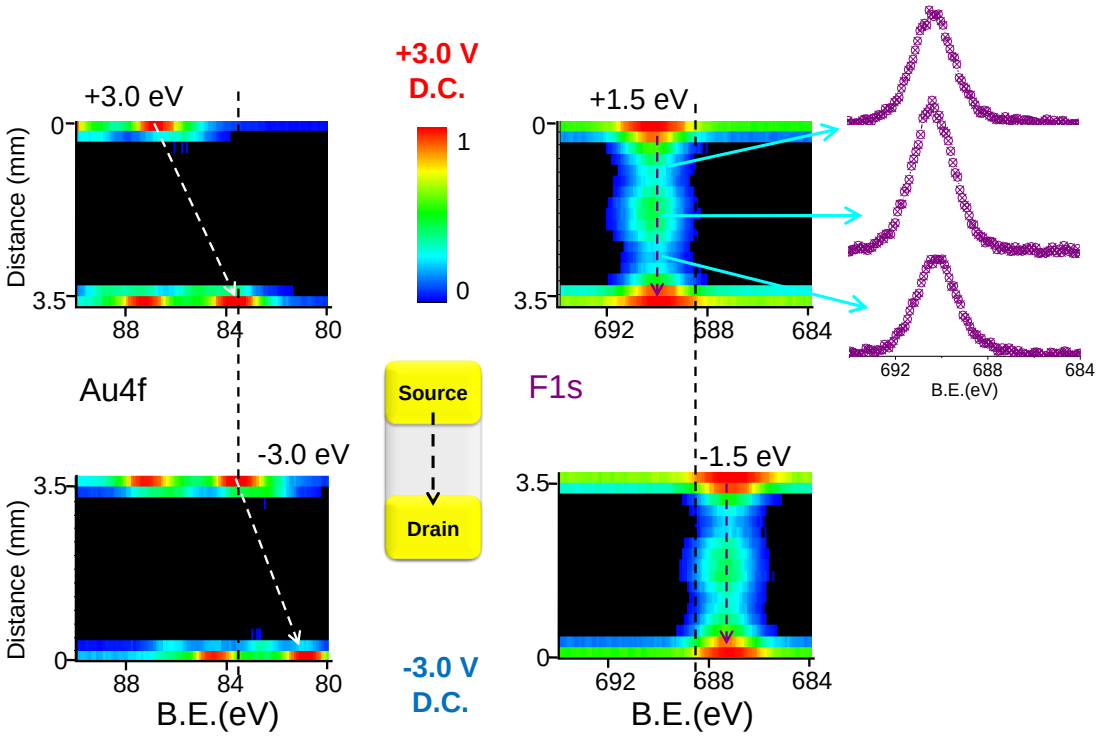

Figure 18. XP spectra of Au4f and F1s regions, recorded in the line scan mode between the two gold electrodes, containing a porous polymer film impregnated with the ionic liquid DEME-TFSI, under the application of +3 (upper part) or -3V (lower part) D.C. bias. The IL is thicker in the middle of the device as reflected by the intensity of the F1s spectra chosen at three representative positions along the line, shown as insets.

As revealed by the Figure 18, a steady-state surface potential is established after formation of the EDL, which is uniform, in the millimeters range, through the entire surface of the IL medium. This finding is interesting since a similar device containing a graphene layer in between the electrodes behaves totally different. C1s core level in Figure 19 corresponding to the graphene layer, is recorded across the Au-electrodes under application of continuous -4 V D.C. potential in line scan mode. It is found to exhibit a smoothly and linearly varying (not constant) value across the two electrodes. Kocabas and Suzer, [164] analyzed the voltage drop variations in a device of single layer graphene on quartz substrates between two gold electrodes. They showed that graphene layer acts as a simple resistive strip between electrodes. These described systems with graphene layer, are far from the EDL concept in ILs but can give insight to further understanding of the steady-state potential achievement in electrified electrode – IL electrolyte devices and the maintenance of this potential through the entire IL-medium.

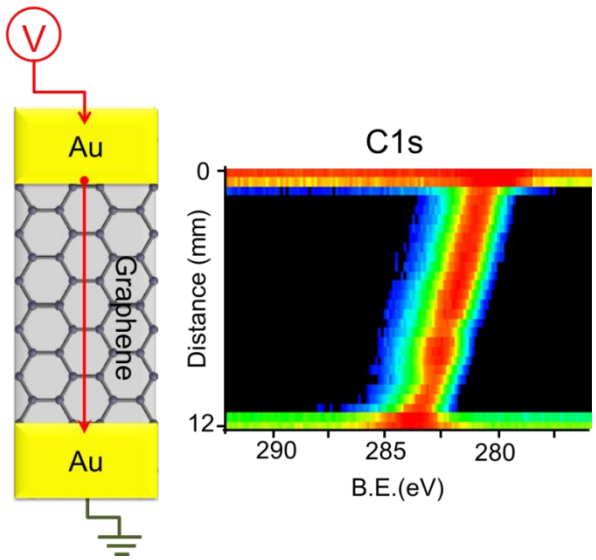

Figure 19. Schematic representation of two-electrode graphene device and smoothly varying voltage change across the electrodes when source electrode was exposed to -4V D.C. potential.

The binding energy of the $Au4f_{7/2}$ peak of electrodes at both sides of the IL-device is 84.0 eV when the spectrometer is grounded. Under D.C. bias, and after equilibrium is established, the corresponding values are measured, at the biased electrode to be 87.0 and 81.0 eV when +3V and -3V are applied to it, respectively, complying totally to the applied bias (i.e. exactly 3.0 eV shift). For the drain-side, no shift is observed in the binding energy position since it is grounded. However, as mentioned above, the F1s and also the other IL peaks such as N1s (given in the Figure 17), exhibit a constant, non-varying shift across the electrodes.

In Figure 18 F1s region, the measured shift is only 1.5 ± 0.1 eV, and corresponds to only half of the imposed potential, i.e. from the grounded reference value of the 688.5 [165] to 690.0 and 687.0 eV, under +3V and -3V bias, respectively. The intensity of F1s peak is non-uniform along the device. It represents a Greek vase structure as a result of IL impregnation in PEM from the middle of the device, but the peak position is uniform, which is totally different from those of the Au4f peak. Thus, only half of the imposed potential prevails on the IL surface, and the rest are partitioned equally to the two metal electrode-IL interfaces, as depicted in Scheme 3. The data presented in Figure 18 and simulated in Scheme 3, related with formation of two similar but oppositely polarized EDLs at both electrodes, and the voltage drop at the metal electrode-IL medium interfaces, are new and direct experimental demonstration of the earlier theoretical prediction.[56]

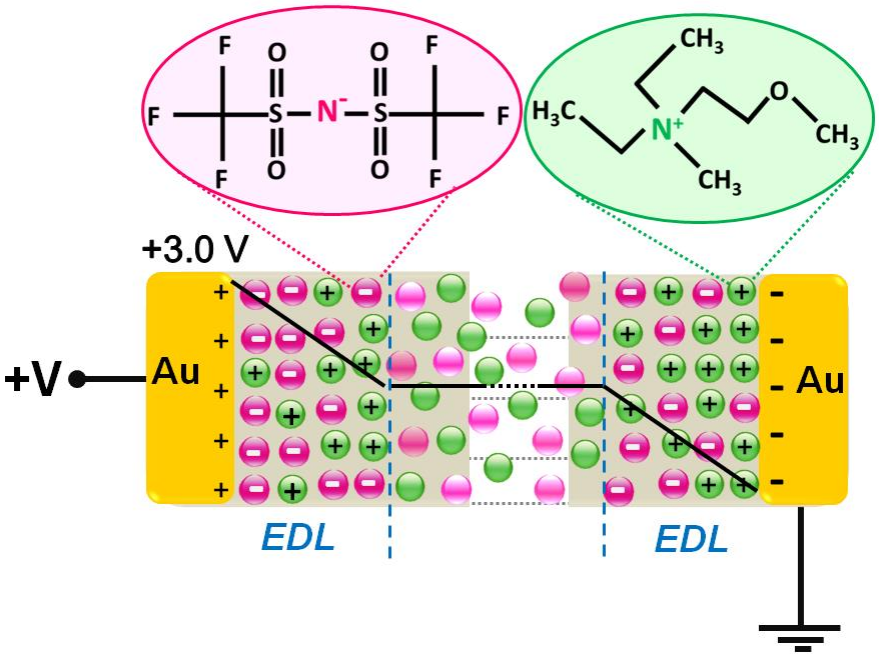

Scheme 3. Schematic representation of ionic fragments across IL-device under applied +3 V potential and charge screening at two interfaces by EDL formation. "Reproduced by permission of the PCCP Owner Societies. http://pubs.rsc.org/en/content/articlelanding/2016/cp/c6cp04933h#!divAbstract "

3.2.2. XPS Analysis Under A.C. Bias

IL-electrochemical device with two Au-electrodes at the each end and conducting IL medium in between enables the study of charge screening and dynamics in both temporal and lateral resolution:

i. *Temporal resolution* is attained through recording the response of surface potential under the application of time-varying external electrical stimuli in the form of slow square waves (SQW).

ii. *Lateral resolution* is achieved by the XP spectra throughout the different lateral position along the entire electrochemical device.

Applying a time-varying electrical signal in the form of slow square-waves (SQW) with a frequency of 10 mHz and amplitude of 5V allows us detect temporal response of the surface potential by recording the F1s signal (or any other peak) with 1s time-resolution, as shown in Figure 20, and also as a function of the lateral position of the probed region from the electrodes, i.e. with lateral resolution as well.

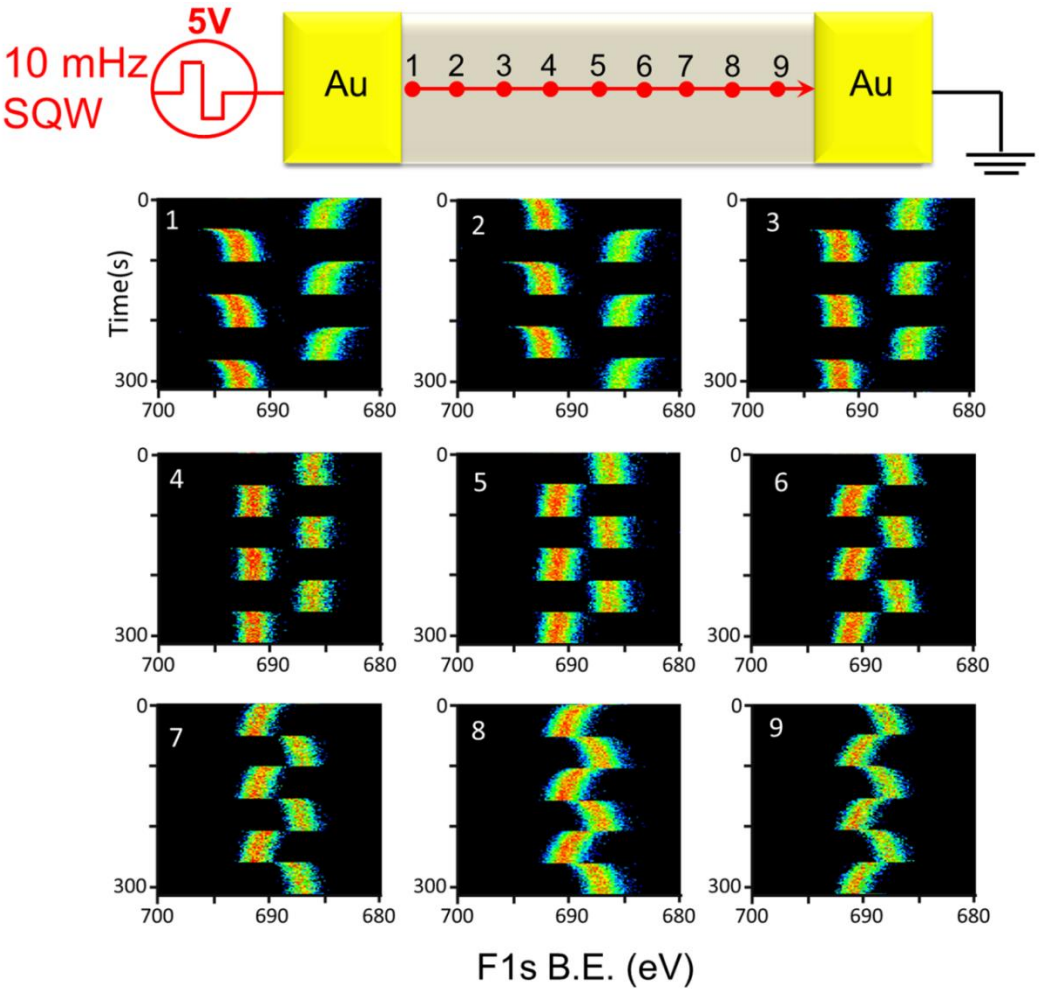

Figure 20. Time-resolved F1s XP spectra recorded at nine different lateral positions across the metal electrodes with 800 μm step-size between each point. Reproduced by permission of the PCCP Owner Societies. http://pubs.rsc.org/en/content/articlelanding/2016/cp/c6cp04933h#!divAbstract ”

The two electrode device, with a conducting IL medium in-between them, provides a platform to study charge screening and dynamics both in moderate time- and position-resolved fashion. When we apply a voltage bias between the electrodes, the mobile ions of the IL screen the local voltage varies along the channel length, such that it acts in opposite directions at the two electrodes, as depicted in Scheme 3. Moreover, this scheme predicts the presence of a hypothetical point of no motion (in time) near midpoint of the electrodes, which is also verified experimentally, and is shown in Figure 20.

In Figure 21, the data presented in the latter figure at positions 1, 4 and 9 respectively, are reproduced parts of as well as limiting the F1s spectra to the first 1-100 s time-window. When the positive cycle of the 10 mHz SQW excitation is switched on, the F1s peak shifts to 688.5 + 5.0 = 693.5 eV, upon which the IL starts screening this potential and reduces it down to 691.0 eV, the equilibrium potential (+2.5V) of the IL medium under +5V electrification. This is exactly what is measured in regions near the electrode as shown in Figure 21 (a). As can also be gathered from the same figure, in the negative cycle (i.e. 50 s later) the peak starts at 688.5 – 5.0 = 683.5 eV and moves towards 686.0 eV. However, the regions near the ground electrode behave in the opposite direction, since at the beginning, the interface was negatively charged, hence a symmetric but opposite screening is observed as a function of time as shown in Figure 21 (c). The middle point does not experience any screening; hence no time dependence in the position of the F1s signal is observed [Figure 21 (b)]. Data presented in Figures 20 and 21 on the laterally resolved information, retrieved from the chemically addressed XPS F1s signal, brings also a new and equally important finding, where it is shown that the device is partitioned to cathodically and anodically polarized

regions and they meet at a neutral point in the middle. The frequency used in Figure 21 is 10 mHz which is not long enough for the response to reach the steady state value the F1s peaks are switched before reaching their D.C. values.

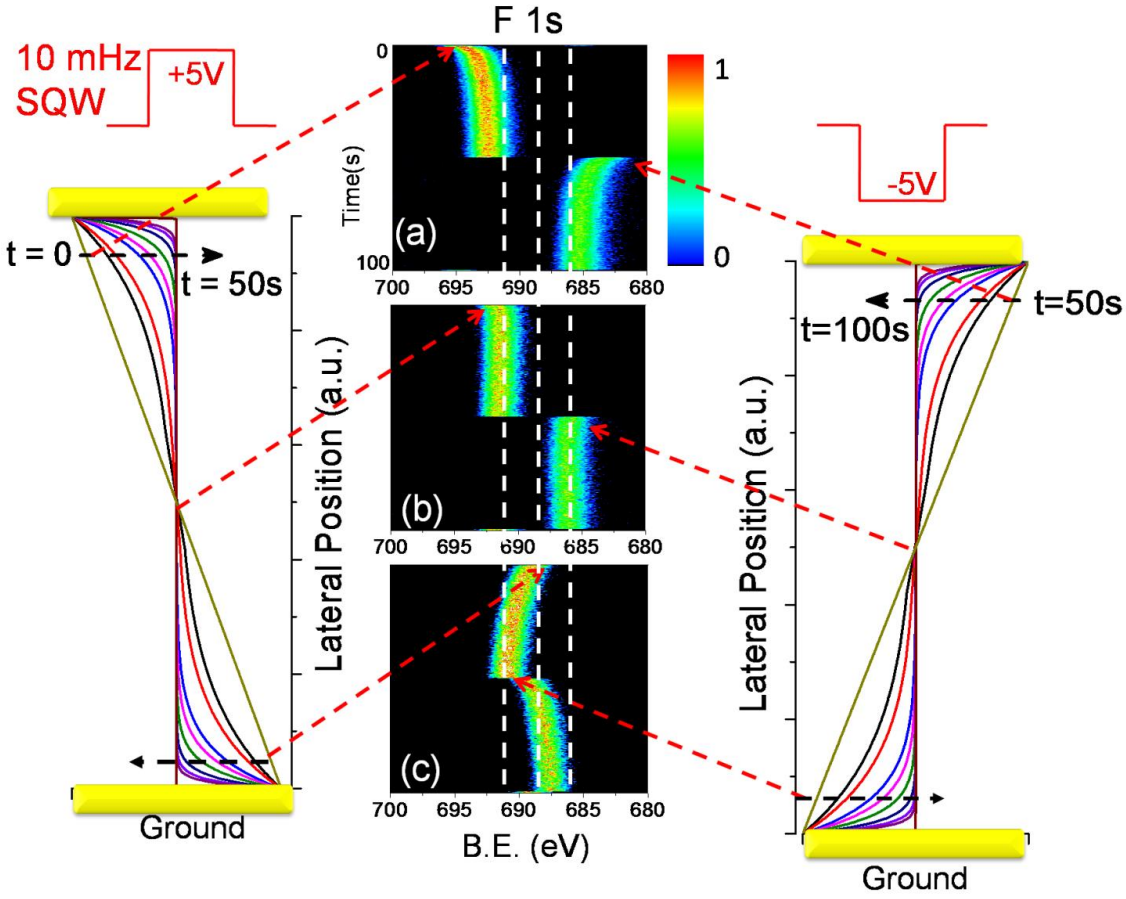

Figure 21. Time-resolved XP spectra of F1s region under 10 mHz 5V SQW excitation and recorded at three different lateral positions, corresponding (a) point1, (b) point 4 and (c) point 9 in Figure 20. Schematic representation of potential changes along the channel for positive (left) and negative (right) cycles. "Reproduced by permission of the PCCP Owner Societies. http://pubs.rsc.org/en/content/articlelanding/2016/cp/c6cp04933h#!divAbstract "

However, the most significant finding of our work is related with the fact that the effects of the charge screening by the mobile ionic components is translated to unexpectedly long lateral range of millimeters, reminiscent of soliton waves.[166]

By varying the frequency of the SQW pulses, it is possible to tap into different electrical properties of the medium. For example, application of a higher frequency (e.g. 1 kHz) allows us catch the initial state of the electrification, since the ion motion is frozen in the timescale of this experiment, no screening is effective and the applied voltage variations along the channel between the electrodes faithfully follow the simple resistive strip model [164], as depicted in Figure 22. Accordingly, the 1kHz SQW measurements correspond to zero-time onset, and the D.C. measurements correspond to the other extreme of the infinite time.

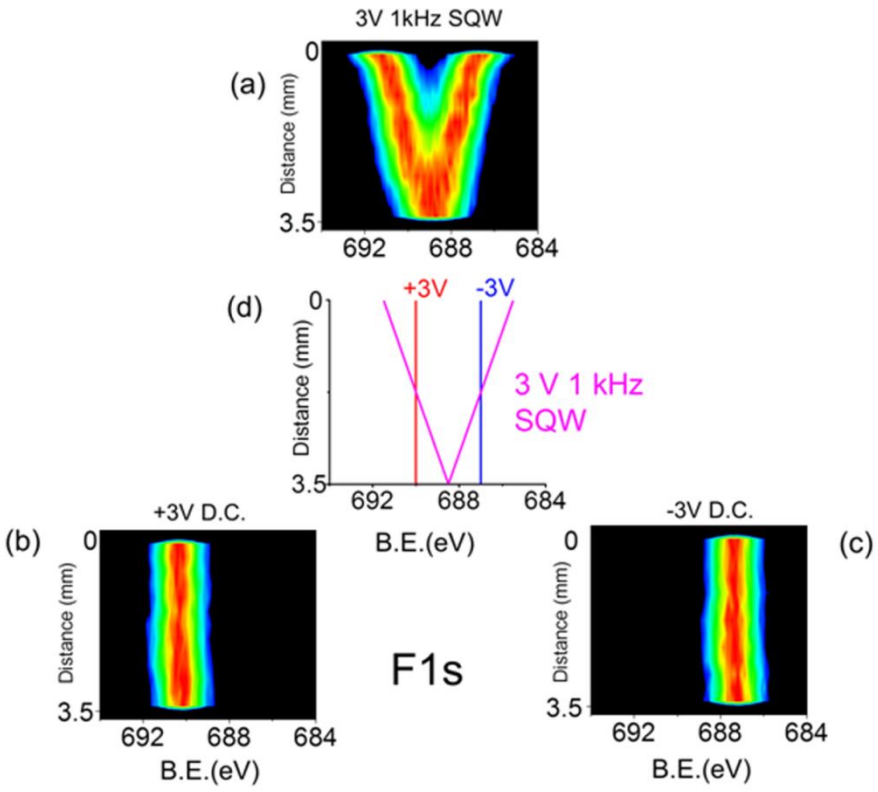

Figure 22. F1s region recorded in line scan mode across two Au electrodes under under application of (a) 1 kHz SQW with amplitude of 3V (b) +3V D.C. and (c) -3V D.C. Similar data acquired. (d) Simulation of F1s binding energy positions under corresponding electrical stimulus. "Reproduced by permission of the PCCP OwnerSocieties.http://pubs.rsc.org/en/content/articlelanding/2016/cp/c6cp04933h#!divAbstract "

3.2.3. Current Measurements and Equivalent Circuit Model

Imposing a voltage stimulus induces an exponentially decaying current with time constants in tens of seconds as given Figure 23. In prolonged times (>1000 s) this current reaches a steady-state value of ~10 nA (not shown), which could be thought of as a leaky capacitor where the main leakage mechanism is expected to be oxidation and reduction taking place on the gold surface of the electrodes. The prolonged application of +3 V bias leads to formation of Au-nanoparticles in the vicinity of the polarized electrode but within the ionic liquid medium, which will be discussed in Section 3.4.

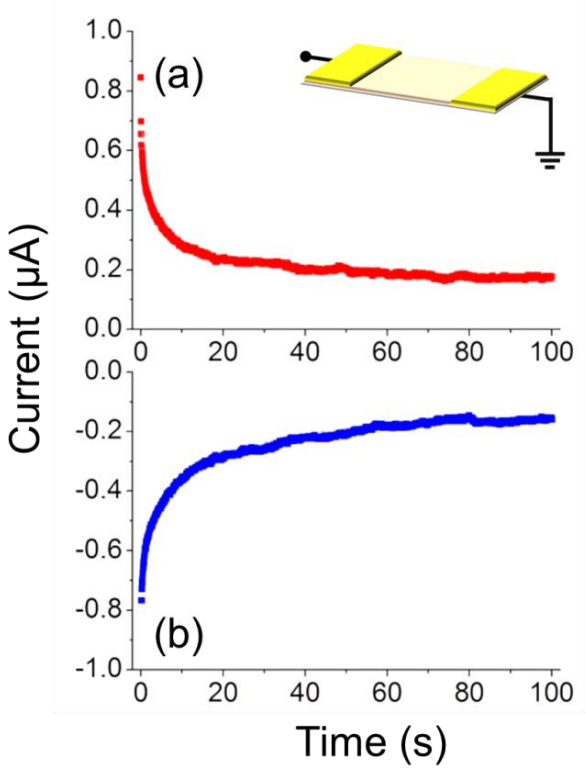

Figure 23. Measurement of current with respect to time for (a) +3V to 0V and (b) -3V to 0V potential application.

The observed voltage dependence, on the lateral position of the ionic liquid across the electrodes, can be modeled with a simple network of resistors and two capacitors, as shown in Figure 24. The capacitors at either side are modeling the electrochemical double layer on the metal-IL interface, and the resistor in the middle is modeling the IL infused polyethylene. To take into account of the persistent ~10 nA current which, two resistors was also included, representing the unavoidable oxidation-reduction taking place on the gold electrodes, as the proposed leakage mechanism across the double layer capacitance. Yet another geometry where the large parallel resistor was placed across the two gold electrodes to represent a current leakage yields a very similar picture.

As can be seen from Figure 24, switching the +5V pulse causes an upward jump, consequently an increase in the binding energy of the measured F1s, when monitored near the biased electrode (designated as Position 1 in Figure 20). Subsequent screening by the IL causes a decrease in time and brings it to near equilibrium position of +2.5 eV. In the negative cycle a reverse behavior is observed. When the corresponding behavior is monitored in a point near the grounded electrode (Position 9 in Figure 20), an opposite picture arises. Before switching the +5V cycle of the pulse, this point was at -2.5 V, the equilibrium potential under -5V, and with the +5V pulse, and together with the screening action of the IL, its position starts moving towards positive directions, and descends to the near equilibrium position of +2.5V. This simple simulation overlooks the fine details of charging at the interface and the ionic liquid surface but provides a basic understanding of the underlying polarization.

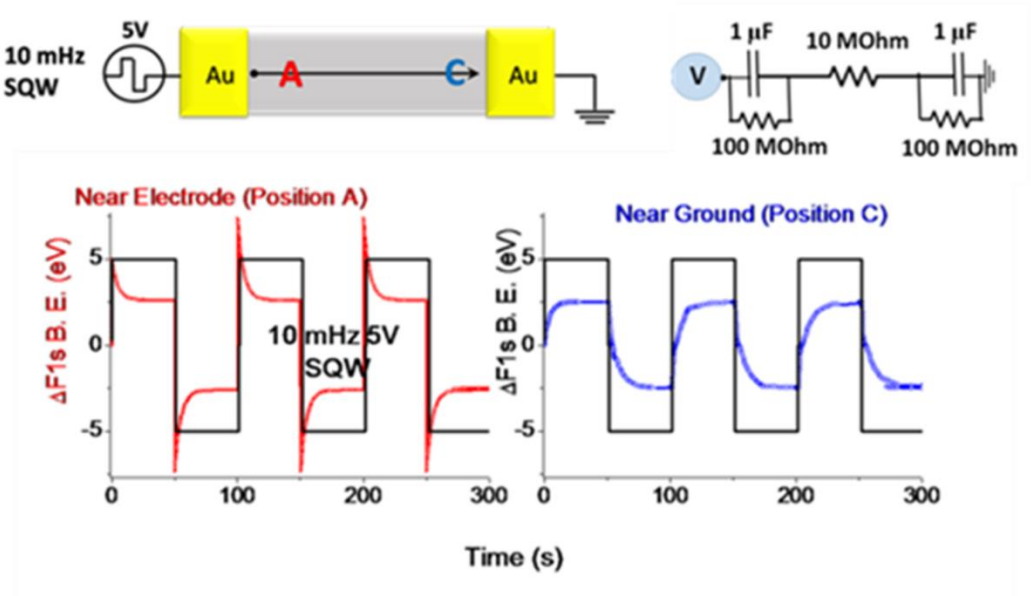

Figure 24. Simulations of potential developed at near electrode region and near ground region under 5V 10 mHz SQW. Equivalent circuit model represents the resistors and capacitors. "Reproduced by permission of the PCCP Owner Societies.http://pubs.rsc.org/en/content/articlelanding/2016/cp/c6cp04933h#!divAbstract "

3.3. XPS Study of Structural Rearrangements in DEME-TFSI at Au Electrode / IL Interface

The structural rearrangement of the ionic fragments closer to the interfacial region is a complicated subject with plenty of room for enhancing our basic understanding. Hence, investigations on probing the preferential rearrangements of the anions and cations are of ultimate interest for further developments in fundamental understanding as well as towards their applications. The most crucial informations are the electroneutrality breakdown and/or kinetics of restructuring of the ion-pairs of the ILs at the electrified interface. In addition to the electrochemical characterization technique; [72] sum-frequency generation (SFG), [150, 151] infrared, [68, 71] Raman, [167] and NMR spectroscopic, [168, 169] surface plasmon resonance, [72] and X-ray reflectivity, [54, 170-173] and AFM,[61] measurements have been utilized to characterize the chemical nature of the changes taking place at the electrochemical interfaces. The common findings of these experimental investigations are the existence of an unexpectedly slow response of ions (10^{-1}-10^{2} s) together with a hysteresis behavior, both of which have been confirmed by extensive simulation studies.[74, 77, 150, 153, 154, 174]

XPS is a chemical state resolved technique, so photoelectron peaks of charged fragments can be distinguished and followed by the intensity changes upon the polarity change thru applying external potential to the sample. For positive or negative bias application, local charge builds up at the interface between electrode and electrolyte and the mobile ions in IL undergo a structural rearrangement. However, until now all XPS measurements have been carried out without deliberate electrification of surfaces. [136, 175] Since it is anticipated that a slow rearrangement of ions will take place at the interface, an equally

slowly varying electrical signal can be used to induce rearrangements, yet allow recording of XPS data in transient. XPS measurements have ability to provide structural information in addition to electrical information about the sample by recording the data under application of external electrical stimuli. In this section it will be shown below that electrical excitation causes charge imbalance between the ion-pairs, revealed by intensity changes of the N1s peaks of the anion and the cation.

DEME-TFSI has well resolved two nitrogen atoms one with a positive $-N^{+}$ group (quaternized ammonium) and the other with a negative $-N^{-}$ group (imide) representative of the DEME-cation and the TFSI-anion. For this purpose, two symmetrical Au electrodes are deposited on PEM, and the DEME-TFSI is injected underneath the membrane in between the electrodes as represented in experimental section [Figure 8 (b)]. The impregnation of the device underneath and the diffusion of DEME-TFSI toward the surface through the pores of PEM enable the study of surface structures. The external electrical stimulus is imposed between the two gold electrodes, where one of them connected to the function generator and the other one grounded as described before in source-drain geometry and the XP spectra were acquired under external potential from the interfacial region near source-electrode (Figure 25).

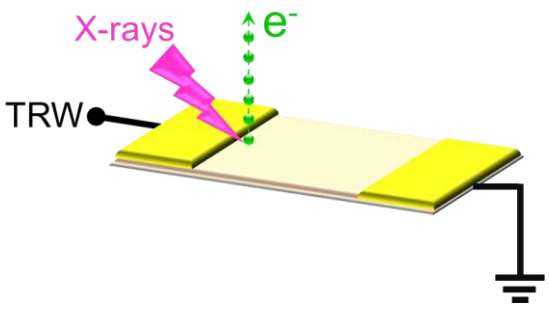

Figure 25. Schematic illustration of (a) preparation and impregnation of device (b) XPS analysis in source and drain geometry.

The typical XP survey spectrum in Figure 26, confirms the presence and the stoichiometry of the IL with the peaks of C1s, N1s, O1s, F1s, and S2p. The well-resolved N1s peaks represents the anionic $–N^-$ and the cationic $–N^+$ fragments in DEME cation and TFSI anion structures with the corresponding binding energies of 402.7 and 399.5 eV, respectively. The anionic $–N^-$ will be termed as N1sA and the cationic $–N^+$ as N1sB in the following discussions in this section. Theoretically, the ratio of N1sA/N1sB =1 due to the 1:1 ratio of two distinct nitrogen species. Before application of the electrical bias, the intensities of these two peaks are very close to each other with a measured intensity ratio of 1.00 ± 0.05 as shown in Figure 26-inset.

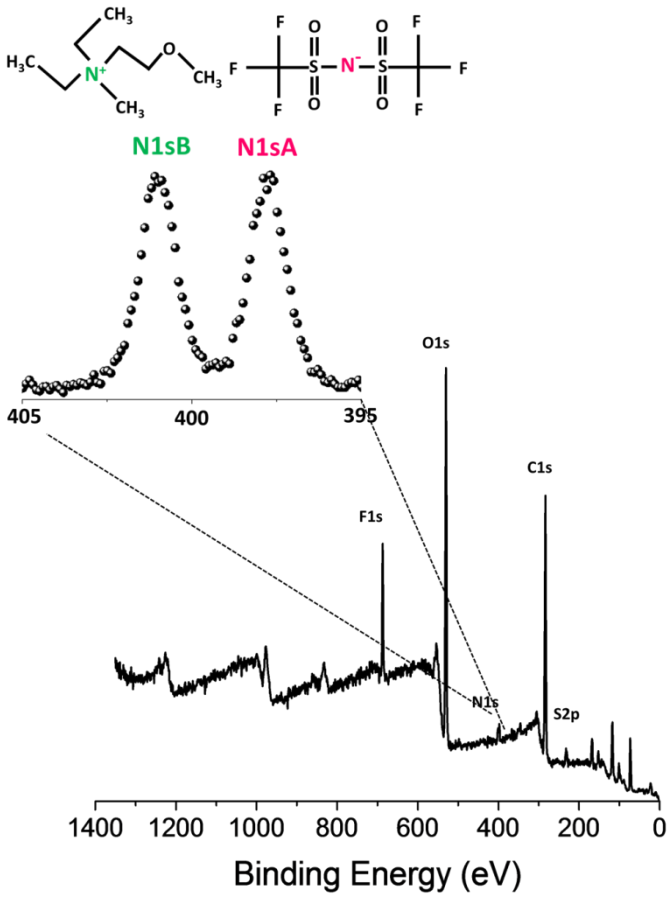

Figure 26. Survey XP spectrum of the Ionic Liquid DEME-TEFSI molecular structure and the corresponding N1s region inlet.

High ionic conduction in ILs causes the movement of ions that is different than the electronic conduction based on the movement of electron. The structural rearrangements of the mobile IL-ions might be probed by the time varying external electrical stimuli in the time scale of the motion of these mobile ionic fragments in the order of tens to hundreds of seconds. Therefore, a triangular wave excitation was adopted, with a 5 V amplitude and 1 mHz frequency, which were optimized to provide the information sought-after, which is the intensity variations of the cationic to anionic peaks as a function of the polarity and the degree of the electrification. It is very important to note that, a time varying stimuli is absolutely necessary to induce ion motion, which is in the order of several tens of seconds, on the other hand, recording a reliable spectral region also requires a finite time window.

The spectrum of the N1s region (390 - 410 eV) is recorded in two different scans as a practical solution to this dilemma since during data acquisition the extent of the electrification also changes. In the first round, the spectrum is recorded in order of increasing binding energy of 0.2 eV steps with a dwell time of 100 ms, and in the second round the same region is recorded in order of decreasing binding energy, resulting in a time difference of 10 seconds between the two N1s spectra, as represented in Figure 27. Under the application of external bias in TRW form external potential is scanned linearly and the N1s peak positions also change, which can be used to reflect the sign and the magnitude of the electrification. The ratio of the anionic $–N^-$ and the cationic $–N^+$ fragments in IL structure is expected to follow the rearrangement of the anionic and cationic fragments with respect to the developed charge at the IL/electrode interface.

Figure 27 displays two different spectral evolution in time, together with their time sequences depicted schematically.

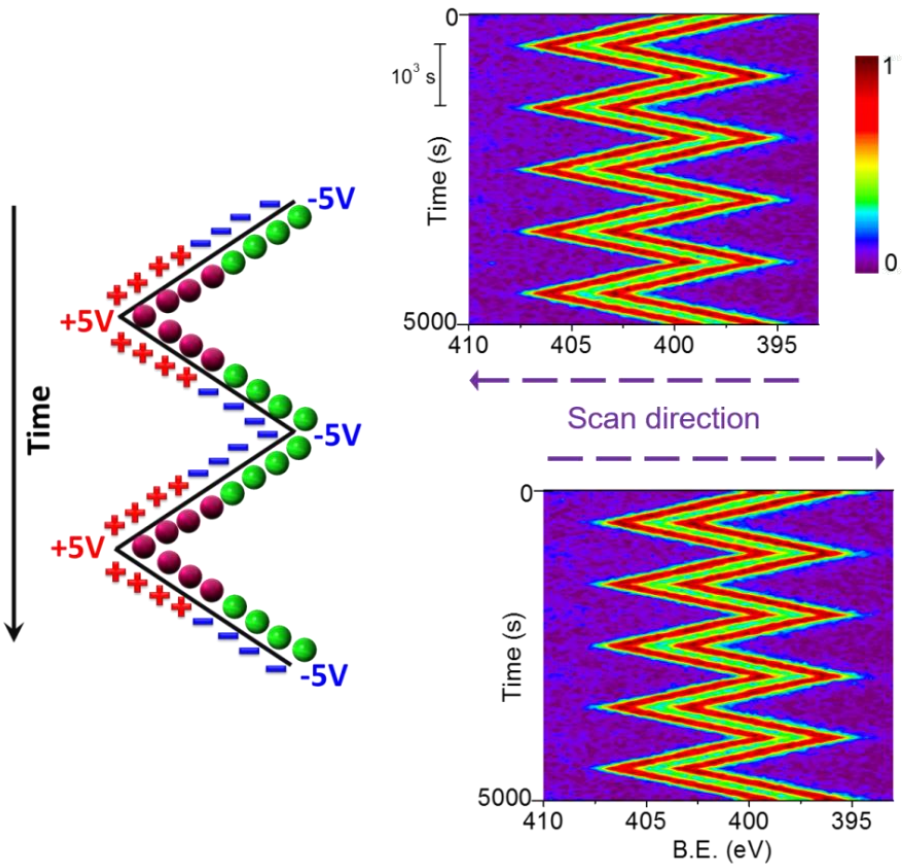

Figure 27. Time-resolved N1s spectral region while the recorded in the forward and reverse directions, while a 5 V TRW excitation is imposed from one of the metal electrodes. The responses of cationic (pink) and anionic (green) fragments to imposed potential change are illustrated.

Each spectrum is fitted to two N1s peaks corresponding to anionic $–N^-$ and the cationic $–N^+$ fragments and the binding energy positions, areas and also the intensity ratio of them are computed separately. The analysis shows that the charge fragments within the IL structure undergoes an interstructural rearrangement with respect to the developed charged at the IL/Au electrode

interface and this is revealed by the intensity change in the well resolved N^-/N^+ photoelectron peaks as shown in Figure 28. It is more obvious to follow the fluctuation in the average of N^-/N^+ intensity ratio up to ~20% intensity increase while the potential is scanned slowly from -5V to +5V in 1000 seconds allowing enough time for the anionic and cationic fragments to re-orient themselves. This intensity fluctuation is reversible and reproducible for longer experiment times, typically 5-6 hours.

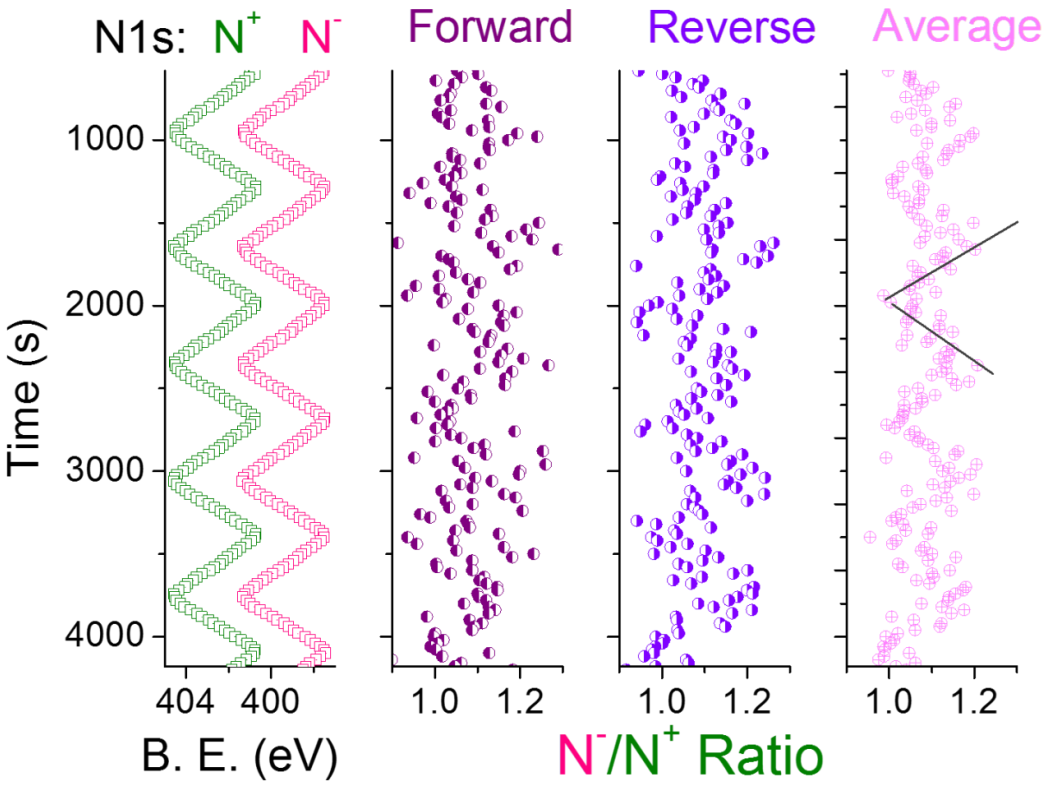

Figure 28. Extracted B.E. positions of the two N1s peaks, together with computed intensity ratio of them, while a 5 V TRW excitation is imposed from one of the metal electrodes.

In order to check the consistency of intensity change in N1s peaks and to minimize the random intensity variations across the electrodes; the Au4f peaks of the electrode and N1s regions are compared with each other. Au4f and N1s regions are recorded under the same experimental conditions. Data in Figure 29 are evaluated by summation of three regions where each one corresponds to one TRW cycle. Au4f region has two peaks due to the spin orbit splitting. As it can be gathered from Figure 29, the measured ratio of the $Au4f_{7/2}$ peak intensity to the intensity $Au4f_{5/2}$ is constant ($Au4f_{7/2}$ /$Au4f_{5/2}$≅1.4). $Au4f_{7/2}$/ $Au4f_{5/2}$ is found to be independent of change in the peak positions as a result of TRW electrification. In contrast, N1s A/ N1s B intensity ratio changes in the same direction of N1s peak position change as shown in Figure 29. The black square-graph is the binding energy change with respect to the applied TRW pulses that follow one cycle from +5V to -5V. Since Au4f XP spectra are acquired from the reference Au-metal, the amplitude of applied potential [10.0 V = +5.0 V – (-5.0 V)] is directly observed in the binding energy shift. However, N1s peak of DEME-TFSI medium has only a response of ~5.0 eV shift in its position, that is the half of the imposed potential difference, in binding energy consistent with the findings discussed in Section 3.2. The ratio between $Au4f_{7/2}$/ $Au4f_{5/2}$ is found as 1.4 ± 0.05 since the ratio of these two spin orbit doublet peaks are fixed. The experimental graph is consistent with the theoretical prospects. The intensity change in N1sA and N1sB peaks is once more underlined to be ~20%.

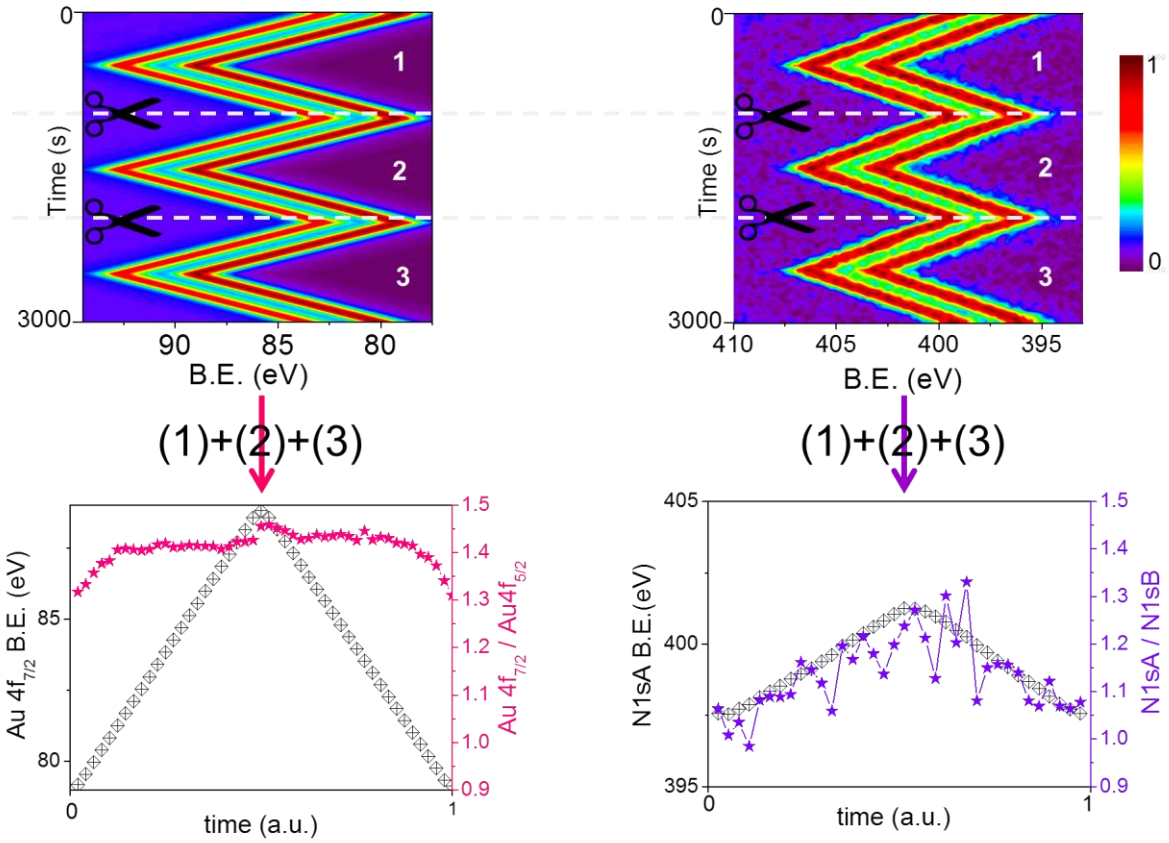

Figure 29. Time-resolved Au4f and N1s spectral regions while the recorded in the forward direction while a 5 V TRW excitation is imposed from one of the metal electrodes and extracted B.E. positions of the $Au4f_{7/2}$ and N1sA peaks, together with computed intensity ratio.

Although the binding energy position is varied by the exposed TRW potential, the intensity ratio between two peaks for Au 4f region is expected to be almost linear since the peak area of the doublets corresponding to Au-metal is almost non-responsive to the external electrical stimuli. The ratio between two N1s peaks changes as a function of applied potential since anions and cations undergo rearrangement. In addition, the residual sum of squares describes the overall deviations of the actual data from the predicted model (data fluctuations from the linear regression line in our case) so a graph of peak intensity ratio vs.

binding energy (Figure 30) shows deviations for Au4f and N1s region. The residual sum of squares value is found to be higher for N1sA/N1sB compared to the $Au4f_{7/2}$/$Au4f_{5/2}$ and the slope of N1s peaks is higher with larger standard deviation as compared to the nearly linear graph of Au peaks, which support our findings.

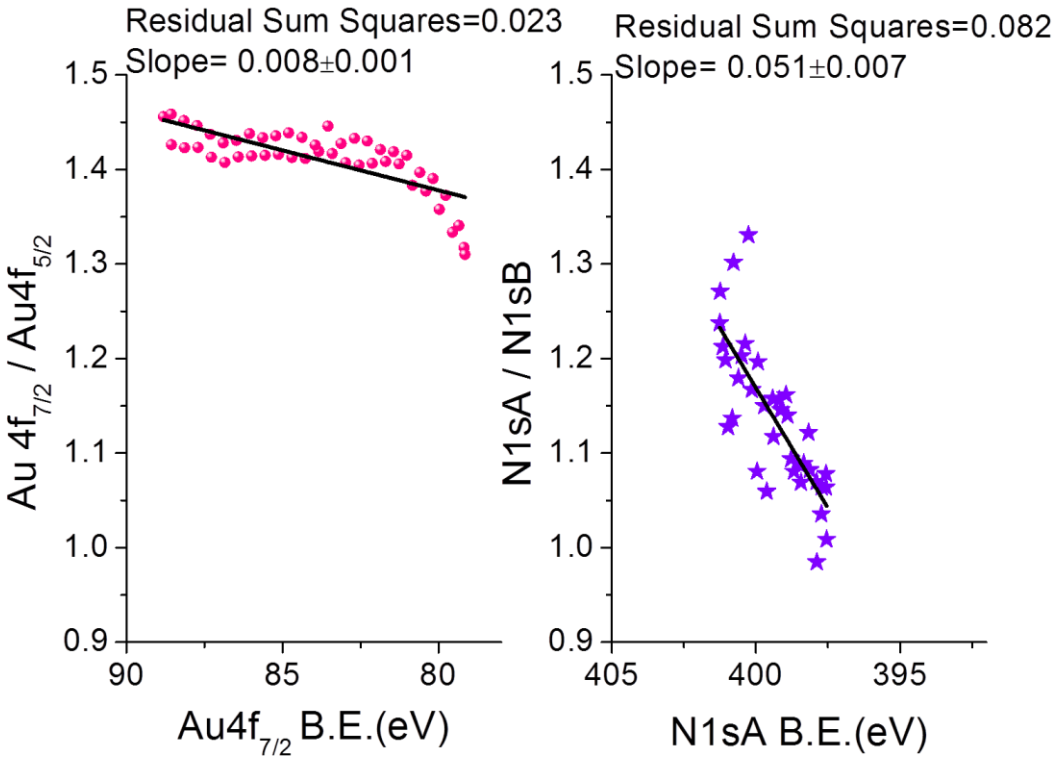

Figure 30. Evaluated data for Au4f and N1s spectral regions representing the residual sum of squares and slopes together with standard deviations.

3.4. *In-Situ* Electrochemical Reaction Monitoring by XPS

Since XPS is a chemically resolved spectroscopic technique, change in the electronic structure of the constituents so the chemical states and environments as a result of an electrochemical reaction, can be monitored *in-situ*. A study of an electrochemical system in real time requires insertion of the electrochemical cell into UHV together with externally connected potentiostat. But in our electrochemical device two Au electrodes plus DEME-TFSI IL medium in-between is closer to an arrangement of a typical coplanar capacitor geometry. This geometry appears to be also a suitable platform to study the *in-situ* and *in-vacuo* electrochemical reactions, as well as recording XP spectra. As described in details in Section 3.2, the prolonged application of +3 V bias leads to formation of Au-nanoparticles (i.e. oxidation mediated electro-corrosion). Therefore in this section, three important questions are focused to answer;

i. Is the reaction predominantly electrochemically driven; if so anodically or cathodically triggered?
ii. Are the Au NPs neutral or charged?
iii. Where do the NPs reside; within the IL medium or deposited on the metal electrodes?

3.4.1. *In-situ* Electro-corrosion Monitoring

The experimental arrangement as described in previous sections, where two Au electrodes are fabricated, in the source-drain geometry, and on a porous poly-ethylene (PE) membrane containing the impregnated IL as the medium providing electrical conductivity, is used. This device geometry is also suitable for real time reaction monitoring at the electrodes. However, this time we have carried out our XPS measurements in much longer time scales of up to several days. +3V D.C. stress has applied while recording consecutive XP spectra in the line scan mode as snapshots of the Au4f region, with 100 μm X-ray spot- and 100 μm step-sizes, respectively, between each data point starting from the source electrode to the drain as shown in Figure 31. The experiment has continued for 15 hours continuously. Figure 31 represent four Au4f regions in time-resolved manner, where x-axes in all spectra correspond to the binding energy in eV and y-axes correspond to distance in millimeters from the source towards drain recorded at the beginning, after three and half, six and fourteen hours, respectively and electro-corrosion process is monitored. The Au4f photoelectron peak appears at 84.0 eV at the grounded electrode and is shifted by 3 eV to higher binding energy at the polarized electrode. As the color bar represents the intensity of Au4f peak, the intensity of Au4f peak corresponding to source-electrode decreases, but there is no change at the drain side, within the time as represented in Figure 31 (a) to (d). The corrosion is noticeable through the physical changes in the electrode accompanied by formation of secondary Au-species at the electrode/IL interfacial region in the polarized electrode only, by examining the Au4f spectra recorded in the line scan mode across the entire device repetitively as the device has been subjected to external biasing up to 14 hours continuously. In parallel, secondary

Au-species ascending from the source side as tails with low intensity, which will be discussed in Section 3.4.2. The decrease in the intensity of source- electrode and the secondary Au species becomes more apparent in prolonged analysis time up to 14 hours.

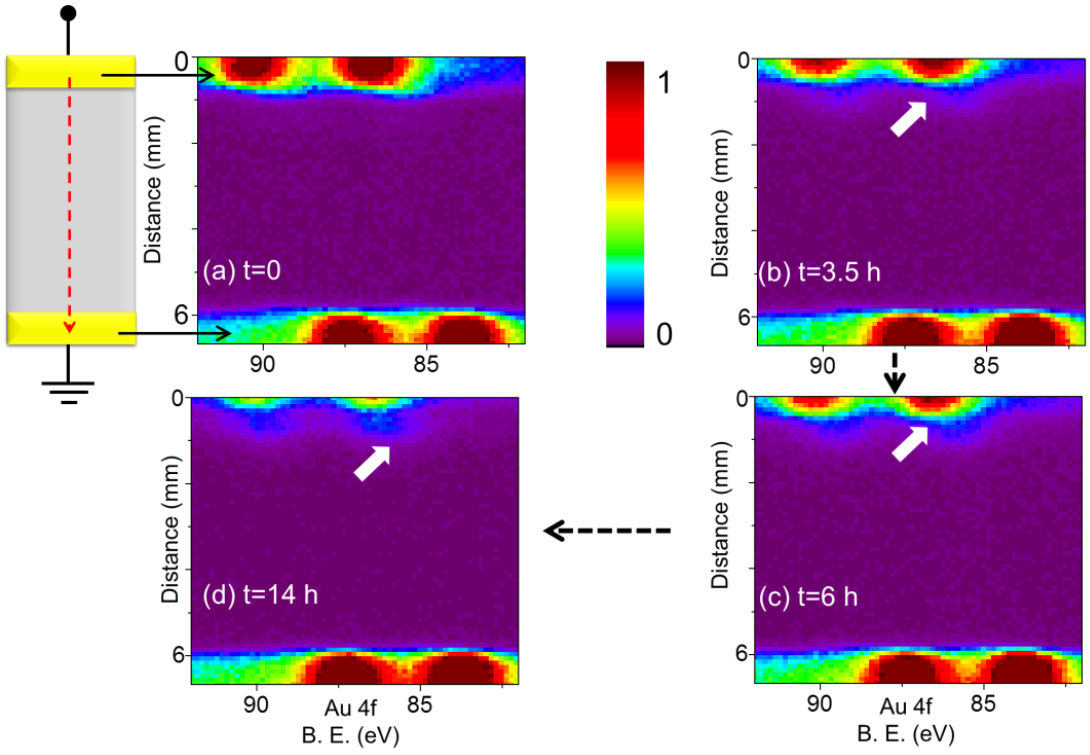

Figure 31. XP spectrum of Au4f region, recorded in the line scan mode from source towards drain electrodes;(a)at the beginning of the experiment (t=0), after (b)3.5 hours (t=3.5 h),(c) 6 hours (t=6 h) and (d)14 hours (t=14 h) during the continuous application of +3V D.C. external potential. Schematic illustration represents the line scan direction and the source - drain geometry including the electrical connections.

A current flows from electrode toward to the electrolyte as a result of positive polarization of the electrode, which is known as *anodic polarization*, and the electrode corrodes due to the electrochemical oxidation reaction (anodic reaction). In our device geometry, +3V potential exposure results in current flow at a high level but it decays to a steady state value of ~14 nA, that triggers the corrosion of the source-electrode. In Figure 32 (a) and (b) line scans along the entire device at the beginning and after 14 hours represented respectively once more to highlight the electro-corrosion process together with the comparison of Au4f spectra at certain points on source and drain electrodes. Au4f spectra are recorded under +3V D.C. potential application within time, at the position d = 0.5 mm corresponding to the 5^{th} point on the entire line scan (Figure 32). The corrosion at the source side under +3V D.C. potential, is emphasized by comparing intensity of the Au4f peaks. The spectra that are also normalized in intensity and shown in Figure 32 (a) confirm the corrosion of the polarized electrode by the significant decrease (~ 70 %) in the intensity of Au4f photoelectron peaks after 14 hours by application of the +3V D.C. However with the same approach, in the normalized spectra, recorded at the position d = 6.0 mm near the drain – side of the device [Figure 32 (d)], display almost no change as an indication of any electrode corrosion and/or secondary specie formation.

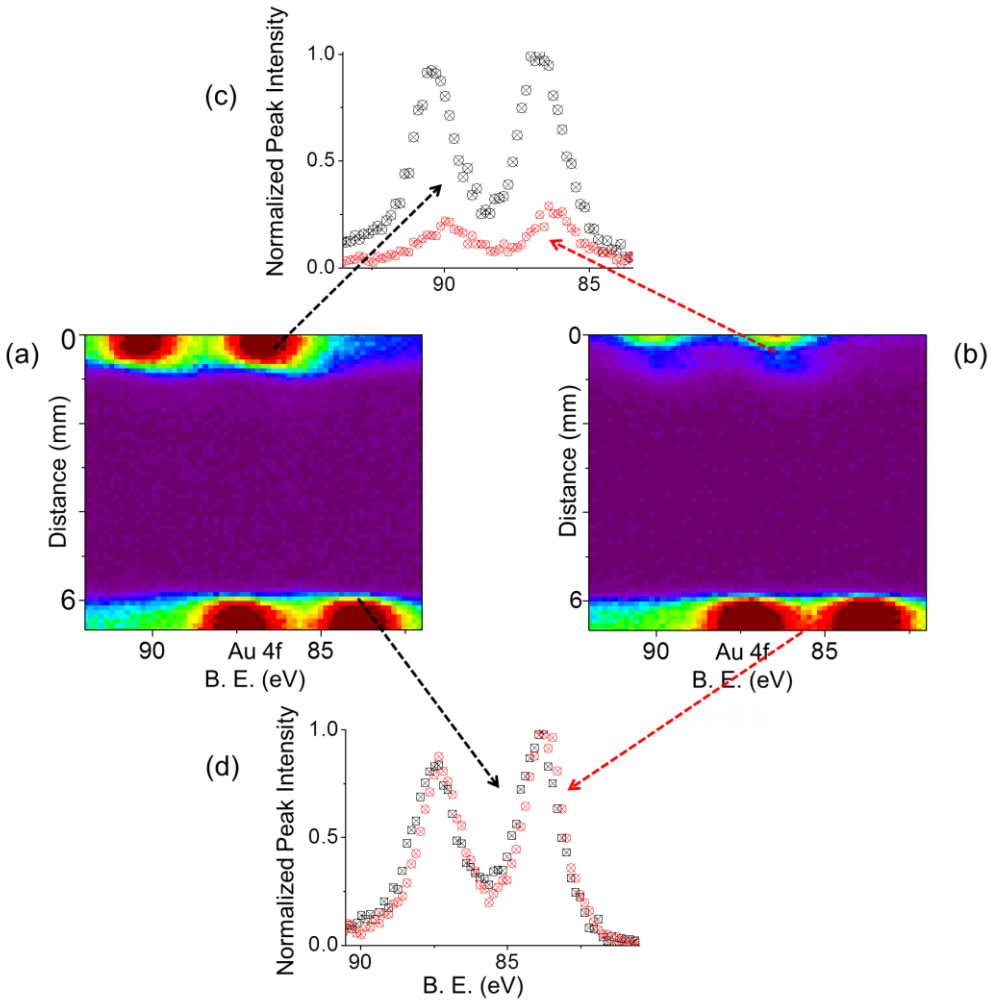

Figure 32. XP line spectrum recorded (a) at the beginning of experiment and (b) after 14 hours same in the Figure 31 (a) and (d). Normalized Au 4f spectra from the two points on the line at different positions are given in; (c) at 500 µm and (d) at 6000 µm away from the polarized electrode.

After probing the electro-corrosion under +3V D.C. potential and recording adequate number of line scans over the entire device, as a next step sign of the potential is switched to negative. Experiment is carried out under -3V D.C. potential using exactly the same experimental conditions except for the reversal of the polarization for 15 hours, continuously. At this point, the purpose is to observe whether an electrochemical reaction taking place at the *drain-electrode* upon the sign reversal of the imposed potential (*i.e. if there is also an electrochemical reaction taking place at the grounded-electrode upon reversal of the polarization.)* and the time-dependent results are depicted in Figure 33, from (a) to (d). Due to the imposed -3V D.C. potential, binding energy position of Au spin orbit doublet shifted to 3 eV lower position 81.0 and 84.7 eV at the source electrode, whereas still at grounded position of 84.0 and 87.7 eV at the drain electrode. The line spectra in Figure (a), (b), (c) and (d) for both the source and the drain sides display *no* apparent change in intensity neither at the source-side nor at the drain-side. In order to be convenient, two normalized Au4f spectra that are recorded from the position d = 6.0 mm on the drain-electrode at the beginning of the experiment and after 15 hours, are represented in Figure 33 (e) confirming that there is neither electro-corrosion nor secondary Au-specie formation at the drain-side of the device. Additionally, in parallel investigations, the stability of both the IL and the fabricated gold electrodes has been checked in vacuum and under X-ray exposure in the above-mentioned time scales, but without imposing any potential across the electrodes. As a result we can confidently say that no significant corrosion is observed under -3V D.C. potential. The experimental results for analysis under +3V and -3V D.C. potential, show that the electro-corrosion is definitely anodically triggered.

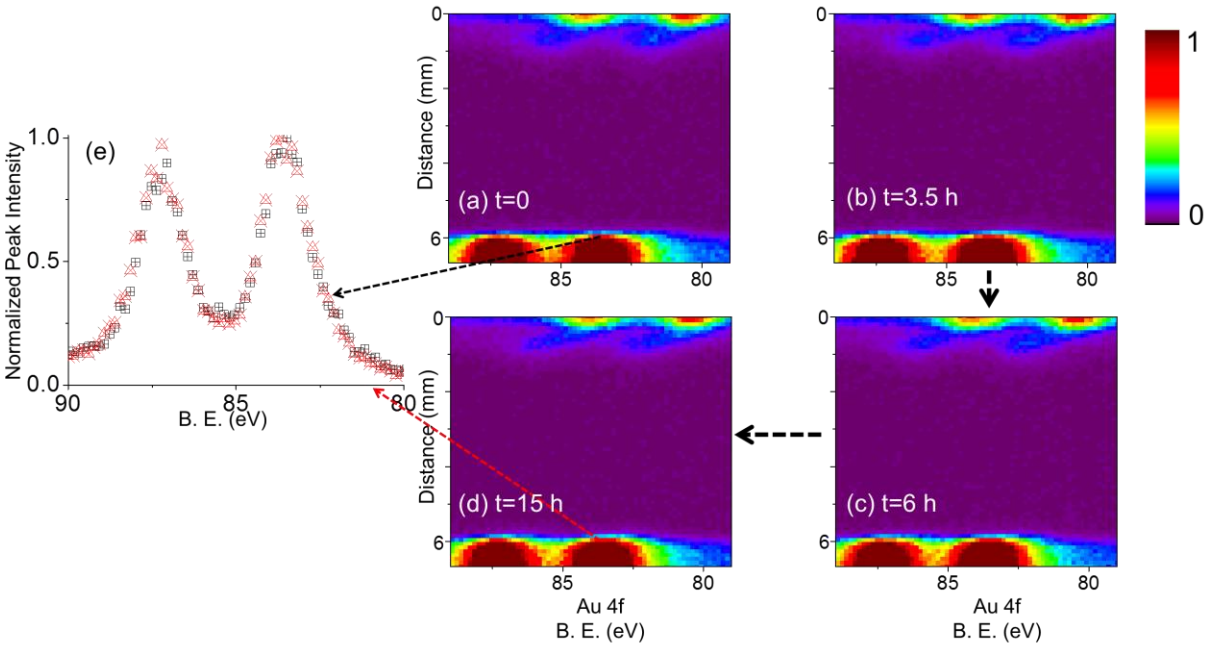

Figure 33. XP spectrum of Au4f region, recorded in the line scan mode from source towards drain electrodes;(a)at the beginning of the experiment (t=0), after (b)3.5 hours (t=3.5 h),(c) 6 hours (t=6 h) and (d)15 hours (t=15 h) during the continuous application of +3V D.C. external potential. (e) Au 4f spectra, normalized in intensity, acquired from the position d=6.0 mm at the beginning of -3V experiment (black) and after 15 hours (red).

3.4.2. Analysis of Secondary Au Species

The secondary specie formation has been detected after the application of +3V D.C. potential for 3.5 hours, as *tails* located at the source-electrode interface with DEME-TFSI [Figure 31 (b) to (d)]. In order to elaborate on the new Au species formed, we zoomed on the interface and recorded data using an X-ray spot size of 50 µm, and recorded a line scan Au4f spectra with 50 µm step sizes for about 1 mm while imposing +3, 0, and -3V D.C. bias, respectively. Figure 34 represents the corresponding line scans of Au4f region together with F1s region. While the secondary Au species appear as a *tail* of the electrode and their spectral positions cannot be separated from those of the metallic Au4f ones when the device is grounded, they get completely separated under both positive and

negative bias. Figure 34 (c) shows Au4f spectra that represent two different points on the line scan. The red spectra recorded on the metallic Au-electrode at 2nd position on the line scan and green spectra recorded on the newly-formed secondary Au species at 11th position in the line scan. The intensity of Au4f spin orbit doublet in Figure 34 (b) and (c) corresponding to secondary Au species is less than the both F1s and Au-metal electrode photoelectron peaks, remarkably. The spectral separation is related with the charging property of the surrounding medium of the new Au species, which, in actuality, is the IL medium itself.

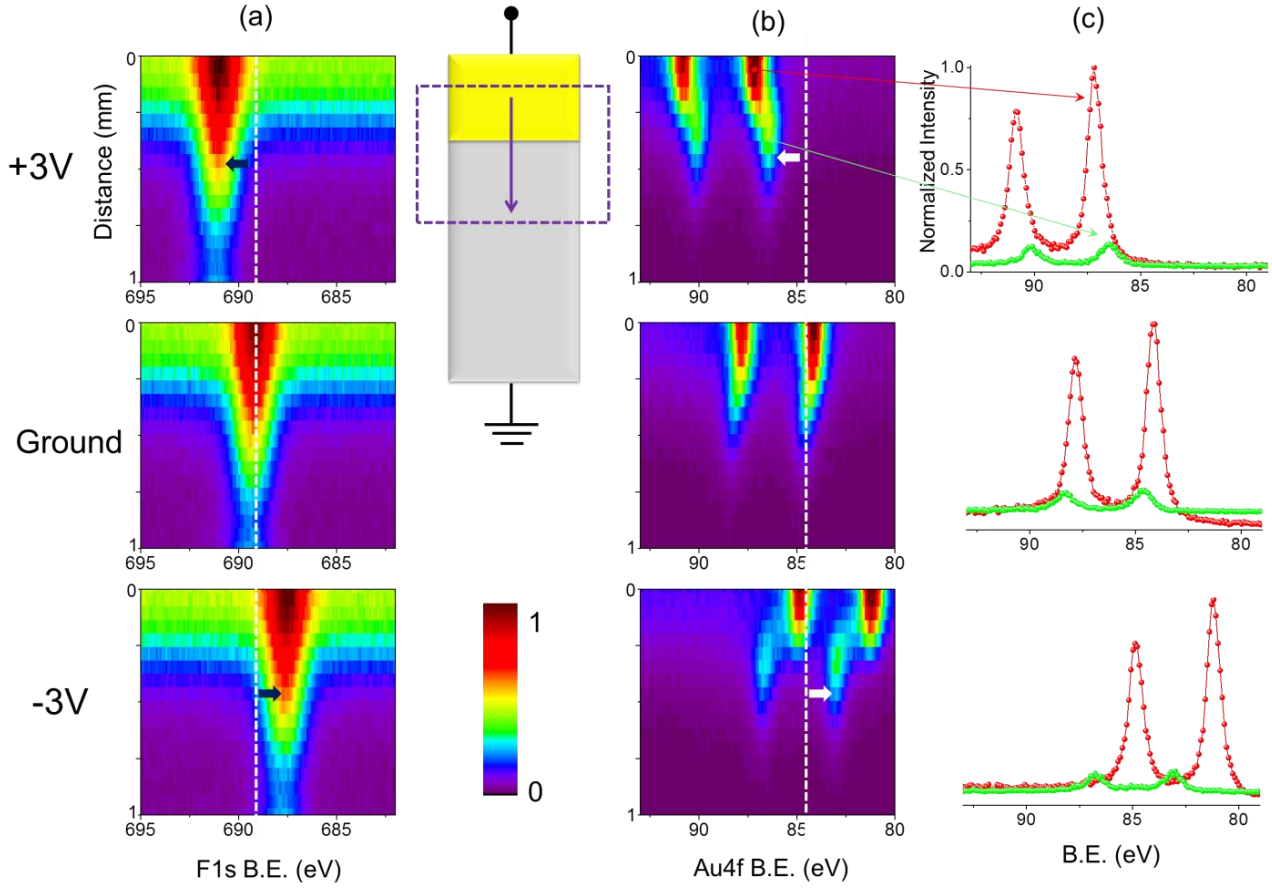

Figure 34. XP spectra of **(a)** F1s and **(b)** Au4f region in *line scan mode* along 1 mm from the source - electrode point recorded under application of +3V, 0V (grounded) and -3V D.C. potential. **(c)** Au4f XP spectra recorded in a higher resolution (*normal scan mode)* on Au electrode (red) and at interfacial region (green).

For that reason, the response of Au-metal electrode, the secondary Au species and the DEME-TFSI medium to the electrical stimuli are related to peak positions of Au4f and F1s peaks, respectively and measured binding energy values are represented in Table 2. The charging behavior of DEME-TFSI medium is reproduced (*See Section 3.2.1. for details*) by the symmetric voltage drop at the two Au-IL interfaces. Also the entire IL medium retains only half of the applied potential which is also uniform within the IL medium. Hence the F1s experiences approximately only +1.5 and -1.5 eV shifts from the grounded position when +3.0 and -3.0 V bias are applied.

Table 2. Measured binding energy values for Au4f and F1s peaks.

Position		B.E. (eV) +3V D.C.	B.E. (eV) Ground	B.E. (eV) -3V D.C.
2nd	$Au4f_{7/2}$(metal-electrode)	87. 14	84.14	81.16
	F1s	691.01	689.26	687.57
	Δ (F1s-$Au4f_{7/2}$)	603.9	605.1	606.4
11th	$Au4f_{7/2}$ (2° Au)	86.50	84.70	83.17
	F1s	691.02	689.17	687.62
	Δ (F1s-$Au4f_{7/2}$)	**604.5**	**604.5**	**604.4**

Spectral information in Figure 34 and the numerical results in Table 2, the metal electrode's Au4f peak has totally different but secondary Au species' Au4f peak has similar response with F1s peak. this is more or less the shift exhibited by the new Au species, and its uncharged binding energy can now be estimated using the binding energy differences between the F1s and the $Au4f_{7/2}$ peaks and working backwards to yield a value of (688.5 – 604.5) = 84.0 ± 0.1 eV, exactly the same value of neutral Au^0, hinting that the new Au species are neutral Au particles.

3.4.3. Role of Electrode's Nature in Electrochemical Au Nanoparticle Preparation

In order to obtain further information about the Au^0 particles and the role of electrode's nature in Au NPs preparation an electrochemical device in different arrangement has been investigated. Instead of the co-planar device geometry with two symmetrical Au electrodes, a bare Au-wire is immersed into DEME-TFSI IL liquid-electrolyte as source electrode and Pt-electrode is used as drain electrode (See Figure 9 in Section 2.3 and Figure 35) The device is transferred to vacuum XPS analysis chamber and exposed to continuous -3V D.C. for ~60 hours [Figure 35(a)]. In general, the formation of Au NPs can be followed through their well-known characteristic wine-red color beyond the analytical and/or microscopic characterization techniques. When the sample is unloaded from the spectrometer *no* apparent change or coloration are detected within IL, as depicted in Figure 35(c) and schematically described in Figure 35(a). In contrast, application of +3V [Figure 35 (b)] for the same duration (~60 hours) resulted in

formation of the well-known wine-colored Au NPs and a corresponding image of Au NPs are given in Figure 35 (d).

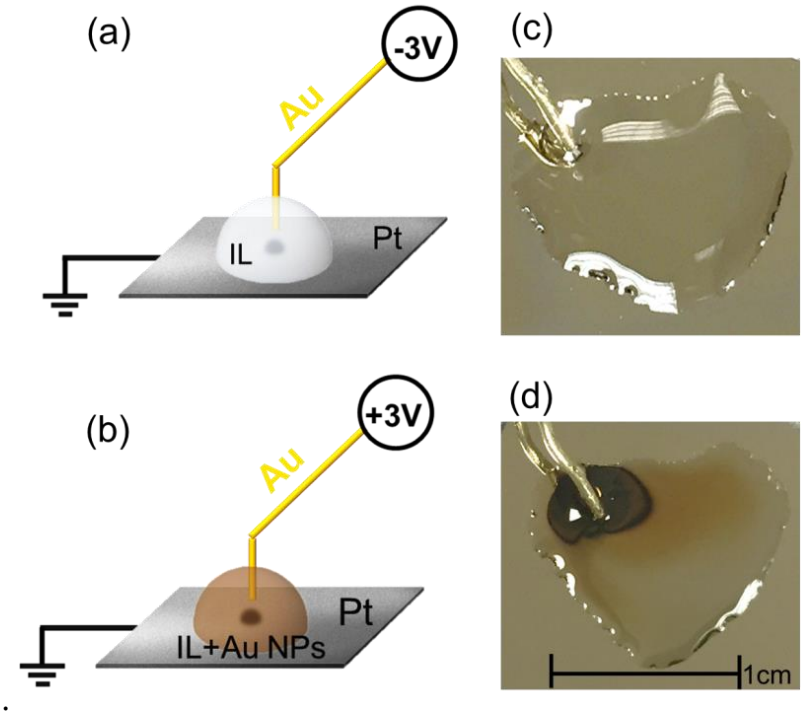

Figure 35. Schematic representation of experimental set-up corresponding (a) -3V (b) +3V potential application to Au-electrode. Images of the devices after ~60 hours under (c) -3V and (d) +3V external stress.

One step further verification of Au NPs in DEME-TFSI IL medium, is achieved by the SPR band appeared as a peak centered at 470 nm in the Visible spectrum (Figure 36).

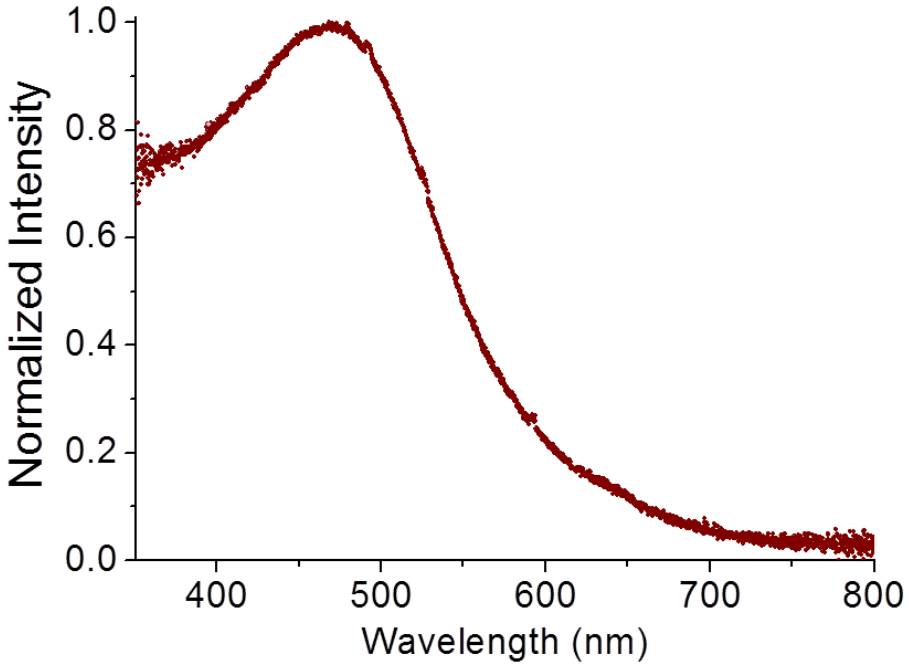

Figure 36. UV-visible spectrum of Au NPs in DEME-TFSI ionic liquid.

The quantification of the electrochemically prepared Au NP in IL-medium is estimated using the measured steady state current reached under +3V potential. During the +3V D.C. potential application to the Au-electrode for ~60 hours, 30 nA steady-state current is established. Since 1 A = 1 C/s, the steady state current appears to be $30 \times 10^{-9}\, A = 3 \times 10^{-10}\, \mathrm{C/s}$ and this current results in $\left(3 \times 10^{-10}\ \frac{C}{s}\right) \times (60\ h \times 3600\ \frac{s}{h}) \times 96485\ \frac{C}{mole} \cong 70 \times 10^{-9}$ mole electron flow for 60 hours, where $96485\ \frac{C}{mole}$ is the *Faraday constant*, that corresponds to amount of electric charge per mole of electrons. Also, assuming that the oxidized Au species have assumed +1 charge, the reduction process is a single step reaction that involves 1 mole of electrons ($Au^{1+} + e^{-} \rightarrow Au^{0}$) for each mole of produced Au^0 particles, and 70×10^{-9} moles of electrons correspond to ~70 n-mol electrochemically produced Au NPs. Thus, the concentration of Au NPs in ~10µl

DEME-TFSI medium is estimated as ~$10^{-3}M$ ($\frac{moles}{L}$). Using the Beer's Law $A = \epsilon.b.c$, as well as the extinction coefficient (ϵ) to be in order of 3-6x10^6/M.cm for small size-Au NPs,[176] and b is the thickness of the Au NPs-IL film ~10 μm; the calculated absorbance of ~1.0 A is consistent with the experimentally measured peak absorbance. Note that the literature absorbance values are given with respect to the concentration of Au atoms and not the concentration of NPs. The absorbance at 470 nm is the characteristics of spherical Au NPs dispersed in IL medium that are smaller than 5 nm[96] and TEM images in Figure 37, represented at different magnifications, verify the nearly spherical, small particle size around ~4 nm (smallest particle 3.4 nm of size and largest 7nm) of the Au NPs. Even at higher magnifications the lattice fringes of Au NPs are observable confirming the crystalline nature of gold. Au has Face Centered Cubic (FCC) crystal structure and the interplanar spacing *d*, that is the distance between to planes in a FCC crystallographic structure, is calculated by $d_{hkl} = \frac{a}{\sqrt{h+k+l}}$ where, *a* is the lattice parameter that is 0. 408 nm for Au and hkl corresponds to the coordinates of the corresponding plane. In Figure 38, distance between two crystal planes in the marked region is found ~0.20 ±0.05 nm and from the interplanar distance calculations this distance is attributed in closest approach within the error margin to the (111) and/or (200) planes of Au $d_{111} = \frac{0.408}{\sqrt{1^2+1^2+1^2}}$ = 0.235 nm and $d_{200} = \frac{0.408}{\sqrt{2^2+0^2+0^2}}$ = 0.204 nm, respectively.

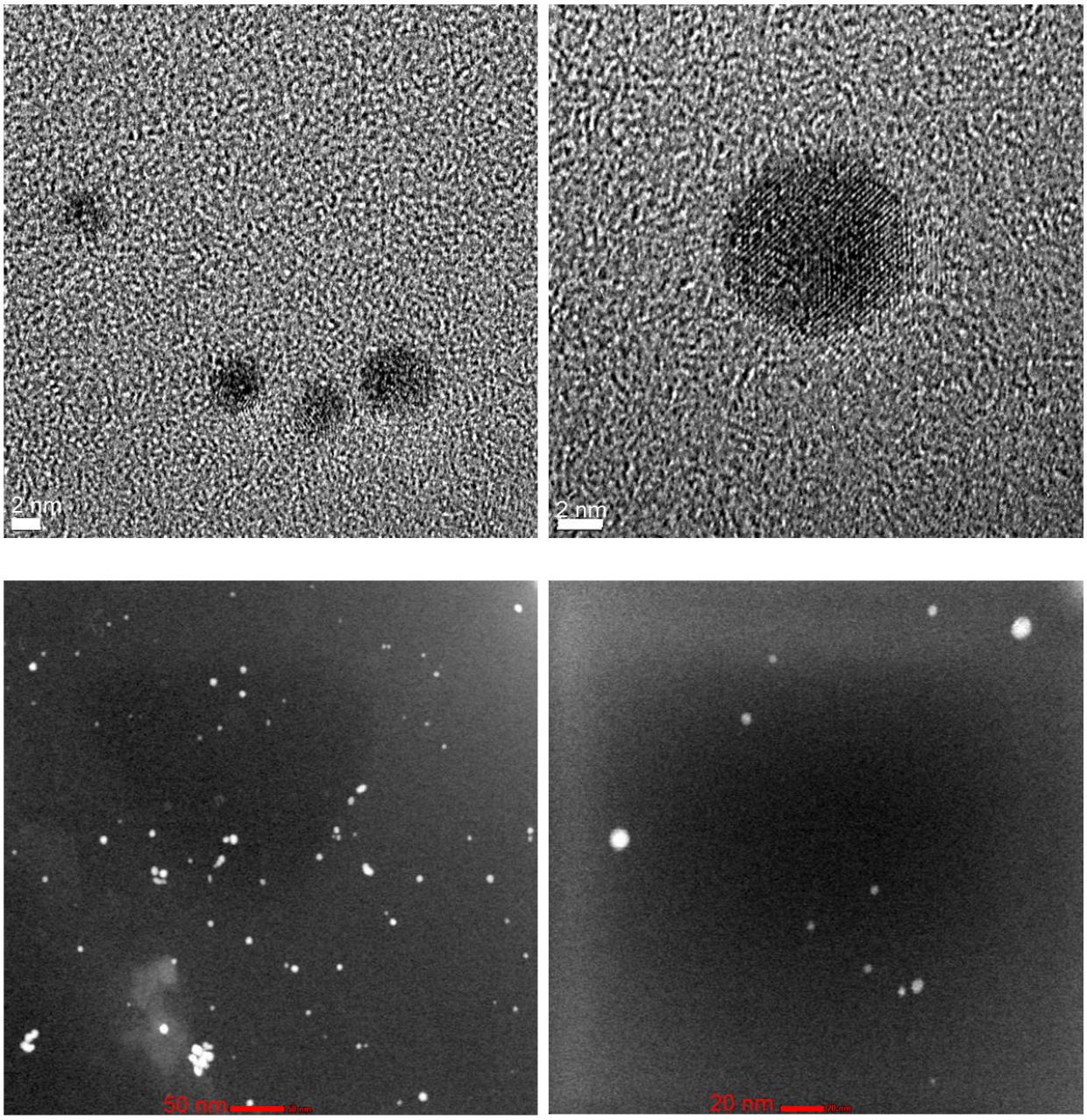

Figure 37. TEM images of Au NPs in DEME-TFSI ionic liquid.

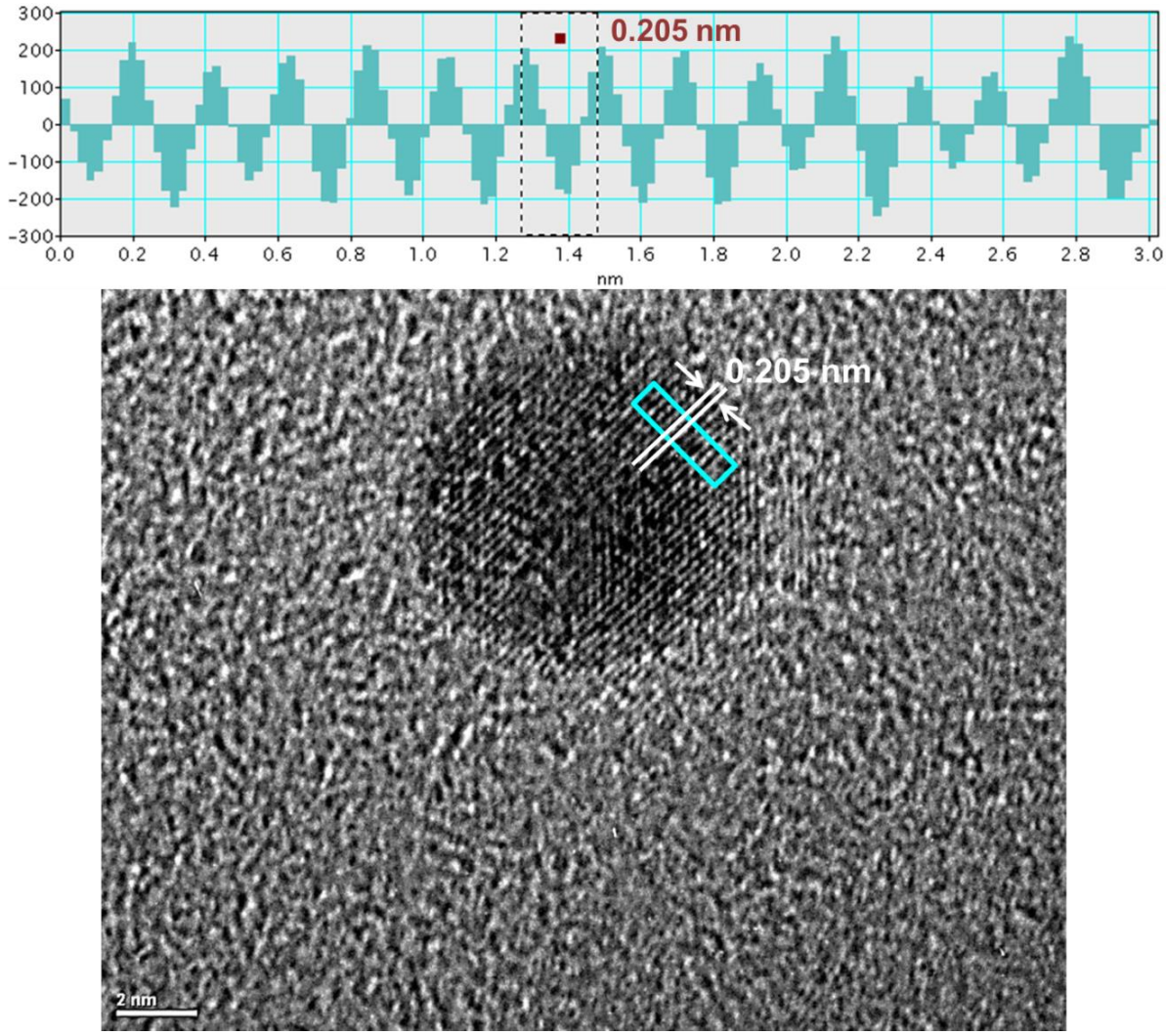

Figure 38. TEM image of Au NPs in DEME-TFSI and the distance profile on top from the marked region.

3.4.4. Electrical Response of Au NPs in DEME-TFSI medium

For analyzing the electrical response of electrochemically produced Au NPs between Au-Pt electrodes using XPS, a 5 µl IL containing the Au NPs is impregnated into PE-membrane between two co-planar Au electrodes in the source and drain geometry (details have been described formerly in Section 2.4.2. and Figure 11). After the transfer of Au NPs in IL to the device, at the onset *no* Pt

species are detected by XPS analyses both in survey and high resolution Pt4f regions but only Au4f peaks are detectable throughout the entire device.

In order to get detailed XPS data on the characterization of Au NPs, the strategy of polarizing Au electrodes is utilized to characterize and separate the Au NP peaks from those of the electrodes. XPS line scan data are collected using X-ray spot size 50 μm and step size 50 μm in the scanning mode for Au 4f and F1s regions under application of ±3V and in the grounded mode. The line scans in Figure 39 (a) represent the collection of Au4f spectra and Figure 39 (b) represents the collection of F1s spectra that are scanned along a 2 mm - line starting from the source electrode toward the middle of the IL-device and color bar represents the intensities of the photoelectron peaks. Au4f spectra corresponding to Au electrode and secondary Au species have no difference when the spectrometer is grounded, yet Au4f peaks are separated through the splitting under applied potential (details have been discussed in Section 3.4.2.) On the contrary, no sign is detected in terms of secondary species formation or splitting of the peaks for F1s region but only a single and continuous peak positions are detected under both +3 V and -3 V D. C. potentials. Also, F1s peak displays uniform 1.5 eV shift, which is only half of the applied potential to the electrode. Figure 39 (a) shows no separated/differentiated Au4f peaks when spectrometer is grounded, since line scan spectra appears to be composed of only one Au4f doublet. The Au-electrodes respond to applied ±3V by ~3eV shift in Au4f binding energy position whereas Au NPs' behavior is reflected in binding energy as ~1.5 eV shift that is in precisely with the shift in the F1s region [Figure 39 (b)].The synchronization of Au NPs and IL-medium, is achieved as the binding energy shifts of the corresponding Au4f and F1s peaks are similar to the applied D.C. potential but

totally different as compared to response of the Au-electrode. These results support that Au NPs reside within IL-medium and not on or in contact with the Au-electrode.

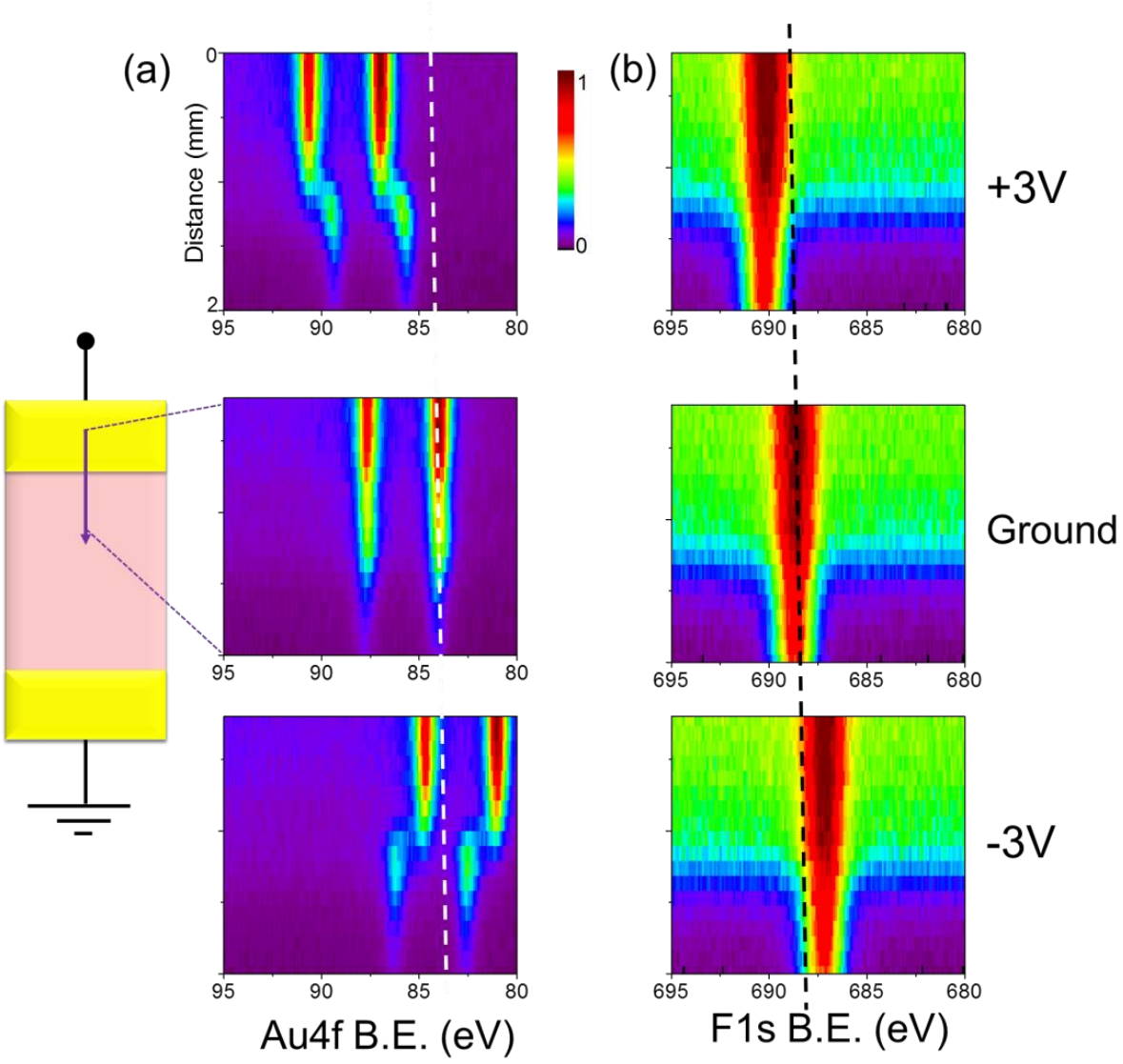

Figure 39. XP spectra of (a) Au4f and (b) F1s regions, recorded in the line scan mode from the source electrode towards the middle of the device under +3V, grounded, and -3V D.C. bias.

In Section 3.2., it was also demonstrated that time-dependent charging behavior of F1s photoelectron peak of the DEME-TFSI IL was found to be different at different lateral positions. Therefore, one can speculate that the Au NPs dispersed in IL should also have similar behavior. In order to test this postulate, Au 4f and F1s regions are recorded with 1s time-resolution for 200 seconds simultaneously while imposing 10 mHz SQW with 3V amplitude, at different lateral positions along the entire device. Figure 40 represents the four lateral positions on the line indicated. The first and fourth points represented by red-color bar, are on the Au-source and the –grounded drain electrodes, respectively and other two points (2^{nd} and 3^{rd}) are at the IL/electrode interfaces. F1s peak is detectable for all points because DEME-TFSI drop spreads over the entire device including the Au-electrodes. Au4f peaks of Au-metal electrodes do not have time dependent response to the external 10 mHz SQW pulses, but at the source-side under positive cycle of the excitation Au4f peak shifts to +3.0 eV higher binding energy position from its grounded position, along with the -3.0 eV shift in the peak position during the negative cycle of SQW excitation and hold their position through the entire cycle. Since drain-electrode is grounded, there is no apparent electrical response detected. The strong time-dependency of F1s peak of IL-medium is clearly displayed at all four points but in the opposite polarization directions at the source- and the drain-electrode sides. For 2^{nd} and 3^{rd} points, time-dependent responses of Au4f peaks corresponding to Au NPs under SQW excitation are in harmony with those of F1s peak of IL medium. Of paramount interest is that the Au4f spectra of the Au NPs are also harmonized with those of the F1s of the IL medium, which also proves our hypothesis.

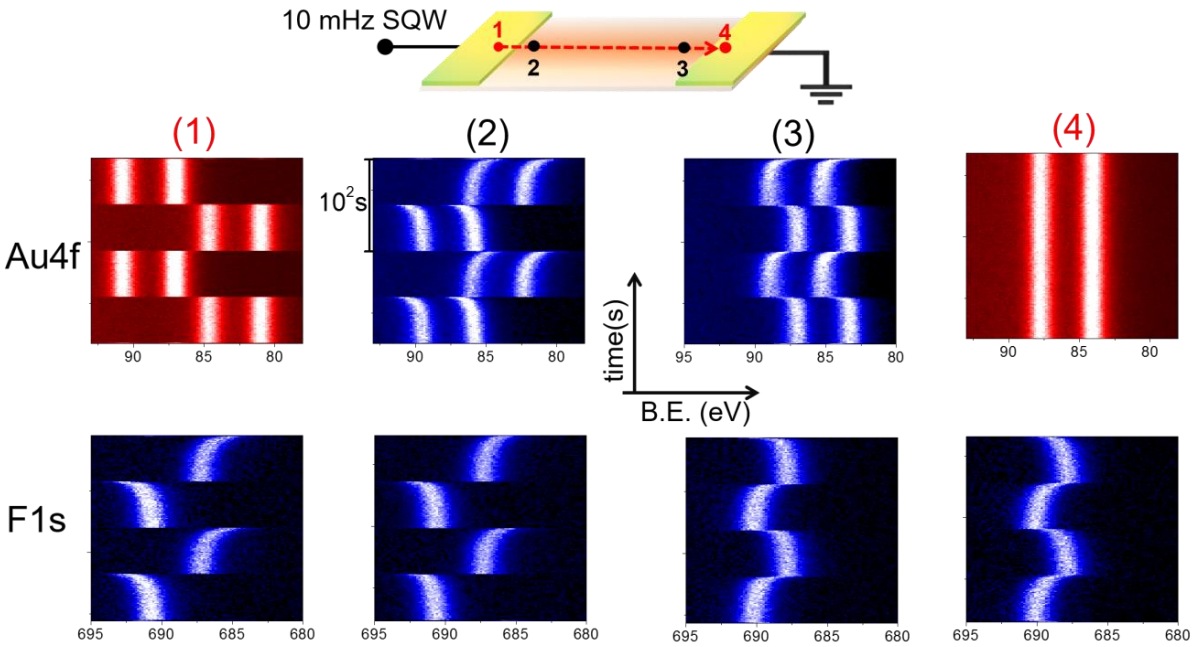

Figure 40. Time-resolved XP spectra of Au 4f and F1s regions under 10 mHz SQW excitation and recorded at four different lateral positions.

Our findings suggest that in our system of the gold electrode in DEME-TFSI, the electrochemically oxidized gold species on the surface of the electrode creates enough strain on the gold surface that leads to dislodging from the electrode surface. Those species eventually get reduced and lead to Au NP formation. Based on what we have probed so far for the in situ preparation of Au NPs *in vacuo*, our results show that;

i. XPS can definitely bring a chemically resolved perspective for in-situ electrochemical reaction monitoring,

ii. Au NPs are synthesized by electrochemical oxidation, possibly first by generation of Au^+ ions, which are reduced to Au^0 and coalesce within the DEME-TFSI medium,

iii. The charging/discharging properties of the Au metal is different from those of the Au NPs dispersed in the IL-medium, leading to completely different responses to electrical excitations, hence offering perfect analytical and spectral separation.

Chapter 4

Conclusions

In this PhD thesis, the electrical properties of co-planar electrochemical DEME-TFSI IL device have been investigated by the novel external biasing approach in XPS. First part of the work has focused on the fundamental understanding of the electrochemical device by the investigation of the device by XPS analysis with modification of the spectrometer to provide both D.C. and A.C. electrical stimuli. The ion imbalance and their preferential arrangements at the properly electrified interfaces and the electrochemical reactions taking place have detected, located and quantified in a chemically resolved way. Then information about electrochemical concepts, including the very long range time and position effects of the electrical double layer formation has been extracted from the electrochemical device with two electrode geometry plus IL medium of DEME-TFSI in between. The EDL formation in nanoscales cannot be monitored directly but the screening of the charge developed at to oppositely charged interfaces and the voltage transient on the entire device enable visualization of the effect of EDL

formation in millimeter scales. Half of the applied 3V potential is found to be prevailed on the entire device and the rest is found to be distributed to two interfacial regions. The charging/discharging behavior is observed to be different with respect to lateral positions on the device and there exist a zero-influence point in the middle of device where charge screening is not felt.

Second part of the work has focused on the interstructural arrangements of mobile ionic constituents within the DEME-TFSI structure. Slowly varying triangular wave pulses are imposed to the electrode and observed to lead to a ~20 % intensity change of $-N^-$ anionic and $-N^+$ cationic fragments while the extent and sign of the polarization have been varied every 500 seconds. In this part we monitored the electrical response at the electrode/DEME-TFSI by XPS since the photon- electron interactions are faster than the relaxation time of the large excess charge at the top 10 nm surface region.

At the last part, XPS has been used for *in-situ* monitoring of electro-corrosion and electrochemical preparation of Au NPs under anodically and cathodically polarization of the electrode in the source-drain geometry. The anodically triggered etching of Au electrode in contact with DEME-TFSI medium causes the simple oxidation of metallic gold and subsequent reduction of the gold ions into nano-sized (~4 nm) Au particles within DEME-TFSI medium. We have also investigated the charging/discharging behaviors of Au4f and F1s peaks corresponding to NPs and IL-medium are found to be in harmony, very different from those of the Au-electrode.

Bibliography

[1] S. Sugden; H. Wilkins, "CLXVII.—The parachor and chemical constitution. Part XII. Fused metals and salts". *Journal of the Chemical Society (Resumed)*, pp. 1291-1298, 1929.

[2] F. H. Hurley; T. P. Wier, "The electrodeposition of aluminum from nonaqueous solutions at room temperature". *Journal of the Electrochemical Society*, vol. 98, pp. 207-212, 1951.

[3] T. Jr. P. Wier, "Electrodeposition of aluminum". U.S. Patent 2446349 A, August 03 1948.

[4] W. Sundermeyer, "Fused salts and their use as reaction media". *Angewandte Chemie International Edition*, vol. 4, pp. 222-238, 1965.

[5] J. S. Wilkes; J. A. Levisky; R. A. Wilson; C. L. Hussey, "Dialkylimidazolium chloroaluminate melts: a new class of room-temperature ionic liquids for electrochemistry, spectroscopy and synthesis". *Inorganic Chemistry*, vol. 21, pp. 1263-1264, 1982.

[6] J. S. Wilkes, "A short history of ionic liquids—from molten salts to neoteric solvents". *Green Chemistry*, vol. 4, pp. 73-80, 2002.

[7] R. D. Rogers; K. R. Seddon, "Ionic liquids--solvents of the future?". *Science*, vol. 302, pp. 792-793, 2003.

[8] T. Welton, "Room-temperature ionic liquids. Solvents for synthesis and catalysis". *Chemical Reviews*, vol. 99, pp. 2071-2084, 1999.

[9] J. F. Brennecke; E. J. Maginn, "Ionic liquids: innovative fluids for chemical processing". *AIChE Journal*, vol. 47, pp. 2384-2389, 2001.

[10] C. P. Fredlake; J. M. Crosthwaite; D. G. Hert; S. N. Aki; J. F. Brennecke, "Thermophysical properties of imidazolium-based ionic liquids". *Journal of Chemical & Engineering Data***,** vol. 49, pp. 954-964, 2004.

[11] M. Deetlefs; K. R. Seddon; M. Shara, "Predicting physical properties of ionic liquids". *Physical Chemistry Chemical Physics***,** vol. 8, pp. 642-649, 2006.

[12] S. Zhang; N. Sun; X. He; X. Lu; X. Zhang, "Physical properties of ionic liquids: database and evaluation". *Journal of physical and chemical reference data***,** vol. 35, pp. 1475-1517, 2006.

[13] M. Armand; F. Endres; D. R. Macfarlane; H. Ohno; B. Scrosati, "Ionic-liquid materials for the electrochemical challenges of the future". *Nature materials***,** vol. 8, pp. 621-629, 2009.

[14] M. Galiński; A. Lewandowski; I. Stępniak, "Ionic liquids as electrolytes". *Electrochimica Acta***,** vol. 51, pp. 5567-5580, 2006.

[15] P. Bonhote; A.-P. Dias; N. Papageorgiou; K. Kalyanasundaram; M. Grätzel, "Hydrophobic, highly conductive ambient-temperature molten salts". *Inorganic Chemistry***,** vol. 35, pp. 1168-1178, 1996.

[16] D. Macfarlane; P. Meakin; J. Sun; N. Amini; M. Forsyth, "Pyrrolidinium imides: a new family of molten salts and conductive plastic crystal phases". *The Journal of Physical Chemistry B***,** vol. 103, pp. 4164-4170, 1999.

[17] S. V. Dzyuba; R. A. Bartsch, "Influence of structural variations in 1-alkyl (aralkyl)-3-methylimidazolium hexafluorophosphates and bis (trifluoromethylsulfonyl) imides on physical properties of the ionic liquids". *ChemPhysChem***,** vol. 3, pp. 161-166, 2002.

[18] M. C. Buzzeo; R. G. Evans; R. G. Compton, "Non-haloaluminate room-temperature ionic liquids in electrochemistry—A review". *ChemPhysChem***,** vol. 5, pp. 1106-1120, 2004.

[19] A. B. Mcewen; S. F. Mcdevitt; V. R. Koch, "Nonaqueous electrolytes for electrochemical capacitors: imidazolium cations and inorganic fluorides with organic carbonates". *Journal of the Electrochemical Society***,** vol. 144, pp. L84-L86, 1997.

[20] A. B. Mcewen; H. L. Ngo; K. Lecompte; J. L. Goldman, "Electrochemical properties of imidazolium salt electrolytes for electrochemical capacitor applications". *Journal of the Electrochemical Society***,** vol. 146, pp. 1687-1695, 1999.

[21] G. J. Kabo; A. V. Blokhin; Y. U. Paulechka; A. G. Kabo; M. P. Shymanovich; J. W. Magee, "Thermodynamic properties of 1-butyl-3-methylimidazolium hexafluorophosphate in the condensed state". *Journal of Chemical & Engineering Data***,** vol. 49, pp. 453-461, 2004.

[22] M. Bier; S. Dietrich, "Vapour pressure of ionic liquids". *Molecular Physics***,** vol. 108, pp. 211-214, 2010.

[23] P. Wasserсheid; W. Keim, "Ionic liquids-new “solutions” for transition metal catalysis". *Angewandte Chemie International Edition,* vol. 39, pp. 3772-3789, 2000.

[24] P. Wasserscheid, "Chemistry: Volatile times for ionic liquids". *Nature***,** vol. 439, pp. 797-797, 2006.

[25] R. Ludwig; U. Kragl, "Do we understand the volatility of ionic liquids?". *Angewandte Chemie International Edition,* vol. 46, pp. 6582-6584, 2007.

[26] E. Frackowiak; F. Beguin, "Carbon materials for the electrochemical storage of energy in capacitors". *Carbon***,** vol. 39, pp. 937-950, 2001.

[27] J. Zheng; J. Huang; T. Jow, "The limitations of energy density for electrochemical capacitors". *Journal of the Electrochemical Society***,** vol. 144, pp. 2026-2031, 1997.

[28] I. Osada; H. De Vries; B. Scrosati; S. Passerini, "Ionic-Liquid-Based Polymer Electrolytes for Battery Applications". *Angewandte Chemie International Edition,* vol.55, pp. 500-513, 2015.

[29] Y. Lu; K. Korf; Y. Kambe; Z. Tu; L. A. Archer, "Ionic-Liquid–Nanoparticle Hybrid Electrolytes: Applications in Lithium Metal Batteries". *Angewandte Chemie International Edition,* vol. 126, pp. 498-502, 2014.

[30] K. L. Van Aken; M. Beidaghi; Y. Gogotsi, "Formulation of Ionic-Liquid Electrolyte To Expand the Voltage Window of Supercapacitors". *Angewandte Chemie International Edition***,** vol. 54, pp. 4806-4809, 2015.

[31] J. P. Hallett; T. Welton, "Room-temperature ionic liquids: solvents for synthesis and catalysis. 2". *Chemical Reviews***,** vol. 111, pp. 3508-3576, 2011.

[32] T. Matsuda; N. Taccardi; J. Schwegler; P. Wasserscheid; H. P. Steinrück; F. Maier, "Vacuum Surface Science Meets Heterogeneous Catalysis: Dehydrogenation of a Liquid Organic Hydrogen Carrier in the Liquid State". *ChemPhysChem*,vol. 16, pp.1873- 1879, 2015.

[33] H. P. Steinrück; J. Libuda; P. Wasserscheid; T. Cremer; C. Kolbeck; M. Laurin; F. Maier; M. Sobota; P. Schulz; M. Stark, "Surface Science and Model Catalysis with Ionic Liquid-Modified Materials". *Advanced Materials***,** vol. 23, pp. 2571-2587, 2011.

[34] R. H. Venderbosch; W. Prins; W. P. M. Van Swaaij, "Platinum catalyzed oxidation of carbon monoxide as a model reaction in mass transfer measurements". *Chemical Engineering Science***,** vol. 53, pp. 3355-3366, 1998.

[35] J. Zhu; Y. Shen; A. Xie; L. Qiu; Q. Zhang; S. Zhang, "Photoinduced synthesis of anisotropic gold nanoparticles in room-temperature ionic liquid". *The Journal of Physical Chemistry C***,** vol. 111, pp. 7629-7633, 2007.

[36] J. Ghilane; P. Martin; O. Fontaine; J.-C. Lacroix; H. Randriamahazaka, "Modification of carbon electrode in ionic liquid through the reduction of phenyl diazonium salt. Electrochemical evidence in ionic liquid". *Electrochemistry communications***,** vol. 10, pp. 1060-1063, 2008.

[37] J. Dupont; G. S. Fonseca; A. P. Umpierre; P. F. Fichtner; S. R. Teixeira, "Transition-metal nanoparticles in imidazolium ionic liquids: recycable catalysts for biphasic hydrogenation reactions". *Journal of the American Chemical Society***,** vol. 124, pp. 4228-4229, 2002.

[38] M. A. Gelesky; A. P. Umpierre; G. Machado; R. R. Correia; W. C. Magno; J. Morais; G. Ebeling; J. Dupont, "Laser-induced fragmentation of transition metal nanoparticles in ionic liquids". *Journal of the American Chemical Society***,** vol. 127, pp. 4588-4589, 2005.

[39] J. Krämer; E. Redel; R. Thomann; C. Janiak, "Use of ionic liquids for the synthesis of iron, ruthenium, and osmium nanoparticles from their metal carbonyl precursors". *Organometallics***,** vol. 27, pp. 1976-1978, 2008.

[40] E. Redel; M. Walter; R. Thomann; L. Hussein; M. Krüger; C. Janiak, "Stop-and-go, stepwise and “ligand-free” nucleation, nanocrystal growth and formation of Au-NPs in ionic liquids (ILs)". *Chemical communications***,** vol. 46, pp. 1159-1161, 2010.

[41] F. Endres; M. Bukowski; R. Hempelmann; H. Natter, "Electrodeposition of nanocrystalline metals and alloys from ionic liquids". *Angewandte Chemie International Edition***,** vol. 42, pp. 3428-3430, 2003.

[42] F. Endres; S. Z. El Abedin, "Electrodeposition of stable and narrowly dispersed germanium nanoclusters from an ionic liquid". *Chemical communications***,** pp. 892-893, 2002.

[43] P. Simon; Y. Gogotsi, "Materials for electrochemical capacitors". *Nature materials***,** vol. 7, pp. 845-854, 2008.

[44] G. Wang; L. Zhang; J. Zhang, "A review of electrode materials for electrochemical supercapacitors". *Chemical Society Reviews***,** vol. 41, pp. 797-828, 2012.

[45] F. Endres, "Ionic liquids: solvents for the electrodeposition of metals and semiconductors". *ChemPhysChem***,** vol. 3, pp. 144-154, 2002.

[46] F. Endres; D. Macfarlane; A. Abbott, Eds. *Electrodeposition from ionic liquids*. Weinheim: Wiley-VCH Verlag GmbH & Co.KGaA, 2008.

[47] A. Lewandowski; A. Świderska-Mocek, "Ionic liquids as electrolytes for Li-ion batteries—an overview of electrochemical studies". *Journal of Power Sources***,** vol. 194, pp. 601-609, 2009.

[48] H. Ohno, Eds. "*Electrochemical aspects of ionic liquids*." New Jersey: John Wiley & Sons Inc., 2011.

[49] A. M. O'mahony; D. S. Silvester; L. Aldous; C. Hardacre; R. G. Compton, "Effect of water on the electrochemical window and potential limits of room-temperature ionic liquids". *Journal of Chemical & Engineering Data***,** vol. 53, pp. 2884-2891, 2008.

[50] T. J. Gannon; G. Law; P. R. Watson; A. J. Carmichael; K. R. Seddon, "First observation of molecular composition and orientation at the surface of a room-temperature ionic liquid". *Langmuir***,** vol. 15, pp. 8429-8434, 1999.

[51] G. Law; P. R. Watson; A. J. Carmichael; K. R. Seddon, "Molecular composition and orientation at the surface of room-temperature ionic liquids: effect of molecular structure". *Physical Chemistry Chemical Physics***,** vol. 3, pp. 2879-2885, 2001.

[52] S. Baldelli, "Influence of water on the orientation of cations at the surface of a room-temperature ionic liquid: a sum frequency generation vibrational spectroscopic study". *The Journal of Physical Chemistry B***,** vol. 107, pp. 6148-6152, 2003.

[53] S. Rivera-Rubero; S. Baldelli, "Surface characterization of 1-butyl-3-methylimidazolium Br-, I-, PF6-, BF4-,(CF3SO2) 2N-, SCN-, CH3SO3-, CH3SO4-, and (CN) 2N-ionic liquids by sum frequency generation". *The Journal of Physical Chemistry B***,** vol. 110, pp. 4756-4765, 2006.

[54] E. Sloutskin; B. M. Ocko; L. Tamam; I. Kuzmenko; T. Gog; M. Deutsch, "Surface layering in ionic liquids: an X-ray reflectivity study". *Journal of the American Chemical Society***,** vol. 127, pp. 7796-7804, 2005.

[55] S. A. Kislenko; I. S. Samoylov; R. H. Amirov, "Molecular dynamics simulation of the electrochemical interface between a graphite surface and the ionic liquid [BMIM][PF 6]". *Physical Chemistry Chemical Physics***,** vol. 11, pp. 5584-5590, 2009.

[56] C. Merlet; M. Salanne; B. Rotenberg; P. A. Madden, "Imidazolium ionic liquid interfaces with vapor and graphite: interfacial tension and capacitance from coarse-grained molecular simulations". *The Journal of Physical Chemistry C***,** vol. 115, pp. 16613-16618, 2011.

[57] C. Merlet; B. Rotenberg; P. A. Madden; M. Salanne, "Computer simulations of ionic liquids at electrochemical interfaces". *Physical Chemistry Chemical Physics***,** vol. 15, pp. 15781-15792, 2013.

[58] A. A. Kornyshev, "Double-layer in ionic liquids: paradigm change?". *The Journal of Physical Chemistry B***,** vol. 111, pp. 5545-5557, 2007.

[59] M. V. Fedorov; A. A. Kornyshev, "Towards understanding the structure and capacitance of electrical double layer in ionic liquids". *Electrochimica Acta***,** vol. 53, pp. 6835-6840, 2008.

[60] M. V. Fedorov; A. A. Kornyshev, "Ionic liquid near a charged wall: structure and capacitance of electrical double layer". *The Journal of Physical Chemistry B***,** vol. 112, pp. 11868-11872, 2008.

[61] R. Hayes; N. Borisenko; M. K. Tam; P. C. Howlett; F. Endres; R. Atkin, "Double layer structure of ionic liquids at the Au (111) electrode interface: an atomic force microscopy investigation". *The Journal of Physical Chemistry C***,** vol. 115, pp. 6855-6863, 2011.

[62] S. Baldelli, "Interfacial structure of room-temperature ionic liquids at the solid–liquid interface as probed by sum frequency generation spectroscopy". *The Journal of Physical Chemistry Letters***,** vol. 4, pp. 244-252, 2012.

[63] K. B. Oldham, "A Gouy–Chapman–Stern model of the double layer at a (metal)/(ionic liquid) interface". *Journal of Electroanalytical Chemistry***,** vol. 613, pp. 131-138, 2008.

[64] D. C. Grahame, "The electrical double layer and the theory of electrocapillarity". *Chemical Reviews***,** vol. 41, pp. 441-501, 1947.

[65] A. J. Bard; L. R. Faulkner; J. Leddy; C. G. Zoski, "*Electrochemical methods: fundamentals and applications*." D. Harris, E. Swain, C. Robey, Eds.Vol. 2. New York: Wiley, pp. 534-579, 2001.

[66] S. Baldelli, "Surface structure at the ionic liquid− electrified metal interface". *Accounts of chemical research***,** vol. 41, pp. 421-431, 2008.

[67] M. V. Fedorov; N. Georgi; A. A. Kornyshev, "Double layer in ionic liquids: The nature of the camel shape of capacitance". *Electrochemistry communications***,** vol. 12, pp. 296-299, 2010.

[68] W. Zhou; S. Inoue; T. Iwahashi; K. Kanai; K. Seki; T. Miyamae; D. Kim; Y. Katayama; Y. Ouchi, "Double layer structure and adsorption/desorption hysteresis of neat ionic liquid on Pt electrode surface—an in-situ IR-visible sum-frequency generation spectroscopic study". *Electrochemistry communications***,** vol. 12, pp. 672-675, 2010.

[69] S. Makino; Y. Kitazumi; N. Nishi; T. Kakiuchi, "Charging current probing of the slow relaxation of the ionic liquid double layer at the Pt electrode". *Electrochemistry communications***,** vol. 13, pp. 1365-1368, 2011.

[70] F. Endres; N. Borisenko; S. Z. El Abedin; R. Hayes; R. Atkin, "The interface ionic liquid (s)/electrode (s): In situ STM and AFM measurements". *Faraday discussions***,** vol. 154, pp. 221-233, 2012.

[71] K. Motobayashi; K. Minami; N. Nishi; T. Sakka; M. Osawa, "Hysteresis of potential-dependent changes in ion density and structure of an ionic liquid on a gold electrode: in situ observation by surface-enhanced infrared absorption spectroscopy". *The Journal of Physical Chemistry Letters***,** vol. 4, pp. 3110-3114, 2013.

[72] N. Nishi; Y. Hirano; T. Motokawa; T. Kakiuchi, "Ultraslow relaxation of the structure at the ionic liquid| gold electrode interface to a potential step probed by electrochemical surface plasmon resonance measurements: asymmetry of the relaxation time to the potential-step direction". *Physical Chemistry Chemical Physics***,** vol. 15, pp. 11615-11619, 2013.

[73] R. Atkin; N. Borisenko; M. Drüschler; F. Endres; R. Hayes; B. Huber; B. Roling, "Structure and dynamics of the interfacial layer between ionic liquids and electrode materials". *Journal of Molecular Liquids***,** vol. 192, pp. 44-54, 2014.

[74] V. Ivaništšev; K. Kirchner; T. Kirchner; M. V. Fedorov, "Restructuring of the electrical double layer in ionic liquids upon charging". *Journal of Physics: condensed matter***,** vol. 27, pp. 102101, 2015.

[75] K. Kirchner; T. Kirchner; V. Ivaništšev; M. V. Fedorov, "Electrical double layer in ionic liquids: Structural transitions from multilayer to monolayer structure at the interface". *Electrochimica Acta***,** vol. 110, pp. 762-771, 2013.

[76] M. A. Gebbie; M. Valtiner; X. Banquy; E. T. Fox; W. A. Henderson; J. N. Israelachvili, "Ionic liquids behave as dilute electrolyte solutions". *Proceedings of the National Academy of Sciences***,** vol. 110, pp. 9674-9679, 2013.

[77] C. Merlet; D. T. Limmer; M. Salanne; R. Van Roij; P. A. Madden; D. Chandler; B. Rotenberg, "The electric double layer has a life of its own". *The Journal of Physical Chemistry C***,** vol. 118, pp. 18291-18298, 2014.

[78] H. Li; F. Endres; R. Atkin, "Effect of alkyl chain length and anion species on the interfacial nanostructure of ionic liquids at the Au (111)–ionic liquid interface as a function of potential". *Physical Chemistry Chemical Physics***,** vol. 15, pp. 14624-14633, 2013.

[79] R. Costa; C. M. Pereira; A. F. Silva, "Charge Storage on Ionic Liquid Electric Double Layer: The Role of the Electrode Material". *Electrochimica Acta***,** vol. 167, pp. 421-428, 2015.

[80] M. V. Fedorov; A. A. Kornyshev, "Ionic liquids at electrified interfaces". *Chemical Reviews***,** vol. 114, pp. 2978-3036, 2014.

[81] A. A. Kornyshev; R. Qiao, "Three-dimensional double layers". *The Journal of Physical Chemistry C***,** vol. 118, pp. 18285-18290, 2014.

[82] J. Jiang; D. Cao; D.-E. Jiang; J. Wu, "Kinetic charging inversion in ionic liquid electric double layers". *The Journal of Physical Chemistry Letters***,** vol. 5, pp. 2195-2200, 2014.

[83] E. Schmidt; S. Shi; P. P. Ruden; C. D. Frisbie, "Characterization of the Electric Double Layer Formation Dynamics of a Metal-Ionic Liquid-Metal Structure". *ACS applied materials & interfaces*, vol.8, pp. 14879–14884 , 2016.

[84] M. Faraday, "The Bakerian lecture: experimental relations of gold (and other metals) to light". *Philosophical Transactions of the Royal Society of London***,** vol. 147, pp. 145-181, 1857.

[85] G. Schmid, "Large clusters and colloids. Metals in the embryonic state". *Chemical Reviews***,** vol. 92, pp. 1709-1727, 1992.

[86] G. Schmid; L. F. Chi, "Metal clusters and colloids". *Advanced Materials***,** vol. 10, pp. 515-526, 1998.

[87] M. Brust; C. J. Kiely, "Some recent advances in nanostructure preparation from gold and silver particles: a short topical review". *Colloids and Surfaces A: Physicochemical and Engineering Aspects***,** vol. 202, pp. 175-186, 2002.

[88] M.-C. Daniel; D. Astruc, "Gold nanoparticles: assembly, supramolecular chemistry, quantum-size-related properties, and applications toward biology, catalysis, and nanotechnology". *Chemical Reviews***,** vol. 104, pp. 293-346, 2004.

[89] S. Eustis; M. A. El-Sayed, "Why gold nanoparticles are more precious than pretty gold: noble metal surface plasmon resonance and its enhancement of the radiative and nonradiative properties of nanocrystals of different shapes". *Chemical Society Reviews***,** vol. 35, pp. 209-217, 2006.

[90] D. L. Feldheim; C. A. Foss, *Metal nanoparticles: synthesis, characterization, and applications*; New York and Basel: Marcel Dekker, Inc., 2002.

[91] A. Henglein, "Physicochemical properties of small metal particles in solution:" microelectrode" reactions, chemisorption, composite metal particles, and the atom-to-metal transition". *The Journal of Physical Chemistry***,** vol. 97, pp. 5457-5471, 1993.

[92] W. P. Mcconnell; J. P. Novak; L. C. Brousseau Iii; R. R. Fuierer; R. C. Tenent; D. L. Feldheim, "Electronic and optical properties of chemically modified metal nanoparticles and molecularly bridged nanoparticle arrays". *The Journal of Physical Chemistry B***,** vol. 104, pp. 8925-8930, 2000.

[93] M. Kim; V. N. Phan; K. Lee, "Exploiting nanoparticles as precursors for novel nanostructure designs and properties". *CrystEngComm***,** vol. 14, pp. 7535-7548, 2012.

[94] P. V. Kamat, "Photophysical, photochemical and photocatalytic aspects of metal nanoparticles". *J. Phys. Chem. B***,** vol. 106, pp. 7729-7744, 2002.

[95] I. Hussain; S. Graham; Z. Wang; B. Tan; D. C. Sherrington; S. P. Rannard; A. I. Cooper; M. Brust, "Size-controlled synthesis of near-monodisperse gold nanoparticles in the 1-4 nm range using polymeric stabilizers". *Journal of the American Chemical Society***,** vol. 127, pp. 16398-16399, 2005.

[96] T. Tsuda; S. Seino; S. Kuwabata, "Gold nanoparticles prepared with a room-temperature ionic liquid–radiation irradiation method". *Chemical communications***,** pp. 6792-6794, 2009.

[97] D. B. Williams; C. B. Carter, The transmission electron microscope. In *Transmission electron microscopy*, New York: Springer Science and Business Media, LLC, pp. 3-17, 1996.

[98] Z. Wang, "Transmission electron microscopy of shape-controlled nanocrystals and their assemblies". *The Journal of Physical Chemistry B,* vol. 104, pp. 1153-1175, 2000.

[99] J. N. Canongia Lopes; A. A. Pádua, "Nanostructural organization in ionic liquids". *The Journal of Physical Chemistry B,* vol. 110, pp. 3330-3335, 2006.

[100] H. Weingärtner, "Understanding ionic liquids at the molecular level: facts, problems, and controversies". *Angewandte Chemie International Edition,* vol. 47, pp. 654-670, 2008.

[101] J. Dupont, "From molten salts to ionic liquids: a "nano" journey". *Accounts of chemical research,* vol. 44, pp. 1223-1231, 2011.

[102] M. Antonietti; D. Kuang; B. Smarsly; Y. Zhou, "Ionic liquids for the convenient synthesis of functional nanoparticles and other inorganic nanostructures". *Angewandte Chemie International Edition,* vol. 43, pp. 4988-4992, 2004.

[103] S. L. Craig, "From ionic liquids to supramolecular polymers". *Angewandte Chemie International Edition,* vol. 48, pp. 2645-2647, 2009.

[104] J. Dupont; J. D. Scholten, "On the structural and surface properties of transition-metal nanoparticles in ionic liquids". *Chemical Society Reviews,* vol. 39, pp. 1780-1804, 2010.

[105] C. Vollmer; C. Janiak, "Naked metal nanoparticles from metal carbonyls in ionic liquids: Easy synthesis and stabilization". *Coordination Chemistry Reviews,* vol. 255, pp. 2039-2057, 2011.

[106] J. D. Scholten; B. C. Leal; J. Dupont, "Transition metal nanoparticle catalysis in ionic liquids". *ACS Catalysis,* vol. 2, pp. 184-200, 2011.

[107] Janiak, C. in *Ionic liquids (ILs) in organometallic catalysis*; Dupont, J.,Kolla´r, L., Eds.; Springer: Newy York, pp 17-55, 2013.

[108] M. Scariot; D. O. Silva; J. D. Scholten; G. Machado; S. R. Teixeira; M. A. Novak; G. Ebeling; J. Dupont, "Cobalt nanocubes in ionic liquids: synthesis and properties". *Angewandte Chemie International Edition,* vol. 47, pp. 9075-9078, 2008.

[109] E. Redel; R. Thomann; C. Janiak, "Use of ionic liquids (ILs) for the IL-anion size-dependent formation of Cr, Mo and W nanoparticles from metal carbonyl M (CO) 6 precursors". *Chemical communications,* pp. 1789-1791, 2008.

[110] T. Torimoto; K.-I. Okazaki; T. Kiyama; K. Hirahara; N. Tanaka; S. Kuwabata, "Sputter deposition onto ionic liquids: Simple and clean synthesis of highly dispersed ultrafine metal nanoparticles". *Applied Physics Letters,* vol. 89, p 243117, 2006.

[111] K.-I. Okazaki; T. Kiyama; K. Hirahara; N. Tanaka; S. Kuwabata; T. Torimoto, "Single-step synthesis of gold–silver alloy nanoparticles in ionic liquids by a sputter deposition technique". *Chemical communications*, pp. 691-693, 2008.

[112] W. Dobbs; J. M. Suisse; L. Douce; R. Welter, "Electrodeposition of Silver Particles and Gold Nanoparticles from Ionic Liquid-Crystal Precursors". *Angewandte Chemie*, vol. 118, pp. 4285-4288, 2006.

[113] S. Z. El Abedin; M. Pölleth; S. Meiss; J. Janek; F. Endres, "Ionic liquids as green electrolytes for the electrodeposition of nanomaterials". *Green Chemistry*, vol. 9, pp. 549-553, 2007.

[114] S. Z. El Abedin; A. Saad; H. Farag; N. Borisenko; Q. Liu; F. Endres, "Electrodeposition of selenium, indium and copper in an air-and water-stable ionic liquid at variable temperatures". *Electrochimica Acta*, vol. 52, pp. 2746-2754, 2007.

[115] K. Manojkumar; A. Sivaramakrishna; K. Vijayakrishna, "A short review on stable metal nanoparticles using ionic liquids, supported ionic liquids, and poly(ionic liquids)". *Journal of Nanoparticle Research*, vol. 18, p 103, 2016.

[116] Y. Gao; A. Voigt; M. Zhou; K. Sundmacher, "Synthesis of Single-Crystal Gold Nano- and Microprisms Using a Solvent-Reductant-Template Ionic Liquid". *European Journal of Inorganic Chemistry*, vol. 2008, pp. 3769-3775, 2008.

[117] G. H. Hong; S. W. Kang, "Synthesis of Monodisperse Copper Nanoparticles by Utilizing 1-Butyl-3-methylimidazolium Nitrate and Its Role as Counteranion in Ionic Liquid in the Formation of Nanoparticles". *Industrial & Engineering Chemistry Research*, vol. 52, pp. 794-797, 2012.

[118] D. Briggs; M. P. Seah; H. Bubert, "Practical Surface Analysis. Vol. 1: Auger and X-ray Photoelectron Spectroscopy". *Angewandte Chemie-German Edition*, vol. 107, pp. 1367-1367, 1995.

[119] J. F. Watts; J. Wolstenholme, "An introduction to surface analysis by XPS and AES". *An Introduction to Surface Analysis by XPS and AES*, Wiley-VCH, 2003.

[120] M. Seah; S. Spencer, "Ultrathin SiO2 on Si II. Issues in quantification of the oxide thickness". *Surface and interface analysis*, vol. 33, pp. 640-652, 2002.

[121] T. Cremer; M. Stark; A. Deyko; H.-P. SteinrüCk; F. Maier, "Liquid/solid interface of ultrathin ionic liquid films:[C1C1Im][Tf2N] and [C8C1Im][Tf2N] on Au (111)". *Langmuir*, vol. 27, pp. 3662-3671, 2011.

[122] S. Suzer, "Differential charging in X-ray photoelectron spectroscopy: a nuisance or a useful tool?". *Analytical chemistry*, vol. 75, pp. 7026-7029, 2003.

[123] B. Bozzini; M. Amati; L. Gregoratti; M. K. Abyaneh; M. Prasciolu; A. L. Trygub; M. Kiskinova, "Microscale evolution of surface chemistry and morphology of the key components in operating hydrocarbon-fuelled SOFCs". *The Journal of Physical Chemistry C***,** vol. 116, pp. 23188-23193, 2012.

[124] H. Sezen; S. Suzer, "XPS for chemical-and charge-sensitive analyses". *Thin Solid Films***,** vol. 534, pp. 1-11, 2013.

[125] G. Ertas; S. Suzer, "XPS analysis with external bias: a simple method for probing differential charging". *Surface and interface analysis***,** vol. 36, pp. 619-623, 2004.

[126] F. Karadas; G. Ertas; E. Ozkaraoglu; S. Suzer, "X-ray-induced production of gold nanoparticles on a SiO2/Si system and in a poly (methyl methacrylate) matrix". *Langmuir***,** vol. 21, pp. 437-442, 2005.

[127] U. K. Demirok; G. Ertas; S. Suzer, "Time-resolved XPS analysis of the SiO2/Si system in the millisecond range". *The Journal of Physical Chemistry B***,** vol. 108, pp. 5179-5181, 2004.

[128] H. Sezen; G. Ertas; A. Dâna; S. Suzer, "Charging/discharging of thin PS/PMMA films as probed by dynamic X-ray photoelectron spectroscopy". *Macromolecules***,** vol. 40, pp. 4109-4112, 2007.

[129] S. Suzer; H. Sezen; G. Ertas; A. D Na, "XPS measurements for probing dynamics of charging". *Journal of Electron Spectroscopy and Related Phenomena***,** vol. 176, pp. 52-57, 2010.

[130] M. Taner-Camcı; S. Suzer, "Dynamic XPS measurements of ultrathin polyelectrolyte films containing antibacterial Ag–Cu nanoparticles". *Journal of Vacuum Science & Technology A***,** vol. 32, pp. 021510, 2014.

[131] E. F. Smith; F. J. Rutten; I. J. Villar-Garcia; D. Briggs; P. Licence, "Ionic liquids in vacuo: analysis of liquid surfaces using ultra-high-vacuum techniques". *Langmuir***,** vol. 22, pp. 9386-9392, 2006.

[132] E. F. Smith; I. J. V. Garcia; D. Briggs; P. Licence, "Ionic liquids in vacuo; solution-phase X-ray photoelectron spectroscopy". *Chemical communications***,** pp. 5633-5635, 2005.

[133] K. R. Lovelock; E. F. Smith; A. Deyko; I. J. Villar-Garcia; P. Licence; R. G. Jones, "Water adsorption on a liquid surface". *Chemical communications***,** pp. 4866-4868, 2007.

[134] O. Höfft; S. Bahr; M. Himmerlich; S. Krischok; J. Schaefer; V. Kempter, "Electronic structure of the surface of the ionic liquid [EMIM][Tf2N] studied by metastable impact electron spectroscopy (MIES), UPS, and XPS". *Langmuir***,** vol. 22, pp. 7120-7123, 2006.

[135] V. Lockett; R. Sedev; C. Bassell; J. Ralston, "Angle-resolved X-ray photoelectron spectroscopy of the surface of imidazolium ionic liquids". *Physical Chemistry Chemical Physics***,** vol. 10, pp. 1330-1335, 2008.

[136] K. R. Lovelock; I. J. Villar-Garcia; F. Maier; H.-P. SteinrüCk; P. Licence, "Photoelectron spectroscopy of ionic liquid-based interfaces". *Chemical Reviews***,** vol. 110, pp. 5158-5190, 2010.

[137] P. Licence, "In Situ XPS Monitoring of Bulk Ionic Liquid Reactions: Shedding Light on Organic Reaction Mechanisms". *Angewandte Chemie International Edition***,** vol. 51, pp. 4789-4791, 2012.

[138] L. G. Chen; H. Bermudez In *Ionic Liquids: Science and Applications*, ACS Symposium Series; American Chemical Society*:* Washington, DC, 2012.

[139] F. Maier; J. M. Gottfried; J. Rossa; D. Gerhard; P. S. Schulz; W. Schwieger; P. Wasserscheid; H. P. Steinrück, "Surface Enrichment and Depletion Effects of Ions Dissolved in an Ionic Liquid: An X-ray Photoelectron Spectroscopy Study". *Angewandte Chemie International Edition***,** vol. 45, pp. 7778-7780, 2006.

[140] S. Caporali; M. Pedio; C. Chiappe; C. S. Pomelli; R. G. Acres; U. Bardi, "Surface study of metal-containing ionic liquids by means of photoemission and absorption spectroscopies". *Surface science***,** vol. 648, pp. 360-365, 2016.

[141] A. W. Taylor; F. Qiu; I. J. Villar-Garcia; P. Licence, "Spectroelectrochemistry at ultrahigh vacuum: in situ monitoring of electrochemically generated species by X-ray photoelectron spectroscopy". *Chemical communications***,** pp. 5817-5819, 2009.

[142] R. Wibowo; L. Aldous; R. M. Jacobs; N. S. Manan; R. G. Compton, "Monitoring potassium metal electrodeposition from an ionic liquid using in situ electrochemical-X-ray photoelectron spectroscopy". *Chemical physics letters***,** vol. 509, pp. 72-76, 2011.

[143] R. Wibowo; L. Aldous; R. M. Jacobs; N. S. Manan; R. G. Compton, "In situ electrochemical-X-ray Photoelectron Spectroscopy: Rubidium metal deposition from an ionic liquid in competition with solvent breakdown". *Chemical physics letters***,** vol. 517, pp. 103-107, 2011.

[144] C. H. Wu; R. S. Weatherup; M. B. Salmeron, "Probing electrode/electrolyte interfaces in situ by X-ray spectroscopies: old methods, new tricks". *Physical Chemistry Chemical Physics***,** vol. 17, pp. 30229-30239, 2015.

[145] S. Caporali; U. Bardi; A. Lavacchi, "X-ray photoelectron spectroscopy and low energy ion scattering studies on 1-buthyl-3-methyl-imidazolium bis (trifluoromethane) sulfonimide". *Journal of Electron Spectroscopy and Related Phenomena***,** vol. 151, pp. 4-8, 2006.

[146] A. Foelske-Schmitz; D. Weingarth; H. Kaiser; R. Kötz, "Quasi in situ XPS study of anion intercalation into HOPG from the ionic liquid [EMIM][BF 4]". *Electrochemistry communications***,** vol. 12, pp. 1453-1456, 2010.

[147] A. Foelske-Schmitz; P. W. Ruch; R. Kötz, "Ion intercalation into HOPG in supercapacitor electrolyte–An X-ray photoelectron spectroscopy study". *Journal of Electron Spectroscopy and Related Phenomena***,** vol. 182, pp. 57-62, 2010.

[148] M. A. Gebbie; H. A. Dobbs; M. Valtiner; J. N. Israelachvili, "Long-range electrostatic screening in ionic liquids". *Proceedings of the National Academy of Sciences***,** vol. 112, pp. 7432-7437, 2015.

[149] Y. Liu; C. Lu; S. Twigg; M. Ghaffari; J. Lin; N. Winograd; Q. Zhang, "Direct observation of ion distributions near electrodes in ionic polymer actuators containing ionic liquids". *Scientific reports***,** vol.3, pp.973 (1-5), 2013.

[150] S. Xu; S. Xing; S.-S. Pei; V. IvanišTšEv; R. Lynden-Bell; S. Baldelli, "Molecular Response of 1-Butyl-3-Methylimidazolium Dicyanamide Ionic Liquid at the Graphene Electrode Interface Investigated by Sum Frequency Generation Spectroscopy and Molecular Dynamics Simulations". *The Journal of Physical Chemistry C***,** vol. 119, pp. 26009–26019, 2015.

[151] C. Y. PeñAlber; S. Baldelli, "Observation of Charge Inversion of an Ionic Liquid at the Solid Salt–Liquid Interface by Sum Frequency Generation Spectroscopy". *The Journal of Physical Chemistry Letters***,** vol. 3, pp. 844-847, 2012.

[152] Y.-X. Zhong; J.-W. Yan; M.-G. Li; X. Zhang; D.-W. He; B.-W. Mao, "Resolving fine structures of the electric double layer of electrochemical interfaces in ionic liquids with an AFM tip modification strategy". *Journal of the American Chemical Society***,** vol. 136, pp. 14682-14685, 2014.

[153] R. M. Lynden-Bell; M. G. Del Popolo; T. G. Youngs; J. Kohanoff; C. G. Hanke; J. B. Harper; C. C. Pinilla, "Simulations of ionic liquids, solutions, and surfaces". *Accounts of chemical research***,** vol. 40, pp. 1138-1145, 2007.

[154] B. Bhargava; S. Balasubramanian, "Layering at an ionic liquid-vapor interface: A molecular dynamics simulation study of [bmim][PF6]". *Journal of the American Chemical Society***,** vol. 128, pp. 10073-10078, 2006.

[155] D. Weingarth; A. Foelske-Schmitz; A. Wokaun; R. Kötz, "In situ electrochemical XPS study of the Pt/[EMIM][BF 4] system". *Electrochemistry communications***,** vol. 13, pp. 619-622, 2011.

[156] C. Kolbeck; T. Cremer; K. Lovelock; N. Paape; P. Schulz; P. Wasserscheid; F. Maier; H.-P. Steinruck, "Influence of different anions on the surface composition of ionic liquids studied using ARXPS". *The Journal of Physical Chemistry B***,** vol. 113, pp. 8682-8688, 2009.

[157] S. Men; D. S. Mitchell; K. R. Lovelock; P. Licence, "X-ray Photoelectron Spectroscopy of Pyridinium-Based Ionic Liquids: Comparison to Imidazolium-and Pyrrolidinium-Based Analogues". *ChemPhysChem*, vol.16, pp. 2211-2218, 2015.

[158] H. Matsumoto; H. Kageyama; Y. Miyazaki, "Room temperature molten salts based on tetraalkylammonium cations and bis (trifluoromethylsulfonyl) imide". *Chemistry Letters***,** vol.30, pp. 182-183, 2001.

[159] H. Matsumoto; H. Kageyama; Y. Miyazaki, "Room temperature ionic liquids based on small aliphatic ammonium cations and asymmetric amide anions". *Chemical communications***,** pp. 1726-1727, 2002.

[160] T. Sato; G. Masuda; K. Takagi, "Electrochemical properties of novel ionic liquids for electric double layer capacitor applications". *Electrochimica Acta***,** vol. 49, pp. 3603-3611, 2004.

[161] T. Sato; G. Masuda; K. Takagi, "Corrigendum to “Electrochemical properties of novel ionic liquids for electric double layer capacitor applications”[Electrochim. Acta 49 (2004) 3603–3611]". *Electrochimica Acta***,** vol. 53, pp. 4934-4935, 2008.

[162] Y. Yoshimura; T. Takekiyo; Y. Imai; H. Abe, "Pressure-induced spectral changes of room-temperature ionic liquid, N, N-diethyl-N-methyl-N-(2-methoxyethyl) ammonium bis (trifluoromethylsulfonyl) imide,[DEME][TFSI]". *The Journal of Physical Chemistry C***,** vol. 116, pp. 2097-2101, 2011.

[163] R. Hayes; G. G. Warr; R. Atkin, "Structure and nanostructure in ionic liquids". *Chemical Reviews***,** vol. 115, pp. 6357-6426, 2015.

[164] C. Kocabas; S. Suzer, "Probing Voltage Drop Variations in Graphene with Photoelectron Spectroscopy". *Analytical chemistry***,** vol. 85, pp. 4172-4177, 2013.

[165] I. J. Villar-Garcia; E. F. Smith; A. W. Taylor; F. Qiu; K. R. Lovelock; R. G. Jones; P. Licence, "Charging of ionic liquid surfaces under X-ray irradiation: the measurement of absolute binding energies by XPS". *Physical Chemistry Chemical Physics***,** vol. 13, pp. 2797-2808, 2011.

[166] E. Infeld; G. Rowlands, *Nonlinear waves, solitons and chaos*. Cambridge: Cambridge university press, 2000.

[167] K. Iwata; H. Okajima; S. Saha; H.-O. Hamaguchi, "Local structure formation in alkyl-imidazolium-based ionic liquids as revealed by linear and nonlinear Raman spectroscopy". *Accounts of chemical research***,** vol. 40, pp. 1174-1181, 2007.

[168] Z.-X. Luo; Y.-Z. Xing; Y.-C. Ling; A. Kleinhammes; Y. Wu, "Electroneutrality breakdown and specific ion effects in nanoconfined aqueous electrolytes observed by NMR". *Nature communications***,** vol. 6, pp. 6358 (1-5), 2015.

[169] J. M. Griffin; A. C. Forse; W.-Y. Tsai; P.-L. Taberna; P. Simon; C. P. Grey, "In situ NMR and electrochemical quartz crystal microbalance techniques reveal the structure of the electrical double layer in supercapacitors". *Nature materials*, vol.14, pp. 812-819, 2015.

[170] M. Mezger; H. Schröder; H. Reichert; S. Schramm; J. S. Okasinski; S. Schöder; V. Honkimäki; M. Deutsch; B. M. Ocko; J. Ralston, "Molecular layering of fluorinated ionic liquids at a charged sapphire (0001) surface". *Science***,** vol. 322, pp. 424-428, 2008.

[171] M. Mezger; B. M. Ocko; H. Reichert; M. Deutsch, "Surface layering and melting in an ionic liquid studied by resonant soft X-ray reflectivity". *Proceedings of the National Academy of Sciences***,** vol. 110, pp. 3733-3737, 2013.

[172] A. Uysal; H. Zhou; G. Feng; S. S. Lee; S. Li; P. Fenter; P. T. Cummings; P. F. Fulvio; S. Dai; J. K. Mcdonough, "Structural origins of potential dependent hysteresis at the electrified graphene/ionic liquid interface". *The Journal of Physical Chemistry C***,** vol. 118, pp. 569-574, 2013.

[173] A. Uysal; H. Zhou; G. Feng; S. S. Lee; S. Li; P. T. Cummings; P. F. Fulvio; S. Dai; J. K. Mcdonough; Y. Gogotsi, "Interfacial ionic 'liquids': connecting static and dynamic structures". *Journal of Physics: condensed matter***,** vol. 27, p 032101, 2015.

[174] Y. Wang, "Disordering and reordering of ionic liquids under an external electric field". *The Journal of Physical Chemistry B***,** vol. 113, pp. 11058-11060, 2009.

[175] C. Kolbeck; I. Niedermaier; A. Deyko; K. R. Lovelock; N. Taccardi; W. Wei; P. Wasserscheid; F. Maier; H. P. Steinrück, "Influence of Substituents and Functional Groups on the Surface Composition of Ionic Liquids". *Chemistry-A European Journal***,** vol. 20, pp. 3954-3965, 2014.

[176] X. Liu; M. Atwater; J. Wang; Q. Huo, "Extinction coefficient of gold nanoparticles with different sizes and different capping ligands". *Colloids and Surfaces B: Biointerfaces***,** vol. 58, pp. 3-7, 2007.